Computational Modeling of Cardiovascular Flows using Smoothed Particle Hydrodynamics

Shahrokh Shahriari

A Thesis

in the Department

of

Mechanical and Industrial Engineering

Presented in Partial Fulfillment of the Requirements

for the Degree of Doctor of Philosophy (Mechanical Engineering) at

Concordia University

Montreal, Quebec, Canada

December 2011

CONCORDIA UNIVERSITY

SCHOOL OF GRADUATE STUDIES

This is to certify that the thesis prepared

By: **Shahrokh Shahriari**

Entitled: **Computational Modeling of Cardiovascular Flows using Smoothed Particle Hydrodynamics**

and submitted in partial fulfillment of the requirements for the degree of

DOCTOR OF PHILOSOPHY (Mechanical Engineering)

complies with the regulations of the University and meets the accepted standards with respect to originality and quality.

Signed by the final examining committee:

_____ Chair
Dr. Y. Zeng

_____ External Examiner
Dr. D.A. Steinman

_____ External to Program
Dr. N. Bouguila

_____ Examiner
Dr. A. Dolatabadi

_____ Examiner
Dr. H.D. Ng

_____ Thesis Co-Supervisor
Dr. L. Kadem

_____ Thesis Co-Supervisor
Dr. I. Hassan

Approved by _____
Dr. W-F. Xie, Graduate Program Director

December 5, 2011

_____
Dr. Robin A.L. Drew, Dean
Faculty of Engineering & Computer Science

ABSTRACT

Computational Modeling of Cardiovascular Flows using Smoothed Particle Hydrodynamics

Shahrokh Shahriari, Ph.D.

Concordia University, 2011

This dissertation presents the first attempt to verify the capability of smoothed particle hydrodynamics (SPH), a meshfree particle method, to simulate pulsatile flow in the cardiovascular system. Smoothed particle hydrodynamics has been extensively used to simulate astrophysical phenomena, free surface flows and transient start-up of the internal flows under constant driving forces at low Reynolds numbers. However, most of the fluid flow phenomena are naturally unsteady with moderate Reynolds numbers. In this thesis, first, a series of benchmark cases are conducted to address internal oscillating flows at moderate Reynolds numbers. The performance of the two most commonly used formulations to model the diffusing viscous term and the XSPH variant, proposed to modify the movement of the particles, is investigated. The relation between particle resolution and sound speed to control compressibility effects in SPH simulations and the spatial convergence rate of the SPH discretization are examined. Furthermore, a modified formulation for wall shear stress calculations is suggested and an approach to implement inflow and outflow boundary conditions in SPH is introduced. It is also shown how SPH simulations with different particle resolutions exhibit behaviors equivalent to a finite volume scheme of different accuracy orders for moderate Reynolds numbers. The application of SPH to cardiovascular fluid dynamics is extended by simulating pulsatile

flow inside a model of the heart's left ventricle and through normal and dysfunctional prosthetic mechanical heart valves. The SPH simulations result in the realistic calculation of the shear stress loading on the blood components and illustrate the important role played by non-physiological flow patterns to shear-induced hemodynamic events.

To my wife, parents and brother

Acknowledgments

It is a pleasure to thank all those who have supported and inspired me during my doctoral studies.

Above all, I would like to express my keen gratitude to my wife for her support, encouragements and great patience during my PhD studies. I wish to thank her for providing a loving environment for me.

My deepest acknowledgement goes to my parents as role models in my life and for giving their invaluable support, love, understanding and sacrifices throughout the years of my education. I appreciate all their great wishes to encourage me to continue my education to the highest possible level. They were always the strongest motivation to go forward in my life and studies.

I would like to express my special appreciation to my principal supervisor, Dr. Lyes Kadem, director of the cardiovascular fluid dynamics laboratory (LCFD) for his advice, efforts, encouragement and friendship. I acknowledge all his contributions of research facilities and funding to pursue the objectives of this thesis. I am also appreciating his support to give me the opportunity to attend international conferences and meetings in order to interact with other researchers.

I wish to acknowledge my co-supervisor, Prof. Ibrahim Hassan, for his support, patience and encouraging words. His advice was invaluable on both academic and daily life.

Many thanks go to Dr. Benedict Rogers, School of Mechanical, Aerospace and Civil Engineering from Manchester University, United Kingdom, for inviting me as a visiting doctoral student to Manchester University, one of the leading research institutes of the Smoothed Particle Hydrodynamics European Research Interest Community (SPHERIC).

I acknowledge Concordia University for technical facilities and financial support, especially the scholarships and awards that encouraged and facilitated my achievements.

Many thanks to the staff at the Department of Mechanical and Industrial Engineering for providing technical and administrative support throughout my PhD studies.

I acknowledge the University of Sherbrooke for providing access to the high performance computing facilities (Mammouth supercomputing cluster). I would also like to thank the people at LCFD for their cooperation.

Finally, I would like to acknowledge my defense committee members, Dr. David Steinman from University of Toronto and Dr. Nizar Bouguila, Dr. Ali Dolatabadi and Dr. Hoi Dick Ng from Concordia University for their advice, suggestions and time devoted to my thesis during the busy fall semester.

Table of Contents

List of Figures

List of Tables

Nomenclature

α	Coefficient of artificial viscosity
$\boldsymbol{a}$	Acceleration vector
β	Coefficient of artificial viscosity; Coefficient of extrapolated velocity
β_{max}	Parameter set to 1.5
c	Sound speed
C_{μ}	Turbulent parameter $= 0.07 - 0.09$
C_{ξ}	Correction coefficient for wall shear stress calculations
d	Distance
δ	Thickness of oscillating layer
E	Energy dissipation rate
ε	XSPH variant
$\boldsymbol{f}_{body}$	Body force per unit volume
f_x	Force applied per unit of the fluid mass
γ	Specific heat ratio
η	Non-dimensional distance
h	Smoothing length
k	Turbulent kinetic energy

l_m	Mixing length
m	Mass
μ	Dynamic viscosity
μ_e	Effective viscosity
N	Number of particles
ν	Kinematic viscosity
ν_T	Turbulent eddy viscosity
ω	Oscillation frequency
P	Thermodynamic pressure; Production of kinetic energy
P_0	Reference pressure
Q	Volumetric flow rate
q	Non-dimensional distance between particles
r	Distance between two particles
r_0	Initial particle spacing
$\boldsymbol{r}$	Position vector of a given point
Re_o	Oscillating Reynolds number
ρ	Density
ρ_0	Reference density

S	Mean strain rate
σ_k	Turbulent parameter $= 1$
t	Time
T	Period
τ	Turbulent shear stress
τ_w	Wall shear stress
$\boldsymbol{V}$	Velocity vector
W	Kernel function
W_o	Womersly number
X	Coordinate on x- axis
Y	Coordinate on y- axis
∇	Gradient of a scalar or vector

Subscript and Superscript

0	Initial condition
a	Regarding coordinates of particle a
b	Regarding coordinates of particle b
ab	Particle b relative to particle a; Average properties of particle a and b
$inlet, outlet$	Inlet/ outlet boundary condition

max	Maximum
n	Time step; Normal to a line
t	Tangent to a line
T	Turbulent
x	x-component of a vector
y	y-component of a vector

Abbreviation

ALE	Arbitrary Lagrangian Eulerian
BMHV	Bileaflet mechanical heart valve
CFD	Computational fluid dynamics
CFL	Courant-Friedrichs-Levy
CSM	Computational solid mechanics
EFG	Element free Galerkin
FD	Finite difference
FE	Finite element
FSI	Fluid structure interaction
FV	Finite volume
IBM	Immersed boundary method
LBM	Lattice Boltzmann method
LES	Large eddy simulation
LV	Left ventricle
MD	Molecular dynamics
MHD	Magnetohydrodynamics
MHV	Mechanical heart valve
MLS	Moving least square

PIC	Particle in cell
RANS	Reynolds averaged Navier-Stokes
SPH	Smoothed particle hydrodynamics
VOF	Volume of fluid
VPI	Virtual particle integration

Introduction

Numerical simulations have significantly enhanced our knowledge of physical phenomena in science and engineering. In comparison with analytical analyses, computational methods generally require less unrealistic assumptions. They are also considered as a substitute for experimental studies which are expensive and time consuming. Numerical simulations have contributed widely to uncovering physical phenomena in emerging fields of research.

Biomechanical engineering is an emerging multidisciplinary field integrating engineering and medicine. It involves several academic disciplines and professional specializations and aims to improve the quality of healthcare diagnosis and treatment. It combines the design and problem solving skills of engineering with medical and biological expertise.

The study of blood flow in the cardiovascular system under normal and pathological conditions is of great importance in biomechanical engineering. Cardiovascular diseases are the major cause of death in North America (Heart and Stroke Foundation of Canada, 2003). It is essential, therefore, to develop tools that can successfully study the hemodynamics of the heart and the arteries, investigate the hemodynamic complications encountered with cardiovascular diseases, test alternative surgical procedures and estimate their clinical impact on the hemodynamic condition of the patient. For this purpose, clinical researchers mainly rely on personal experience and *in vitro* facilities.

It is of great significance then, to develop *in silico* tools capable of simulating cardiovascular fluid dynamics. Despite the great developments in computational methods

and computer capabilities, solving such problems using conventional mesh-based methods is complex. These methods have already demonstrated good capabilities in simulating cardiovascular flows and generated interesting results with significant clinical and practical implications. The main inherent limitation of mesh-based methods is their dependency on the process of mesh generation. Also, some important characteristics of cardiovascular flows, mainly under pathological conditions are difficult to capture using mesh-based methods. Examples include, flow in complex geometries, tracking fluid properties history, thrombus formation and break up of red blood cells (microcirculation). The simulation of such characteristics requires computational fluid dynamic (CFD) methods based on a Lagrangian approach instead of Eulerian approach, and therefore simulating blood flow using meshfree particle methods. Meshfree methods do not spend time on the generation or regeneration of the mesh network and creation of connectivity between the nodes. In this thesis, Smoothed Particle Hydrodynamics (SPH), a fully Lagrangian meshfree method, is used to address this issue. SPH was applied originally to astrophysics in the 1970s and its first terrestrial application was performed in 1994 to simulate inviscid water flows. The SPH method has several advantages, including fully meshfree nature, presenting limited difficulties in treatment of complex geometries, easy to get time history of physical variables, naturally suited for parallel computation, and very wide application from micro- to macro-scale phenomena.

In SPH, a continuum medium is comprised of a set of particles. Each particle has its own physical properties. Numerical discretization involves interpolating the value of a physical property for a given particle based on the properties of its neighboring particles using an interpolating function.

This thesis is the first work dedicated specifically to the SPH simulation of cardiovascular flows in a variety of flow characteristics and geometries.

Chapter 1 provides an overview on computational mesh-based and meshfree methods and their advantages and disadvantages. The most widely used meshfree methods and their limitations are described and the motivations to select SPH as a promising candidate to simulate problems in cardiovascular fluid dynamics are provided.

Chapter 2 provides a bibliography on the historical development of SPH and its mathematical formulation and numerical features such as different SPH discretization for Navier-Stokes equations, time integration technique and boundary condition implementations.

In chapter 3, the ability of SPH to simulate oscillating and steady flows at different flow characteristics and moderate Reynolds numbers are examined. The selected benchmark cases have similarities in geometry and flow characteristics with the cardiovascular system. First, the performance of the two most commonly used formulations for viscous term modeling is studied. Then, the effect of using the XSPH variant, suggested to keep the movement of each particle consistent with the average velocity of its neighboring particles, on particle distribution is investigated. Some points regarding the use of symmetric form of pressure gradient modeling are discussed. After that, the application of SPH is extended to oscillating flows imposed by oscillating body forces and oscillating moving boundary for different oscillating frequencies and amplitudes. Also, a modified formulation for wall shear stress calculations is introduced and verified against exact solutions. The results for SPH simulation of the lid-driven cavity flow, at higher Reynolds numbers than reported in the literature, are shown. In this

simulation, an interesting feature of SPH in relation to particle resolution and sound speed to control the compressibility effects is revealed.

Chapter 4 aims to extend the application of SPH to simulate flow inside a model of the heart's left ventricle (LV). This is the first attempt to simulate flow inside LV using a meshfree particle method. Simulating this kind of flow, characterized by high pulsatility and moderate Reynolds number using SPH is challenging. First, the simulation results for a pulsatile flow in a rectangular cavity are presented and the results are compared to those obtained using the finite volume method. An approach to deal with inflow and outflow boundary conditions is introduced and verified. Finally, the flow in a model of LV under pulsatile inflow condition is simulated and the ability of SPH to track fluid properties history is illustrated. Some interesting features of SPH are also demonstrated including the relation between particle resolution and sound speed to control the compressibility effects and order of convergence in SPH simulations.

Chapter 5 extends the application of SPH to simulate flow through normal and dysfunctional bileaflet mechanical heart valves (BMHVs) with a realistic aortic flow waveform. Evaluating shear induced hemodynamic events is of primary importance for the design of mechanical heart valves (MHVs). Currently, this relies on numerical simulations based on Eulerian approach. However, a more accurate evaluation should be based on the analysis of the Lagrangian dynamics of blood components. This chapter represents the first attempt to simulate turbulent pulsatile flow through BMHVs using SPH. The results obtained regarding the accumulation of shear stress patterns on blood components illustrates the important role played by non-physiological flow patterns and mainly vortical structures. The statistical distribution of particles with respect to shear

stress loading history provides important information regarding the relative number of blood components that can be damaged.

Finally, an overall conclusion and future directions of this work are described.

Chapter 1

Computational Mesh-Based and Meshfree Methods

A comprehensive review of computational mesh-based and meshfree methods is presented and their advantages and disadvantages are discussed. The main advantages of using Smoothed Particle Hydrodynamics (SPH), a fully Lagrangian meshfree method, are also highlighted.

1.1. Introduction

Computational methods are essential to simulate different physical phenomena. Experimental studies are expensive and time consuming to adjust and analytical analyses are possible for limited physical problems with a series of unrealistic assumptions. Different types of computational methods have been developed and employed in the previous and present century. In conventional methods, the physical domain is discretized into meshes. The meshes are fixed in the domain (Eulerian approach) or attached to the material and move in the domain (Lagrangian approach). The meshes are defined in three forms including, connected nodes in the finite difference (FD) method, volumes (cells) in the finite volume (FV) method and elements in the finite element (FE) method. The meshes are used for transforming governing differential equations of physical phenomena (in physical domains) into a set of algebraic equations (in discretized computational domains).

Computational methods in fluid mechanics, known as computational fluid dynamics (CFD), are widely used to simulate fluid dynamic phenomena. In CFD, the physical governing equations of fluid motion, Navier-Stokes equations, are discretized in the spatial and temporal domain and approximated by a system of algebraic equations solved by computational algorithms.

1.2. Mesh-based Methods

In the finite difference (FD) method, developed in the 1920s, the physical differential equations are approximated to a series of FD equations at mesh points or nodes (Anderson, 1995). This method is difficult to implement for an unstructured mesh and not accurate for flow simulation in complex geometries. The derivatives of the variables in differential equations are approximated using Taylor series expansion.

In the finite volume (FV) method, differential equations are represented as a set of algebraic equations based on an infinitesimal volume surrounding each point in a meshed geometry (Versteeg and Malalasekra, 2007). This method is able to handle flow simulations in complex geometries using unstructured meshes. However, the method has difficulties simulating 3D phenomena. In FV, interpolation techniques are applied to calculate the values of physical variables at the surface of each finite volume using computed variables at the central node of the volumes. Then the flux at the volume surface is evaluated (using quadrature formulae) and the volume integrals of the physical governing equations, in integral forms, are converted to surface integrals (using the divergence theorem).

Similar to the FV method, the finite element (FE) method discretizes the physical domain into elements in which the variables across the elements are calculated based on the values at the element nodes (Zienkiewicz et al., 2005). The differential equations are approximated by a set of numerically stable equations developed based on nodal points. The FE method is suitable for problems with complex geometries and has been used widely in different areas.

Simulation of the interaction of fluid flow with structures, known as fluid structure interaction (FSI) modeling, is of great interest for the CFD community in which two common techniques are used: The immersed boundary method (IBM) and the arbitrary Lagrangian Eulerian (ALE) approach.

Immersed boundary method uses a combination of Eulerian and Lagrangian variables. The fluid domain is described on a fixed, Eulerian, frame of reference and the structure is described in a Lagrangian manner (Peskin, 2002). The Navier-Stokes equations are solved based on discretized Eulerian grids and the structure is modeled as a set of connected points. These points move freely in a Lagrangian frame of reference through Eulerian grids in accordance with the applied hydrodynamic forces. The interaction between the structural points and the fluid grids is modeled based on force density functions. This interaction procedure employs a Dirac delta approximation function.

In the ALE technique, nodes in the fluid domain can be fixed or move arbitrarily in a Lagrangian manner giving optimized shapes to the elements (mesh rezoning) (Souli and Benson, 2010). However, special treatment is needed for momentum remapping. Fluid elements interacting with moving structures, can easily track the boundary movements.

Conventional mesh-based methods have been used over a wide area in CFD and computational solid mechanics (CSM). These methods have several inherent advantages, including:

- The algorithms and associated procedures are robust and well understood.
- Several types of commercial software are available with convenient and user-friendly interface.
- The computational time step is appropriate for engineering applications, although it depends on the selected technique and algorithm.
- They have determined stability and high accuracy.

The main difficulty in these methods is their dependence on the process of mesh generation, distortion and regeneration which are time consuming and can lead to additional computational error. The problems with complex geometries and moving boundaries are still challenging for these computational methods. Some limitations of these methods include:

- Complex and irregular geometries are meshed with difficulty.
- The entire domain needs to be meshed. (Liu and Liu, 2003)
- In problems with large deformations, a mesh regeneration process is needed to prevent distortion of meshes. This is complex and computationally expensive.
- The location of deformable and moving interfaces is not determined precisely. (Liu and Liu, 2003)

- In some methods such as the FD method, it is necessary to map an irregular physical geometry to a regular computational domain. (Anderson, 1995)
- These methods are not well adapted for monitoring material properties and determination of time history of the materials. (Liu, 2010)
- In fluid structure interaction problems, a strong coupling between Eulerian and Lagrangian variables is needed which increases the computation time.

Due to the above limitations, it is desirable to propose methods that are independent of mesh generation or regeneration processes. To overcome these limitations a new class of methods called meshfree methods was introduced.

1.3. Meshfree Methods

In meshfree methods, no kind of mesh is used to approximate physical quantities and to convert differential equations to algebraic equations. The physical domain is discretized with a set of points (nodes) that are not connected with each other, unlike mesh-based methods. The physical governing equations are approximated based on the points, not the elements. These methods have similar fundamental concepts, but differ in employing approximation functions, discretization equation systems and the implementation methodology. (Liu and Liu, 2003)

Meshfree methods spend minimal time on generation or regeneration of the mesh network and the creation of connections between meshes. Some meshfree methods need a background mesh to integrate the system of equations locally or within the entire domain. Methods that do not use meshes in any way can be implemented easily, but they are sensitive to stability and accuracy related issues. (Liu, 2010)

Meshfree methods are in the development stage and several modifications remain in progress. In the following sections, the most developed and widely used meshfree methods are briefly described and their features are discussed.

1.3.1. Molecular Dynamics Method

Molecular dynamics (MD) is a meshfree computational method introduced for modeling molecular level systems based on statistical mechanics. It was developed to overcome the difficulties in analytical modeling of physical systems having an infinite number of atoms.

The classical MD is based on Newton's second law. In the computational domain, atoms or molecules interact based on intermolecular forces derived from an interaction potential function. Molecular dynamics was first applied in chemistry and physics and then to material science in 1960 by Gibson. Later, macroscopic physical models were introduced to extend the application of MD to simulate macro-scale phenomena. The first MD modeling of a system of liquid water was performed by Bernal (1962) and Stillinger and Rahman (1974).

The MD method at macroscopic scales is not accurate enough to reproduce the realistic dynamics of a physical system. Simulation of a continuum fluid domain, determination of transport properties and accurate potential functions still need further examination.

1.3.2. Monte Carlo Method

Monte Carlo method is categorized as a probabilistic meshfree method. This method approximates the mathematical equations using random numbers and probability theory.

This method can be applied to problems with both inherent probabilistic and non probabilistic characteristics. The Monte Carlo method originated by Ulam and Metropolis on the subject of chance games (Metropolis, 1987).

The first works extending the application of Monte Carlo to physics and engineering include: the book written by Hammersley and Handscomb (1964), the work done by Haji-Sheikh and Sparrow (1967) to model heat conduction problems, the study of Binder (1992) on determination of the physical properties of the condensed matters and simulation of inviscid fluid flow problem by Perez and Zachrich (2000).

Implementation of the Monte Carlo method requires an iterative process including creation of the model, generation of random inputs and evaluation of the model.

1.3.3. Lattice Boltzmann Method

Lattice Boltzmann method (LBM) was first developed to solve governing equations in compressible fluid dynamics. The fluid domain is discretized by a series of uniformly spaced lattice nodes. The continuous Boltzmann equation is approximated based on the nodes and an interaction model is adopted to mimic the viscous flow behavior (Chen and Doolen, 1998).

The motion of particles under the governing equations of fluid dynamics is mimicked using specific collision rules. Particle movements are modeled using distribution functions, which define the density and velocity at each lattice node.

The significant developments in LBM were done by Hardy et al. in 1976 proposing a particle velocity model to determine the transport properties of the fluids and by Frisch et

al. in 1986 to correct governing equations of the fluid flow based on the lattice gas automata.

To calculate pressure field, there is no need to solve the Poisson equation. This method is classified as a probabilistic meshfree method. The major disadvantages of this method for incompressible fluid dynamic applications are compressibility effects and instabilities resulting in limitations in increasing the time step for the simulations. Also, this method requires a background lattice of nodes and is not a fully meshfree method. This method is not applicable for solving solid dynamic equations leading to similar difficulties as in mesh-based method for FSI simulations.

1.3.4. Element Free Galerkin Method

The element free Galerkin (EFG) method was introduced by Belytschko et al. (1994). This method is a combination of finite element and meshfree methods.

Numerical approximation is performed based on the moving least square (MLS) concept on a set of nodes in the entire domain to construct a shape function. The system of equations is descritized in Galerkin form and the integration procedure is done using a background mesh. This method is also not fully meshfree.

The challenges in the EFG method include the construction of an appropriate shape function and using background meshes for the integration process.

1.3.5. Immersed Boundary Method

The immersed boundary method was developed by Peskin in 1972 to model fluid structure interactions in biological systems, especially blood flow in the heart. The immersed boundary method can not be categorized exactly as a meshfree method, but the

implementation technique to model the interaction between the fluid domain and the moving solid structure is not performed like in conventional mesh-based methods.

In the immersed boundary method, a Cartesian mesh is created in the entire fluid domain. The solid structure is not constrained by Eulerian fluid meshes and can move without restriction. The Eulerian fluid variables are linked to the Lagrangian solid variables by a Dirac delta function. (Peskin, 2002)

This method needs a background mesh for integration of flow equations and is not implemented easily in problems with variable fluid viscosity and anisotropic solid elasticity.

1.3.6. Vortex Method

In this method, flow governing equations are transformed to the form of the vorticity transport equation. As a result, the method does not need to solve the pressure term in the Navier-Stokes equations. The discretized vorticity field is expressed as summation of the vorticities on vortex elements. The origin of this method was in the study of point vortices and surface vortex distributions in the 1930s. However, the vortex method as a computational tool was introduced by Chorin (1968) and Leonard (1980).

The main difficulties in the vortex method are the complexity in modeling viscous terms and calculation of the velocity components. Moreover, in FSI problems this method should be coupled with a computational method capable of modeling the solid parts.

1.3.7. Particle in Cell Method

In the particle in cell (PIC) method, a set of particles is tracked in the Lagrangian frame of reference, then their properties are interpolated on Eulerian mesh points. This

method is a combination of Lagrangian and Eulerian approaches. The process of exchange between the two frames of reference and the related interpolation process is computationally time consuming.

The early use of this method was in 1955 by Harlow, and the work of Brackbill and Ruppel (1986) which presented a successful application of PIC to simulate fluid flow.

1.3.8. Smoothed Particle Hydrodynamics Method

Smoothed particle hydrodynamics (SPH) is a fully Lagrangian meshfree method created originally to simulate compressible flow in astrophysics by Lucy and at the same time by Gingold and Monaghan in 1977. The physical domain is discretized by a number of particles. Each particle has its own physical properties. Numerical discretization involves approximation of the physical properties of each particle by interpolating the properties of its neighboring particles. The application of the SPH method in engineering began around 1994 (Monaghan, 1994). SPH can be applied in both fluid and solid dynamics and therefore FSI can be performed with less difficulty compared to mesh-based methods.

Table 1.1 provides a general comparison between mesh-based and meshfree methods, emphasizing the advantages and disadvantages for each.

Table 1.1. Comparison between mesh-based and meshfree methods.

Numerical Complications	Mesh-based Methods	Meshfree Methods
Mesh generation	time consuming, needed in the entire domain	no need (at least for discretization of equations)
Complicated and irregular geometries	great effort to mesh and model	less effort to model
Moving and large deformation boundaries	mesh distortion, need to re-meshing process which is computationally expensive	less effort to model
3D problems	difficult, especially in irregular and moving boundaries	2D algorithm can be extended to 3D with less difficulty than in mesh-based methods
Time history of material elements	not easy to get, needs coupling with a Lagrangian method	easy to get
Algorithm and procedures	developed	under development
Time step	depends on the selected algorithm and procedure	smaller than in mesh-based methods
Accuracy and stability	Already known with high accuracy and stability	have reached an acceptable level for engineering applications

A comparison between different types of meshfree methods with emphasis on SPH advantages is provided in Table 1.2.

Table 1.2. A comparison between SPH and other meshfree methods. (Adapted from Liu and Liu, 2003; Liu, 2010)

Conventional Meshfree Methods		**Smoothed Particle Hydrodynamics Method**
Molecular Dynamics Method	Applicable for modeling systems at molecular level	Applications are from micro to macro-scale.
Monte Carlo Method	Iterative method based on stochastic and perturbation theory	Do not use random numbers and stochastic theories.
Lattice Boltzmann Method	In FSI problems, needs to be coupled with other methods capable of modeling solid part.	Capable of solving solid and fluid dynamic equations in the same algorithm.
Element Free Galerkin Method	Use background mesh for integration; not a fully meshfree method.	Completely a meshfree method.
Immersed Boundary Method	Need a background mesh for integration of flow equations; not straightforward to simulate cases with variable fluid viscosity and solid elasticity.	Completely a meshfree method; variable properties can be considered without difficulty.
Vortex Method	Not able to simulate solid mechanic equations; velocity components and pressure are not computed directly.	Capable of solving solid and fluid dynamic equations; velocity components and pressure are derived directly.
Particle in Cell Method	A combination of Lagrangian-Eularian approaches and a form of mesh is needed.	Completely a Lagrangian meshfree method.

1.4. Summary

Smoothed particle hydrodynamic is selected in this thesis as a promising candidate to simulate problems in cardiovascular fluid dynamics due to the following reasons:

1) The accuracy and stability of this method has reached an acceptable range for engineering applications.

2) Direct tracking of real fluid particles in the domain allows determination of the fluid elements' residential time which can be linked to risk of damage to blood components.

3) There is no need for the process of mesh generation and regeneration in the simulation of problems with complex geometry and large deformation as in the cardiovascular system.

4) SPH method is suitable for parallel computation.

5) Its applications are very wide from fluid to solid mechanics and from micro-scale to macro-scale problems.

Chapter 2

Smoothed Particle Hydrodynamics Method

This chapter focuses mainly on fundamental concepts, mathematical formulation, and implementation techniques in the SPH method.

2.1. Introduction

Smoothed particle hydrodynamics is a fully Lagrangian meshfree particle method capable of satisfying conservation properties of continuum physical systems. The method was originally developed to model compressible flow in astrophysical phenomena by Lucy (1977) and Gingold and Monaghan (1977). Although the primary model did not exactly conserve the linear and angular momentum, it led to promising results in the simulation of complex behavior of celestial bodies (see Fig. 2.1).

During the last two decades, the initial algorithm of SPH was improved to satisfy the conservation of momentum and energy and its applications have been extended rapidly to simulation of a variety of continuum solid and fluid mechanics phenomena (Libersky and Petschek, 1991; Monaghan, 1994). During the first developmental stage, the method was applied to shock tube problems by introducing the concept of artificial viscosity (Monaghan and Gingold, 1983).

The idea of using the artificial equation of state to calculate the static pressure in incompressible flow systems opened a new perspective to apply this method to a wide range of problems in fluid mechanics. The first attempt to simulate inviscid water flows subject to gravitational force was performed by Monaghan in 1994.

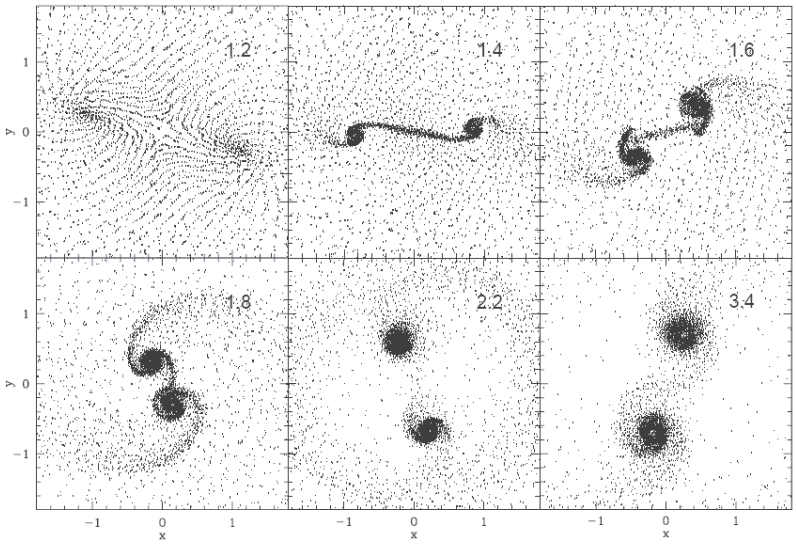

Fig. 2.1. Simulation of star formation using SPH. (Bate, 1995)

There has been increasing interest among researchers, especially in hydraulic engineering, to apply and develop the SPH algorithm, increase its accuracy, and extend its application to simulate a variety of physical phenomena.

The problems of solitary waves, breaking waves, shallow water and dam breakdown are among the first class of problems which have widely used the SPH method (Monaghan, 1994; Monaghan and Kos, 1999). Conventional computational methods have several difficulties simulating free surface flow and need to employ a two-phase flow modeling approach.

As the dominant force field in cosmological systems is the magnetic field, the SPH formulation in the presence of a magnetic field was investigated and applied to simulate Magnetohydrodynamics (MHD) problems (Price and Monaghan, 2004; Jiang et al., 2006).

Smoothed particle hydrodynamics has also been applied to simulate industrial die casting processes (Cleary et al., 2002). The SPH method has been shown to capture more details of the flow and free surface waves than the volume of fluid (VOF) method when compared with experimental studies. The VOF method suffers from several limitations such as numerical oscillations and implementation complexities.

The application of SPH is not limited to the fore-mentioned problems and has been extended to simulate other fields in fluid dynamics including multi-phase flows (Monaghan and Kocharyan, 1995; Richie and Thomas, 2001; Hu and Adams, 2006), flow through porous media (Zhu et al., 1999), viscoelastic flows (Ellero et al., 2002) and interacting and interfacial fluid flows (Monaghan et al., 1999; Colagrossi and Landrini, 2003). Most SPH simulations of internal incompressible flow were performed at low Reynolds number (Morris et al., 1997; Sigalotti et al., 2003).

Smoothed particle hydrodynamics is also highly flexible in terms of adding new physics and can easily be extended to three dimensions (Cleary et al., 2002; Gomez-Gesteira and Dalrymple, 2004). In SPH literature, turbulence modeling has not been adequately investigated and has been applied mainly to simulate free surface flows in coastal engineering (Shao and Gotoh, 2004; Ting et al., 2005; Dalrymple and Rogers, 2006; Violeau and Issa, 2007).

Smoothed particle hydrodynamics has also been applied to simulate the elastic dynamic behavior of solids with large deformation and structural distortion as well as the development of fractures in solid mechanics (Libersky L, Petschek, 1991; Wingate and Stellingwerf, 1994; Benz and Asphaug, 1995; Randles and Libersky, 1996; Bonet and Kulasegaram, 2000; Gray et al., 2001). For fluid structure interactions, an elastic gate interacting with water in a free surface tank behind the gate has recently been modeled (Antoci et al., 2007).

New approaches have also emerged to overcome the time step constraint and the compressibility effect existing in classical SPH method (Cummins and Rudman, 1999; Lee et al., 2008). Although SPH has been successfully applied to different fields in fluid and solid mechanics, several aspects of the method are still under development.

2.2. Mathematical Formulation

2.2.1. SPH Formulation

In SPH, a continuum domain is discretized by a set of particles. Each particle has its own physical properties that are statistically interpolated using the properties of its neighboring particles.

To interpolate the value of any physical property A at position $\boldsymbol{r}$ in the domain, the concept of integral interpolant (Monaghan, 1992) is used as

$$A(\boldsymbol{r}) = \int A(\acute{\boldsymbol{r}})W(\boldsymbol{r} - \acute{\boldsymbol{r}}, h)d\acute{\boldsymbol{r}} \tag{2.1}$$

where h is the smoothing length that determines the size of neighboring domain and $W(\boldsymbol{r} - \acute{\boldsymbol{r}}, h)$ is the weighting function or so called interpolating kernel which is a symmetric function. This kernel function has a similar appearance to the Gaussian

function, but with a specified supporting size. The kernel should be normalized and treats as a Dirac delta function when h tends to zero.

This integral is approximated using a summation operator (Monaghan, 1992) to be applicable numerically as

$$A(\boldsymbol{r}) = \sum_b m_b \frac{A_b}{\rho_b} W(\boldsymbol{r} - \boldsymbol{r_b}, h) \tag{2.2}$$

where A_b presents each physical property at particle b with mass of m_b, density of ρ_b, and position of $\boldsymbol{r_b}$ within the neighboring domain (limited by the influence length of the kernel) of a particle located at position $\boldsymbol{r}$.

The concept of SPH interpolation, neighboring particles (b) of a given particle (a) and the interpolating function W_{ab} ($= W(\boldsymbol{r_a} - \boldsymbol{r_b}, h)$) are shown in Fig. (2.2).

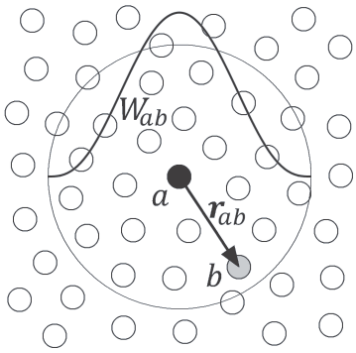

Fig. 2.2. The main idea of SPH: Kernel function, supporting domain and neighboring particles.

2.2.2. Interpolating Kernel Function

The weighting function or interpolating kernel, is one of the most important factors in SPH formulation. A kernel function defines the interpolation form and determines the dimensional influence of the neighboring domain. This function should have several

properties as being normalized and treated as a Dirac delta function when the smoothing length tends to zero (Liu et al., 2003). The first applications of SPH used a Gaussian kernel. Since then, different forms of kernel functions have been constructed and proposed in the literature.

The most commonly used kernel function is in the form of a cubic spline. The cubic spline, when compared with higher order splines, has less computational cost, but shows lower stability. The standard form of the cubic spline kernel for 2D simulations is shown below (Morris et al., 1997) as

$$W_{ab} = \frac{10}{7\pi h^2}\begin{cases} 1 - \frac{3}{2}q^2 + \frac{3}{4}q^3 & 0 \le q < 1 \\ (2-q)^3/4 & 1 \le q < 2 \\ 0 & 2 \le q \end{cases} \tag{2.3}$$

where $q = \boldsymbol{r}_{ab}/h$.

The fourth order, quartic, spline kernel (Violeau and Issa, 2007) has the form of

$$W_{ab} = \frac{96}{1199\pi h^2}\begin{cases} (\frac{5}{2}-q)^4 - 5(\frac{3}{2}-q)^4 + 10(\frac{1}{2}-q)^4 & 0 \le q < 0.5 \\ (\frac{5}{2}-q)^4 - 5(\frac{3}{2}-q)^4 & 0.5 \le q < 1.5 \\ \left(\frac{5}{2}-q\right)^4 & 1.5 \le q < 2.5 \\ 0 & 2.5 \le q \end{cases} \tag{2.4}$$

Compared to the cubic kernel, this type of kernel has higher stability, but a wider influence domain which leads to higher computational time. The supporting size of these kernel types is $2h$ and $2.5h$, respectively.

Using Eq. (2.2) and its derivatives, the governing equations of the fluid dynamics can be rewritten in the form of SPH formulation. In classical SPH, a weakly compressible fluid concept is used to formulate the governing equations of an incompressible flow.

2.2.3. Navier-Stokes Equations

The Navier-Stokes equations in Lagrangian form are

$$\frac{d\rho}{dt} + \rho \boldsymbol{\nabla}.\boldsymbol{V} = 0 \tag{2.5}$$

$$\rho \frac{d\boldsymbol{V}}{dt} = \boldsymbol{f}_{body} - \boldsymbol{\nabla} P + \mu \nabla^2 \boldsymbol{V} \tag{2.6}$$

where t is for time, ρ is fluid density, $\boldsymbol{V}$ is the velocity vector, and $\boldsymbol{f}_{body}$ is the body force indicating the applied forces per unit volume of the fluid element due to the external fields. P is thermodynamic pressure and μ is dynamic viscosity.

2.2.4. Conservation of Mass

In SPH, the conservation of mass for a fluid particle (a) leads to calculation of the particle density at its local position ($\boldsymbol{r}_a$). Two types of formulations are presented based on the summation and continuity density methods.

The first SPH formulation for conservation of mass was derived directly from the summation interpolant, Eq. (2.2), as

$$\rho_a = \sum_b m_b W_{ab} \tag{2.7}$$

here $\rho_a = \rho(\boldsymbol{r}_a)$ and $W_{ab} = W(\boldsymbol{r}_a - \boldsymbol{r}_b, h)$.

The time derivative form of the conservation of mass (Monaghan, 1992) leads to

$$\frac{d\rho_a}{dt} = \sum_b m_b (\boldsymbol{V}_a - \boldsymbol{V}_b).\boldsymbol{\nabla}_a W_{ab} \tag{2.8}$$

where $\nabla_a W_{ab}$ is the gradient of the kernel function with respect to coordinates of the given particle (a). In this study, to evaluate the density of particle a, Eq. (2.8) is employed because of its advantages compared to Eq. (2.7) (Morris et al., 1997;

Monaghan 1992). Equation (2.8) is more appropriate for liquids and links the rate of density change to the relative velocity of the particles within the support domain. It also creates an even distribution of weight ensuring stability in density calculations based on the interaction between velocity and pressure changes and reduces the computational time.

2.2.5. Conservation of Momentum

To formulate the conservation of momentum under the SPH scheme, pressure and viscous terms need to be modeled. In the literature, different forms for both terms have been suggested (Monaghan, 1992; Cleary, 1998; Monaghan, 2006).

The conventional type for the pressure gradient is the symmetric form as it satisfies the conservation of linear and angular momentum. The pressure gradient can be rewritten as (Monaghan, 1992)

$$\frac{\boldsymbol{\nabla} P}{\rho} = \frac{P}{\rho^{\sigma}} \boldsymbol{\nabla} \left(\frac{1}{\rho^{1-\sigma}} \right) + \frac{1}{\rho^{2-\sigma}} \boldsymbol{\nabla} \left(\frac{P}{\rho^{\sigma-1}} \right) \tag{2.9}$$

and then

$$\left(\frac{\boldsymbol{\nabla} P}{\rho} \right)_a = \sum_b m_b \left(\frac{P_b}{\rho_a^{2-\sigma} \rho_b^{\sigma}} + \frac{P_a}{\rho_a^{\sigma} \rho_b^{2-\sigma}} \right) \boldsymbol{\nabla}_a W_{ab} \tag{2.10}$$

This form is symmetric for all values of parameter σ. The most prevalent type of the symmetric form is the one for $\sigma = 2$,

$$\left(\frac{\boldsymbol{\nabla} P}{\rho} \right)_a = \sum_b m_b \left(\frac{P_b}{\rho_b^2} + \frac{P_a}{\rho_a^2} \right) \boldsymbol{\nabla}_a W_{ab} \tag{2.11}$$

An alternative symmetric formulation for the pressure gradient is

$$\left(\frac{\nabla P}{\rho}\right)_a = \sum_b m_b \left(\frac{P_a + P_b}{\rho_a \rho_b}\right) \nabla_a W_{ab} \tag{2.12}$$

This form is variationally consistent (Colagrossi and Landrini, 2003) and was shown to give slightly superior results compared to the conventional pressure gradient term (Vila, 1999).

For SPH simulations, incompressible flow is approximated as a slightly compressible flow. It is done by using an artificial equation of state to relate density to pressure, while the continuity equation is used to evolve the density over time. The use of a quasi-incompressible equation of state is justified by the fact that the actual equation of state leads to a very small time step. In SPH literature, a stiff equation of state is often used for simulations with water as (Monaghan, 1994)

$$P = P_0\left(\left(\frac{\rho}{\rho_0}\right)^{\gamma} - 1\right) \tag{2.13}$$

where P_0 is pressure at the reference density of ρ_0 and γ is the specific heat ratio. As this equation has been recommended for modeling free surface flows and is sensitive to density fluctuations, in this work the following equation of state is used (Morris et al., 1997):

$$P = c^2 \rho \tag{2.14}$$

where c is the speed of sound. This equation has shown minimal sensitivity to density fluctuations and is more suitable for the type of flows simulated in this thesis as there is no development of a free surface. In terrestrial applications of fluid mechanics, the speed of sound is high compared to the bulk velocity of the fluid, therefore an artificial sound speed should be employed to avoid very small computational time steps while keeping

density fluctuations within an acceptable range (1 to 3%, in order to maintain incompressible flow behavior). A value of 0.1 or less is suggested as an approximate value for Mach number to specify the artificial sound speed (Monaghan, 1994; Morris et al., 1997).

For the viscous term, the first expression proposed comes from the concept of artificial viscosity used to limit non-physical post shock oscillations in the original SPH algorithm dealing with inviscid flows (Monaghan, 1992; Monaghan, 1994). The most commonly used form is similar to the Von Neumann-Richtmyer viscosity in mesh-based methods. In SPH, it is presented as a combination of shear and bulk viscosity when the particles are approaching each other. In this approach the viscosity force per unit mass of a fluid particle can be modeled as

$$\left(\frac{\mu}{\rho}\nabla^2\boldsymbol{V}\right)_a = \sum_b m_b \frac{\alpha \bar{c}_{ab}\mu_{ab}}{\bar{\rho}_{ab}} \boldsymbol{\nabla}_a W_{ab} \tag{2.15}$$

with addition of the following term (Ellero et al., 2002),

$$-\sum_b m_b \frac{\beta \mu_{ab}^2}{\bar{\rho}_{ab}} \boldsymbol{\nabla}_a W_{ab} \tag{2.16}$$

where μ_{ab} is defined as

$$\mu_{ab} = \frac{h\boldsymbol{V}_{ab}\cdot\boldsymbol{r}_{ab}}{r^2+\eta^2} \tag{2.17}$$

here $\bar{c}_{ab} = (c_a + c_b)/2$ is average artificial sound speed, $\bar{\rho}_{ab} = (\rho_a + \rho_b)/2$ is average density, $\boldsymbol{V}_{ab} = \boldsymbol{V}_a - \boldsymbol{V}_b$ and $\boldsymbol{r}_{ab} = \boldsymbol{r}_a - \boldsymbol{r}_b$. The order of α is around 1 and $\beta = 2\alpha$. The η^2 is a small term to avoid the singularity ($\eta^2 = 0.01h^2$).

The artificial viscosity should be applied only when a compression is happening (particles are approaching each other). Using this approach to model the real viscosity leads to spurious viscosity in areas away from the compression region and the fluid shows a more viscous behavior. To eliminate this unphysical effect, several attempts have been made and several types of artificial viscosities have been proposed. The common treatment is to multiply equation (2.16) by (Balsara, 1995; Morris and Monaghan, 1997)

$$\bar{f}_{ab} = \frac{f(a)+f(b)}{2} \tag{2.18}$$

where,

$$f(a) = \frac{|(\boldsymbol{\nabla}.\boldsymbol{V})_a|}{|(\boldsymbol{\nabla}.\boldsymbol{V})_a|+|(\boldsymbol{\nabla}\times\boldsymbol{V})_a|+0.0001c/h} \tag{2.19}$$

In this way, the production of unphysical viscosity is limited only to the region of compression. Although this model is still adopted by some literature, it will not be used in this study as the viscous force results in unrealistically high viscous effects.

A standard form to model the real viscous force, presented in its original form, is (Monaghan, 1994; Violeau and Issa, 2007)

$$\left(\frac{\mu}{\rho}\nabla^2\boldsymbol{V}\right)_a = \sum_b m_b \frac{16}{\rho_a\rho_b}\frac{\mu_a\mu_b}{(\mu_a+\mu_b)}\frac{\boldsymbol{V}_{ab}.\boldsymbol{r}_{ab}}{\boldsymbol{r}_{ab}^2}\boldsymbol{\nabla}_a W_{ab} \tag{2.20}$$

This form was developed originally to simulate free surface flows and then has been widely used for other types of flow. It should be noted however that Cleary (1998) proposed and applied successfully a calibration coefficient for Eq. (2.20) based on a series of numerical tests. The proposed coefficient still needs to be generalized for different kernel functions. This is also the case for a new suggested formulation for

modeling viscous force in shear flows which possesses a dependent coefficient (Monaghan, 2006).

Another formulation used to model the viscous term is obtained from a combination of standard SPH and finite difference approximations of the first derivative. This formulation was originally presented to model the viscous term at low Reynolds number flows (Morris et al, 1997). The term, in its original form, is presented as

$$\left(\frac{\mu}{\rho}\nabla^2 \boldsymbol{V}\right)_a = \sum_b m_b \frac{(\mu_a+\mu_b)\boldsymbol{r}_{ab}.\boldsymbol{\nabla}_a W_{ab}}{\rho_a \rho_b \, r_{ab}^2} \boldsymbol{V}_{ab} \tag{2.21}$$

The above formulation leads to conservation of linear momentum, while angular momentum is approximately conserved. In addition to being computationally efficient, it is also less influenced by computational errors in cases with low particle numbers (Morris et al., 1997).

In Chapter 3 of this thesis, the accuracy of these two standard forms, Eqs. (2.20) and (2.21), is investigated under moderate Reynolds number flow conditions.

2.2.6. Turbulence Modeling

Turbulence modeling is not frequently reported in the SPH literature and is mainly applied to simulate free surface flows (Shao and Gotoh, 2004; Ting et al., 2005; Dalrymple and Rogers, 2006; Violeau and Issa, 2007). Monaghan in 2002 provided a SPH version of the alpha turbulence model for compressible flows. A large eddy simulation (LES) was applied by Shao and Gotoh in 2004 to wave propagation in coastal applications. Dalrymple and Rogers in 2006 introduced a sub-particle scaling technique using the LES approach in modeling breaking waves on beaches. Violeau and Issa in 2007 presented a review on the recently adopted turbulence models to the SPH method

and applied mixing length, $k-\epsilon$ model, explicit algebraic Reynolds stress model (EARSM) and large eddy simulation (LES) to free surface flows.

In this thesis, the effect of turbulent fluctuations on mean flow is modeled using one equation $k-l_m$ turbulence model (Wilcox, 2006; Violeau and Issa, 2007). The model is easy to code and computation takes less time than complex turbulence models, while being able to give reasonable results. (see Chapter 5)

In Reynolds averaged Navier-Stokes (RANS) momentum equations, the effective viscosity is defined as

$$\mu_e = \mu + \rho\nu_T \tag{2.22}$$

where μ is dynamics viscosity, ρ is density and ν_T is turbulent eddy viscosity.

Turbulent eddy viscosity corresponding to particle a is given by

$$\nu_{t,a} = C_\mu \frac{k_a^2}{E_a} \tag{2.23}$$

where k_a is turbulent kinetic energy, E_a is energy dissipation rate for particle a, and $C_\mu = 0.07 - 0.09$. Turbulent kinetic energy for particle a is written as

$$\frac{dk_a}{dt} = P_a - E_a + \sum_b m_b \frac{(\mu_{k,a}+\mu_{k,b})k_{ab}}{\rho_a\rho_b \boldsymbol{r}_{ab}^2} \boldsymbol{r}_{ab}.\boldsymbol{\nabla}_a W_{ab} \tag{2.24}$$

where P_a indicates production of kinetic energy associated with particle a, $k_{ab} = k_a - k_b$, $\mu_k = \mu + \mu_T/\sigma_k$ and $\sigma_k = 1$. The production of kinetic energy considered in its classical form is given by

$$P_a = \nu_{T,a} S_a^2 \tag{2.25}$$

where, S_a is mean strain rate for particle a. Violeau and Issa (2007) suggested

$$S_a^2 = -\frac{1}{2}\sum_b m_b \frac{(\rho_a+\rho_b)\boldsymbol{u}_{ab}^2}{\rho_a\rho_b \boldsymbol{r}_{ab}^2}\boldsymbol{r}_{ab}.\boldsymbol{\nabla}_a W_{ab} \quad (2.26)$$

and the dissipation rate is computed using

$$E_a = C_\mu^{\frac{3}{4}}\frac{k_a^{\frac{3}{2}}}{l_m} \quad (2.27)$$

where l_m is mixing length.

2.3. Numerical Features

2.3.1. Particle Movement and XSPH Variant

Fluid particles move in a Lagrangian frame of reference based on

$$\frac{d\boldsymbol{r}_a}{dt} = \boldsymbol{V}_a \quad (2.28)$$

The new position of particles is derived by time integration of the velocity at each instant. In SPH literature, a variant, referred to as XSPH, is proposed with the goal of modifying and smoothing SPH particle movements based on the average velocity of their neighboring particles (Monaghan, 1992) as

$$\frac{d\boldsymbol{r}_a}{dt} = \boldsymbol{V}_a + \varepsilon\sum_b m_b \frac{(\boldsymbol{V}_b-\boldsymbol{V}_a)}{(\rho_a+\rho_b)/2}W_{ab} \quad (2.29)$$

where, ε is a constant between 0 and 1. The accuracy of both approaches (Eqs. 2.28 and 2.29) will be investigated in Chapter 3.

2.3.2. Time Integration

A second order accurate time integration scheme, predictor-corrector algorithm, is used for time integration of governing equations (Monaghan, 1989). For a differential equation in the general form of

$$\frac{dy}{dt} = f \tag{2.30}$$

the predictor part consists of an explicit half time step integration as

$$y^{n+\frac{1}{2}} = y^n + \frac{\Delta t}{2} f^n \tag{2.31}$$

followed by a corrector part to correct the approximated properties in the previous part as

$$y^{n+\frac{1}{2}} = y^n + \frac{\Delta t}{2} f^{n+\frac{1}{2}} \tag{2.32}$$

Finally, the properties at the new time step are calculated based on the values obtained at predictor and corrector steps as

$$y^{n+1} = 2y^{n+\frac{1}{2}} - y^n \tag{2.33}$$

At each step, pressure is calculated using the equation of state. The structure of predictor-corrector algorithm is presented in Appendix A.

2.3.3. Variable Time Step

The time step in SPH is usually derived based on the three well-known criteria that are governed by the Courant-Friedrichs-Levy (CFL) condition, external force and viscous diffusion terms (Monaghan, 1992; Morris et al., 1997). The variable time step should be chosen so

$$\Delta t \leq min\left\{0.25\frac{h}{c}, 0.25\sqrt{\frac{h}{max|\boldsymbol{f}_a|}}, 0.125\frac{h^2}{\nu}\right\} \tag{2.34}$$

where $|\boldsymbol{f}_a|$ is the force magnitude per mass unit of a particle. This inequality states that the maximum speed of numerical propagation cannot exceed the maximum speed of

physical propagation. A variable time step is used according to Eq. (2.34) to obtain a reasonable compromise between computational efficiency and stability.

2.3.4. Search of the Neighboring Particles- Linked List Method

In contrast to mesh-based methods where the neighboring nodes for each node are clearly defined, in Lagrangian particle methods, the neighboring particles for each particle are changing with time and need to be found at each time step.

The simplest way to find the neighboring particles, b, of the particle under consideration, a, within the kernel supporting size is to calculate the distance of all particles in the domain from particle a and compare it with the kernel supporting size. This approach generates a long computational time (order of N^2), where N is the number of particles in the domain. As a consequence, this simple method is usually limited to one dimensional problems.

An efficient method to optimally search for neighboring particles is to employ a linked list method (Dominguez et al., 2010). In this method, an imaginary Cartesian network of cells, with dimensions corresponding to the kernel supporting size, is constructed on the domain (Fig. 2.3). After updating the particle positions at each time step, it is possible to determine how many and which particles are positioned in a specific cell in the domain. Therefore, only particles in the same cell as the particle of interest, a, and in its neighboring cells are considered (in 2D simulations, 9 cells). Applying this method reduces the computational time to the order of $N\,logN$. This method is not applicable when variable influence length is used.

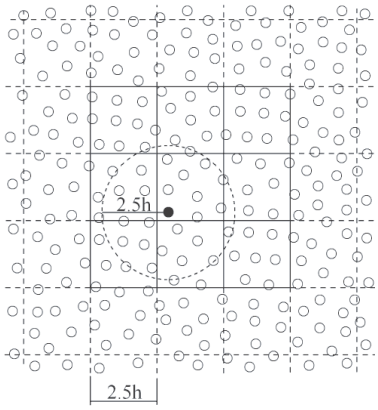

Fig. 2.3. Imaginary cells used to search the neighboring particles of a given particle using link list method. The dimension of the cells is based on the selected interpolating function (for quartic spline kernel is $2.5h$).

The codes developed to search neighboring particles based on linked list method and to calculate the SPH approximations are provided in Appendix B.

2.3.5. Periodic Boundary Condition

The periodic boundary condition is used to model a large physical domain by simulating only a part of the domain. A schematic of this technique is depicted in Fig. (2.4). Particles near a boundary interact with the particles near the opposite boundary.

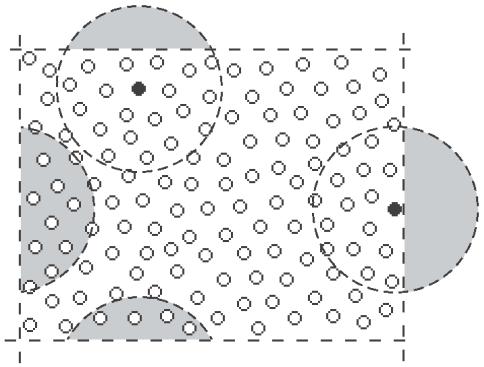

Fig. 2.4. Periodic boundary condition.

To conserve mass within the region of interest, exited particles from the region enter again from the opposite side with the same physical properties.

2.3.6. Rigid Boundary Conditions

Wall boundary treatment in SPH requires special attention since the particles near the boundaries do not have enough particles in their neighboring domain (the kernel is truncated). This leads to incorrect computation of density and pressure. Simply setting the velocity of the particles on the stationary walls to zero cannot prevent entirely fluid particles from penetrating rigid walls.

Therefore, different techniques have been developed in order to model wall boundaries. One method is to apply a form of Lennard-Jones force to the fluid particles approaching the wall (Fig. 2.5). The force per unit mass of the particle can be modeled as a function of distance, $\boldsymbol{r}$, between a wall particle and approaching fluid particles. This is expressed as (Monaghan, 1994)

$$f(\boldsymbol{r}) = D\left(\left(\frac{r_0}{r}\right)^{12} + \left(\frac{r_0}{r}\right)^{6}\right)\frac{\boldsymbol{r}}{r^2} \tag{2.35}$$

where r_0 is initial particle spacing and D is a coefficient dependent on the physical characteristics of the problem. Different forms of this technique have been presented to improve particle movements near the boundaries.

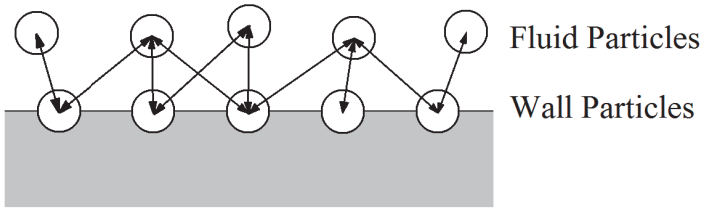

Fig. 2.5. No slip boundary condition; Attraction and repulsion between wall and fluid particles.

An alternative method is to use mirror particles which are created by reflecting particles approaching the walls (reflection with respect to the wall boundary). These mirror particles have the same density and pressure as their reference fluid particles, but a velocity vector with opposite direction (Cummins and Rudman, 1999).

Another technique considers some fixed particles outside the wall boundaries with an extrapolated velocity to satisfy the zero velocity condition on the wall (Takeda et al., 1994; Morris et al., 1997). In this case, an artificial velocity is allocated to each particle based on

$$\boldsymbol{V}_{ab} = \beta \boldsymbol{V}_a \tag{2.36}$$

such that

$$\beta = \min\left(\beta_{max}, 1 + \frac{d_b}{d_a}\right) \tag{2.37}$$

where $\boldsymbol{V}_{ab}$ is the relative velocity between fluid particle $'a'$ and the imagined fixed particle $'b'$ located outside the wall boundary (Fig. 2.6). In Eq. (2.37), d_b is the normal distance of particle $'b'$ to the tangent line at the wall curvature drawn in the direction of the normal distance of fluid particle $'a'$, d_a, to the wall. The β_{max} parameter is set to 1.5. (Morris et al., 1997)

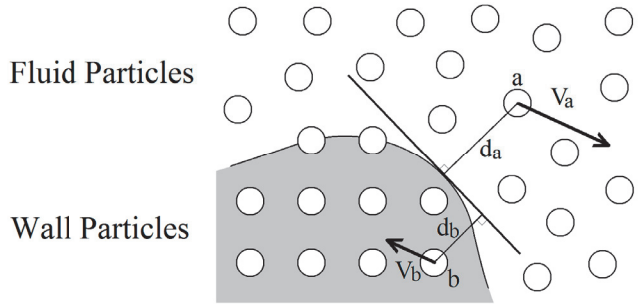

Fig. 2.6. No slip boundary condition; Fixed boundary particles with artificial velocity.

The rigid wall boundaries can also be implemented by placing a set of finite particles exactly on the wall boundaries (located at the same distance as the initial fluid particles) along with layers of fixed imaginary particles constructed outside the boundaries parallel to the walls. This technique is similar to considering dummy particle layers on the boundary (Koshizuka et al., 1998; Shao and Lo, 2003; Violeau and Issa, 2007). The wall and the dummy particles have zero velocity. To easily apply a Neumann type boundary condition for pressure on the walls, imaginary particles can be arranged such that each one is allocated to a normal line drawn from a wall particle. Implementation of this idea is presented in Fig. (2.7).

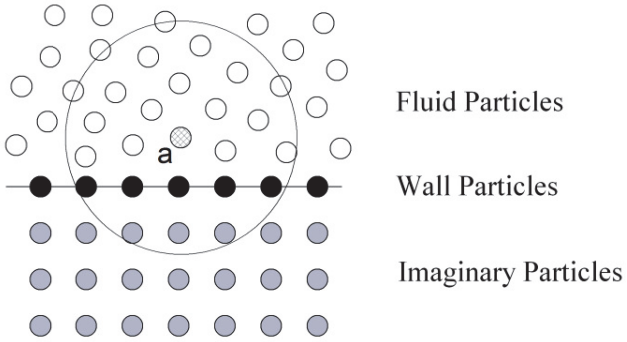

Fig. 2.7. No slip boundary condition; Wall particles and three layers of imaginary particles.

2.4. Summary

This chapter presented the historical development of SPH methodology from its origin in astrophysics to terrestrial applications. The SPH method concept, mathematical formulation, different discretization for Navier-Stokes equations including viscous and pressure gradient terms and one equation, $k - l_m$, turbulence modeling under SPH formulation were described. Numerical features of the method, including standard and modified equations for particle movement, second order predictor-corrector time

integration algorithm, variable time step and linked-list method to search neighboring particles were provided. Different techniques in the treatment of the no-slip and periodic boundary conditions were explained.

Chapter 3

Verification of Smoothed Particle Hydrodynamics Methodology and Validation of Developed Code

This chapter aims to verify the accuracy of SPH methodology, provided in chapter 2, and validate the ability of the computational code developed to simulate steady and oscillating flows under flow characteristics similar to those found in the cardiovascular system. The required modifications are presented and the relation between particle resolution and sound speed to control compressibility effects and order of convergence in SPH simulations are demonstrated.

3.1. Introduction

Although the SPH method has passed its preliminary development stage, several studies are ongoing to improve the algorithm, verify its accuracy and discover new implementation features.

Most of the reported unsteady incompressible flow simulations using SPH are limited to free surface problems including dam breaking, shallow water and wave flumes (Gomez-Gesteira et al., 2010). The SPH method has proven to be capable of successfully simulating transient start up of internal steady flows due to constant driving forces for low Reynolds numbers, typically compressible flows with $Re \leq 55$ (Takeda et al., 1994),

incompressible flows with $Re \leq 1$ (Morris et al., 1997; Sigalotti et al., 2003) and viscoelastic flows with $Re \leq 2.5$ (Ellero et al., 2002). An attempt has been made to explain the transition to turbulence in a start up Poiseuille flow in the presence of a streamwise magnetic field (Jiang et al., 2006), but the comparison with an exact solution was not reported and flow patterns were only presented qualitatively.

Most fluid flow phenomena in science and engineering vary with time at discrete locations and occur throughout a wide range of Reynolds numbers. For example, cardiovascular flows are characterized by moderate Reynolds numbers and unsteadiness due to the oscillatory driven forces and boundary movements.

In this chapter, the transient behavior of Poiseuille flow is simulated for a range of Reynolds numbers up to 1500. For this benchmark case, the two most referred standard formulations to model viscous force suggested by Monaghan et al. (1994) and by Morris et al. (1997) are examined. In addition, the effect of the XSPH variant, suggested to keep the movement of each particle consistent with the average velocity of its neighboring particles, on particle distribution is investigated. Then, the capability of SPH to simulate unsteady flows induced by an oscillating pressure difference (Womersley type flow: $W_o = 1$ and 10) and an oscillating moving boundary (Stokes' second problem) with various frequencies ($\omega = \pi\ (\mathrm{rad/s})$ and $10\pi\ (\mathrm{rad/s})$) and amplitudes is examined. An applied formulation is introduced to approximate the wall shear stress in SPH. This formulation can also be used with other particle methods. Indeed, an accurate determination of wall shear stress is of primary importance for several applications and in particular for physiological flows where it is well correlated with damage to the cells lining blood vessels (Traub and Berk, 1998).

The results for SPH simulation of lid-driven cavity flow are presented and compared to reference data. This was performed because the flow characteristics induced, mainly by a large recirculation zone, are close to the ones observed in the human heart during the late filling phase. Furthermore, this test is also frequently considered as a benchmark for numerical simulations since reference data are available up to high Reynolds numbers. In SPH literature, the simulation of steady internal flows at high Reynolds numbers are reported (Ting et al., 2005), but the SPH simulations of lid-driven cavity flow are at Reynolds numbers up to 1000 (Basa et al., 2009; Lee et al., 2008). In the present study, flows with higher Reynolds numbers ($Re = 3200$ and 5000) are considered. These values are selected to show the ability of SPH to simulate this kind of flow in laminar regime up to the onset of turbulence, occurring between 6000 and 8000 (Koseff and Street, 1984; Shankar and Deshpande, 2000). In this simulation, an interesting feature of SPH related to the link between particle resolution and sound speed to control the compressibility effects is demonstrated.

3.2. Methodology and Formulations

The conservation of mass and momentum for a fluid element (particle) in an incompressible flow are expressed as Eqs. (2.5) and (2.6).

The time derivative form of the conservation of mass, Eq. (2.8), is used to calculate particle density. In the equation of motion, the common symmetric form, Eq. (2.11), is used for the pressure term, and the quasi-incompressible equation of state, Eq. (2.14), is employed to relate density to pressure. In this chapter, the accuracy of the two standard forms to model the viscous term is investigated under moderate Reynolds number flow

conditions. Since modeling the viscous term based on the concept of artificial viscosity, Eq. (2.15), creates unrealistic viscous effects, the standard forms of Eq. (2.20), refers to "*Form I*" and Eq. (2.21), refers to "*Form II*", are considered in this study. Particle movements are studied based on the standard Eq. (2.28) and the modified Eq. (2.29).

The quartic spline kernel, based on Eq. (2.4), is used to construct the interpolation form due to its high stability. The time integration of the governing equations is performed using predictor-corrector algorithm, a second order accurate time integration scheme (see Sec. 2.3.2).

The no slip boundary conditions are implemented by placing a finite number of particles exactly on the wall boundaries and adding several layers of fixed imaginary particles parallel to the boundaries outside the domain (Fig. 2.7). There is no need to create mirror particles at each time step as in Cummins and Rudman (1999). These particles are placed in such a way to have the same spacing as the initial fluid particles. This ensures that fluid particles near the plates have enough homogeneous distribution of particles in their domain. So far, this implementation is similar to the technique which uses a series of dummy particle layers on the walls with zero velocity (Koshizuka et al., 1998). In the present simulations, an extrapolated artificial velocity is allocated to the imaginary particles based on the velocity of the fluid particles approaching the plates (Eq. 2.36). The velocity of the wall boundary particles is set to zero. The periodic boundary condition is applied at inlet and outlet boundaries to conserve the mass within the domain.

3.3. Poiseuille Flow

The Poiseuille flow consists of the movement of a fluid between two infinite parallel plates similar to the flow in channels and pipes. There is no applied pressure difference in the vertical direction and the fluid is driven by an axial pressure difference resulting in a flow parallel to the plates. The fluid acceleration due to a directional pressure difference can be interpreted as the effect of an external body force in momentum equation, Eq. (2.6). A body force causes acceleration, $\boldsymbol{a}$, of a fluid element as

$$\boldsymbol{a} = \frac{\boldsymbol{f}_{body}}{\rho} \tag{3.1}$$

here, $\boldsymbol{f}_{body}$ is the body force per unit volume of the fluid element, so-called force density. The force applied on a fluid element with volume d∀ as a result of a pressure difference in x direction is $-\frac{dP}{dx}d\forall$, so the force per unit of the mass becomes $-\frac{1}{\rho}\frac{dP}{dx}$.

In this study, the plates are located at $y = 0$ and $y = d$. The fluid starts to move from rest until it reaches steady state. Under such conditions, the analytical solution for the time dependent velocity is given by (Morris et al., 1997)

$$V_x(y,t) =$$

$$\frac{f_x}{2\nu}y(y-d) + \sum_{n=0}^{\infty}\frac{4f_x d^2}{\nu\pi^3(2n+1)^3}\sin\left(\frac{\pi y}{d}(2n+1)\right)\exp\left(-\frac{(2n+1)^2\pi^2\nu}{d^2}t\right) \tag{3.2}$$

where, V_x is the flow velocity in the x direction, t stands for time and ν is kinematic viscosity. f_x is the force applied per unit of the fluid mass due to a pressure difference in x direction:

$$f_x = -\frac{1}{\rho}\frac{dP}{dx} = \frac{8\nu U_o}{d^2} \tag{3.3}$$

here, U_o is the predefined maximum steady state velocity which occurs at a location equidistant from the plates. The physical properties are selected as $d = 5 \times 10^{-3}$ (m), $\rho_o = 1000$ (kg/m^3) and $\nu = 1 \times 10^{-6}$ (m^2/s).

3.3.1. Viscous Term Formulation

Using this benchmark case first the ability of the two standard formulations to model the viscous term, Eq. (2.20) referred as *"Form I"* and Eq. (2.21) referred as *"Form II"*, is examined.

In this simulation, U_o is set to 0.1 (m/s) corresponding to a Reynolds number ($Re = U_o d/\nu$) equal to 500. The results for uniform particle spacing of $dx = dy \approx 1.08695 \times 10^{-4}$ (m) (45 layers of particle in span of the plates) are shown in Figs. 3.1(a, b). Using *"Form II"*, the results are more satisfactory, with a relative error of 0.47% for the peak of the velocity profile at steady state. This error was 7.2% using *"Form I"*.

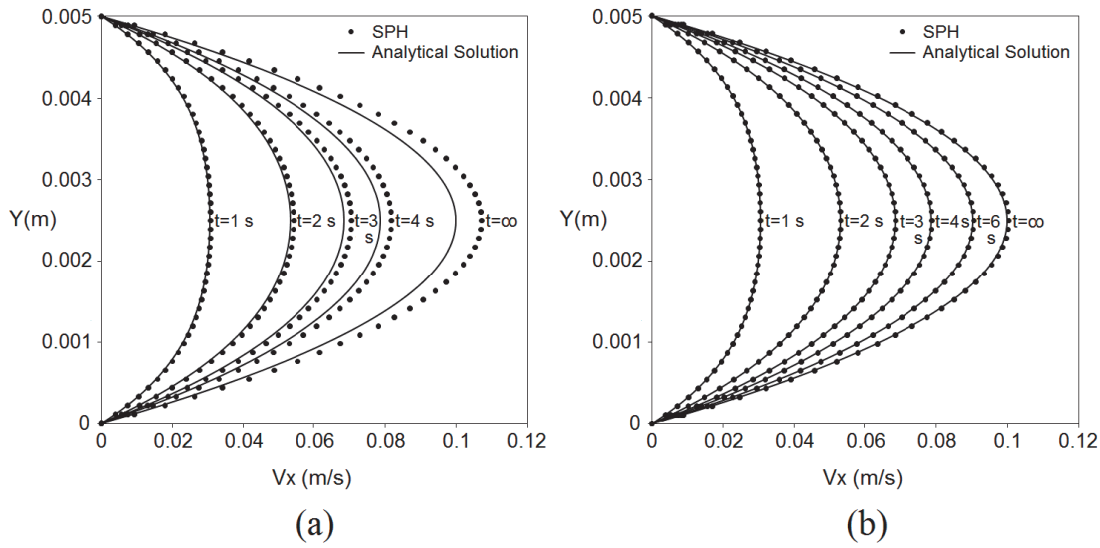

Fig. 3.1. Velocity profiles for Poiseuille flow at different start up instants to reach steady state; $Re = 500, \varepsilon = 0$. Using standard viscosity formulations in: (a) *"Form I"*; and (b) *"Form II"*.

The spatial convergence rate in both simulation cases is evaluated based on L_2 relative error norm as

$$L_2\ relative\ error\ norm = \sqrt{\frac{\sum_{i=1}^{i=N}(V_{x,SPH}(i)-V_{x,Exact}(i))^2}{\sum_{i=1}^{i=N}V_{x,Exact}^2(i)}} \tag{3.4}$$

where $V_{x,SPH}(i)$ and $V_{x,Exact}(i)$ are axial velocity of particle i simulated by SPH and calculated by exact analytical solution, respectively. N is the number of particles.

In Fig. 3.2, the average L_2 relative error norm of the velocity in Fig. 3.1 is plotted against the particle spacing.

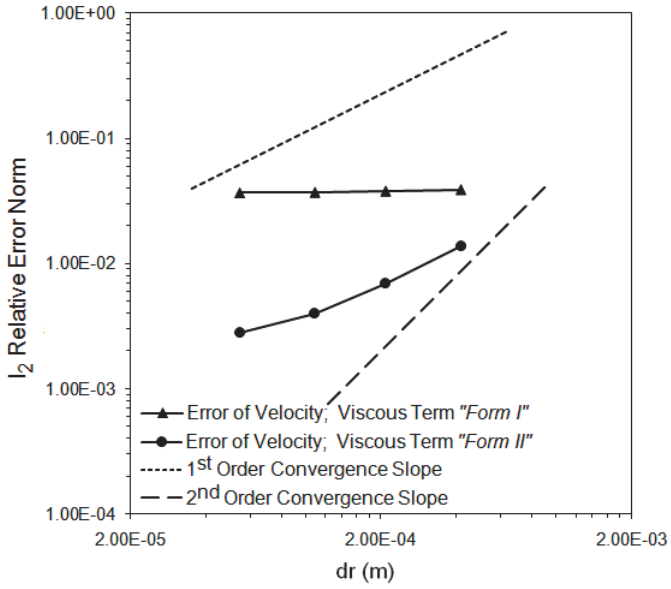

Fig. 3.2. Poiseuille flow with $Re = 500, \varepsilon = 0$; Average L_2-norm of relative error for axial velocity using standard viscosity formulations in *"Form I"* and *"Form II"*.

The convergence rate is very slow when *"Form I"* is used to model viscous effect. Also, the error norm converges to a higher value than when using *"Form II"*. The theoretical convergence rate of SPH discretization has been proved to be second order

(Ellero et al., 2002; Liu and Liu, 2003). However, several reasons affect the accuracy of SPH calculations (Quinlan and Basa, 2006; Vaughan et al., 2008). The most important ones are the movement of SPH particles with regards to their initial regular distribution and the ratio of smoothing length to particle spacing (Vacondio et al., 2011).

As it appears, increasing the number of particles did not have a significant impact on the accuracy of the results obtained using *"Form I"*. We found that the accuracy of this formulation is highly dependent on the selected type of kernel function and flow characteristics; however, this was not the case for *"Form II"*. It should be noted however that Cleary (1998) proposed and applied successfully a calibration coefficient for *"Form I"* based on a series of numerical tests performed on the case of time dependent Couette flow. The proposed coefficient still need, however, to be generalized for different kernel functions. This is also the case for a new suggested formulation for modeling viscous force in shear flows which possesses a dependent coefficient (Monaghan, 2006). The detailed investigation of these issues is beyond the scope of this study.

The test conditions for *"Form II"* are then extended to different Reynolds numbers ($Re = 0.05$ and $Re = 1500$). The results are shown on Fig. 3.3. For all cases, there is a very good agreement between the numerical simulations and the analytical solutions. For the case of $Re = 1500$, the maximum relative error for the peak of the velocity during the simulation is 0.49% and the average relative error over all the particles in the domain at steady state is 0.68%. A simulation test with a lower number of particles (21 particles located in the span of the plates) showed 0.9% relative error for the peak of the velocity at steady state.

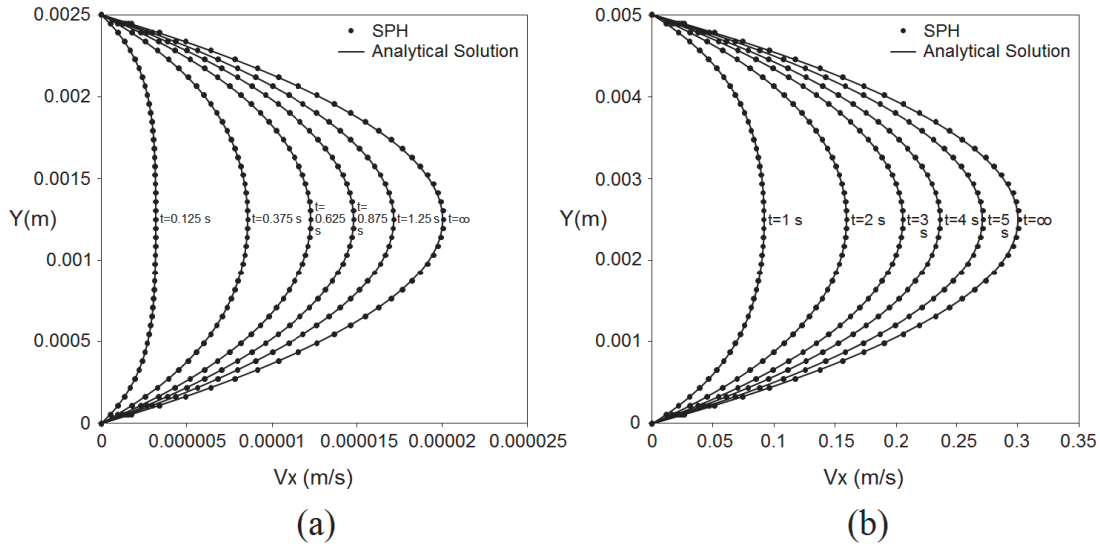

Fig. 3.3. Velocity profiles for Poiseuille flow at different start up instants to reach steady state: (a) $Re = 0.05$; and (b) $Re = 1500$.

It should be noted that the *"Form II"* for viscosity formulation was presented to simulate very low Reynolds number flows (Morris et al., 1997), however, it also shows a good validity for a wider range of Reynolds numbers for such unsteady flow configuration.

Figure 3.4 presents the evolution of the maximum flow velocity (at the centerline between the two plates) and the maximum changing in density of the particles with respect to the initial reference density. The density remained constant and did not show large fluctuations for both Reynolds number cases ($Re = 0.05$ and $Re = 1500$). The maximum relative variations in density are 0.000056% and 0.000126% during the simulation for $Re = 0.05$ and $Re = 1500$ respectively, which is perfectly within an acceptable range.

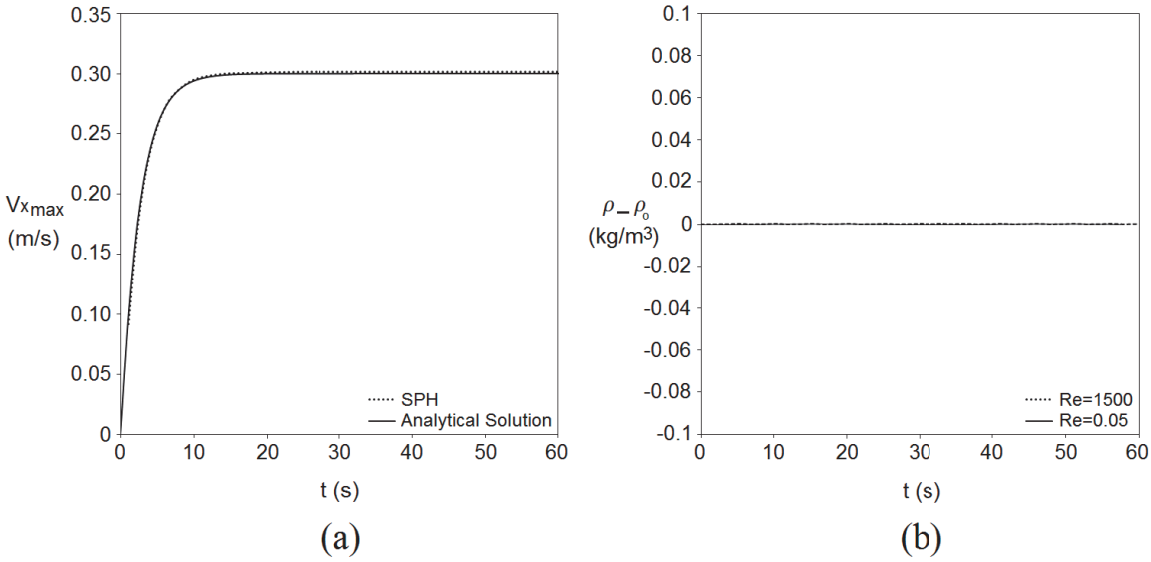

Fig. 3.4. The Poiseuille flow characteristics: (a) maximum flow velocity with respect to time for $Re = 1500$ case; and (b) maximum particle density changes versus time for $Re = 1500$ and $Re = 0.05$ cases.

3.3.2. XSPH Variant

The second test using this benchmark case is to investigate the effect of applying XSPH variant to particle movements (Eq. 2.29). This variant was proposed with the goal of preventing particles from penetrating each other when simulating impinging streams of fluid (Monaghan, 1989). It has also been reported to be capable of keeping the particles orderly during simulations of nearly incompressible fluids in the absence of viscosity (Monaghan, 1992). This variant has been employed in literature for different simulation cases, without a prior validation. Figure 3.5 shows the effect of XSPH variant ($\varepsilon = 0.3$) on particle order, beyond steady state, compared to the classical formulation for particle movement (Eq. 2.28). Particles are initially positioned with spacing of 2.08333×10^{-4} (m). In this case, the fluid properties are the same as mentioned before and

Reynolds number is equal to 500. In addition, the standard viscosity formulation in *"Form II"* is employed. In present simulation, the XSPH variant creates disorder in particle movements especially in the regions subjected to high velocity gradients.

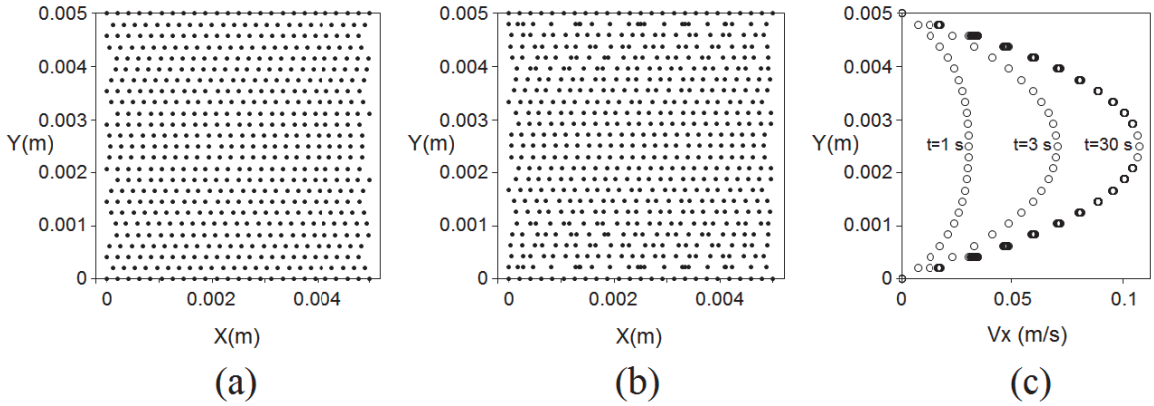

Fig. 3.5. Investigation on the effect of applying the XSPH variant to particle order and velocity field in the domain for Poiseuille flow with $Re = 500$: (a) particle distribution beyond steady state for $\varepsilon = 0$; (b) particle distribution beyond steady state for $\varepsilon = 0.3$; and (c) velocity profiles for $\varepsilon = 0.3$.

Oscillation in interparticle spacing along the axis of the plates and L_2 relative error norm of velocity for the first layer of the particles near the plates are demonstrated in Fig. 3.6 at steady state with respect to initial particle spacing. The rate of spatial convergence is close to the first order.

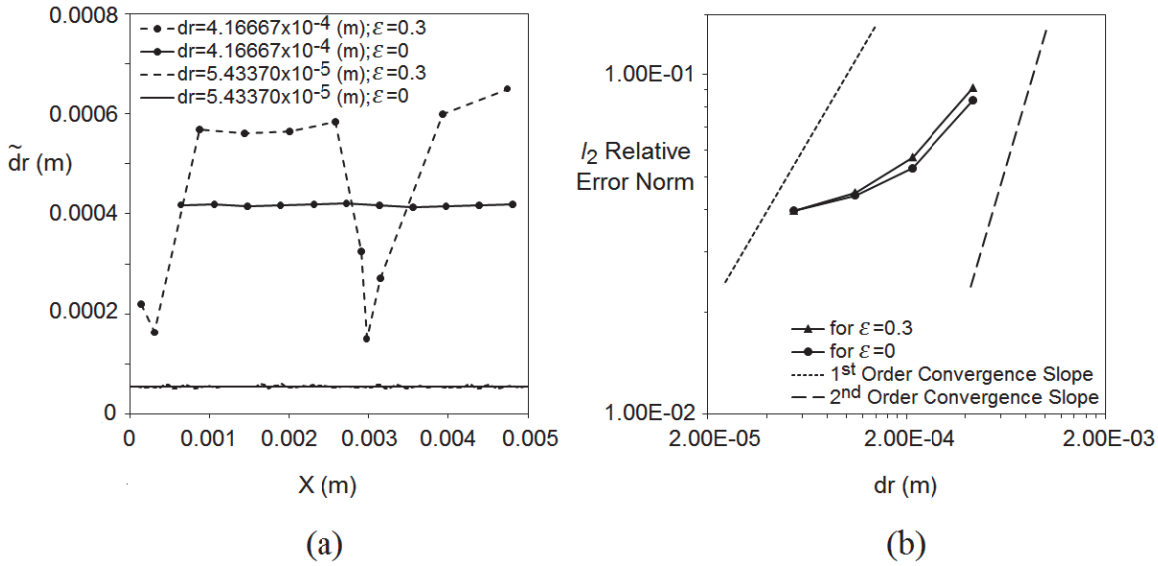

Fig. 3.6. Investigation on the effect of applying XSPH variant on the closest layer of particles to the plates in the steady state; Poiseuille flow with $Re = 500$: (a) oscillation in interparticle spacing; and (b) average L_2-norm of relative error of axial velocity.

As it shows however, that the undesirable effect of XSPH variant can be minimized by increasing the number of particles, but this will lead to higher computational time. In comparison, not using the XSPH variant leaded to accurate results and more ordered particle distribution.

The effect of different numerical parameters such as precision of calculations, time step, smoothing length and sound speed were also examined and the consequence was just delaying or speeding up the onset of disordered particle distribution. Based on this study, XSPH should be used with caution in the presence of real viscosity, especially when the flow is subjected to high velocity gradients and particle resolution is not high. These results regarding the XPSH variant are consistent with the observation of Imaeda and Inutsuka (2002) on the effect of this variant on shear flows in astrophysical systems.

3.3.3. Pressure Gradient Term Formulation

In this chapter, the standard symmetric formulation for pressure gradient (Eq. 2.11) is always employed as it conserves exactly the linear and angular momentum (the calculated pressure force on particle a due to its neighboring particle, b, is equal to the applied force on particle b caused by particle a).

At this point it should be mentioned that in experimental fluid mechanics, the thermodynamic pressure of a moving fluid is measured by a static pressure probe. By definition, "the static pressure is the pressure seen by the fluid particle as it moves (so it is something of a misnomer!)" (Fox et al., 2004). This definition is consistent with the Lagrangian motion of particles in SPH. However, in most of the SPH literature, P in Navier-Stokes equations is referred to as "hydrostatic pressure" and in some works it is called the total pressure and expressed as the summation of dynamic and hydrostatic pressures in which the equation of state is used to model dynamic pressure (Morris et al., 1997; Sigalotti et al., 2003; Ma and Ge, 2008). It is then important to clarify that the pressure obtained through SPH simulations represents static pressure.

Ma and Ge in 2008 examined the computational performance of standard symmetric formulations for the pressure gradient term compared to asymmetric ones. They reported that the symmetric formulation is less accurate, more sensitive to the selected value for sound speed and leads to larger errors. Their conclusion was based on simulation results with large fluctuations in flow variables. In the case of Poiseuille flow, they reported a noisy mean flow velocity and pressure term for values of $c^2 = 10^{-7}, 2 \times 10^{-5}, 5 \times 10^{-5}$ $(\mathrm{m}^2/\mathrm{s}^2)$. These values correspond to sound speeds of 25, 358, and 566 times of the peak velocity magnitude at steady state (1.25×10^{-5} $(\mathrm{m/s})$ for $Re = 1.25 \times 10^{-2}$),

respectively. The error in their simulations was about 3% at the peak of the velocity profile at steady state for both symmetric and asymmetric pressure formulations. In the present simulation (Fig. 3.3b), this error was 0.49% for Re=1500 using the same formulation for modeling the viscous term.

The time step (10^{-4} s) reported in the Ma and Ge study cannot be appropriate for simulations with very high sound speeds due to CFL stability conditions (Morris et al., 1997). The large fluctuations in the calculated pressure terms and mean velocity, which can also affect the order of particle arrangement in both symmetric and asymmetric forms, are not due to the computational performance of the SPH formulation employed for pressure gradient term but are instead due to the mismatch between the adopted values for sound speed and computational time step.

Figure 3.7 shows the mean flow velocity calculated in this thesis, using the standard symmetric formulation for pressure gradient and considering all moving particles in the domain. The geometry and flow characteristics are selected as in the work of Ma and Ge (2008): $d = 1 \times 10^{-3}\ (\mathrm{m}),\ \rho_o = 1000\ (\mathrm{kg/m^3}),\ \nu = 1 \times 10^{-6}\ (\mathrm{m^2/s}),\ Re = 1.25 \times 10^{-2}$, 50 particles in span of the plates and the worst value for sound speed, 566 times greater than the peak velocity magnitude ($c^2 = 5 \times 10^{-5}\ \mathrm{m^2/s^2}$). The results do not show large fluctuations as it was reported by Ma and Ge (2008).

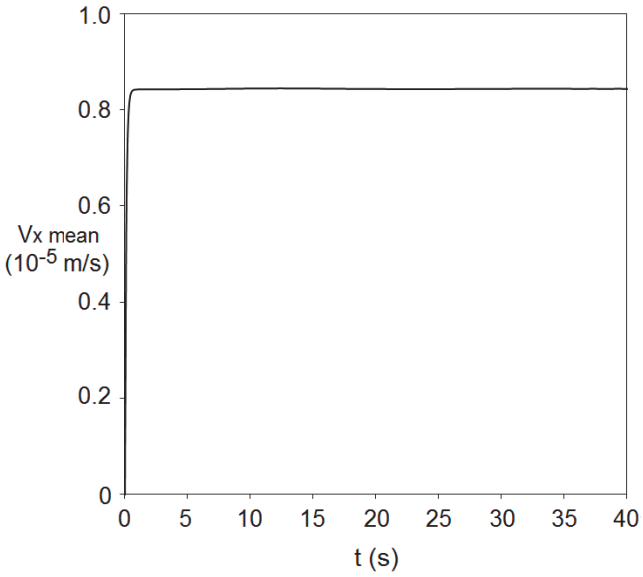

Fig. 3.7. Time variation of mean flow velocity for Poiseuille flow at $Re = 1.25 \times 10^{-2}$ using $c^2 = 5 \times 10^{-5}$ $(\mathrm{m}^2/\mathrm{s}^2)$ corresponding to $c = 566 \times U_o$.

In the following sections, the flexibility of SPH as a meshfree particle method to handle simulation of oscillating flows is examined. Here, two cases: internal flow driven by an oscillating pressure difference and flow above an oscillating plate are studied. As the performance of the viscosity formulation in *"Form II"* was verified in simulation of Poiseuille flow for a variety of Reynolds numbers, this form is employed here and its performance is examined in simulating cases where there is no simple relationship between the viscous and applied body forces. In addition, the XSPH variant is not considered since as shown before, this variant is not adequate for this type of shear flow with elevated velocity gradients.

3.4. Oscillating Flow Cases

3.4.1. Internal Flow Driven by Oscillating Pressure Difference

This case is similar to Poiseuille flow except that the pressure difference does not remain constant but instead varies with time. This type of flow is commonly found in large arteries and in industrial piping systems due to changes in direction of pressure waves. The flow between two plates oscillates due to an axial oscillating pressure difference of

$$\frac{dP}{dx} = -A\,cos(\omega t) \tag{3.5}$$

where, A is the amplitude of the imposed pressure difference, ω is the oscillation frequency ($\omega = 2\pi/T$, T is the period of oscillation) and t stands for time. The analytical solution for velocity in this case is found as (Loudon and Tordesillas, 1998)

$$V_x(y,t) = \frac{A}{\omega\rho\gamma}\ \{[\sinh\Phi_1(y)\,.\sin\Phi_2(y) + \sinh\Phi_2(y)\,.\sin\Phi_1(y)]\cos(\omega t) +$$

$$[\gamma - \cosh\Phi_1(y)\,.\cos\Phi_2(y) - \cosh\Phi_2(y)\,.\cos\Phi_1(y)]\sin(\omega t)\} \tag{3.6}$$

where,

$$\Phi_1(y) = \frac{W_o}{\sqrt{2}}\left(1 + \frac{2y}{d}\right),\quad \Phi_2(y) = \frac{W_o}{\sqrt{2}}\left(1 - \frac{2y}{d}\right) \tag{3.7}$$

and

$$\gamma = \cosh(\sqrt{2}W_o) + \cos(\sqrt{2}W_o) \tag{3.8}$$

The variables d and W_o are the distance between the plates and Womersley number, respectively. Womersley number is an important dimensionless number in oscillating

internal flows that represents the ratio of oscillating inertial effects to viscous effects and is defined as

$$W_o = \frac{d}{2}\sqrt{\frac{\omega}{\nu}} \tag{3.9}$$

Figures 3.8(a, b) show the simulation results for a Womersley number of $W_o = 1$ and oscillating pressure difference amplitudes of $0.09\ (\mathrm{N/m^3})$ and $90\ (\mathrm{N/m^3})$. The fluid physical properties are selected similar to the previous cases. The particle initial spacing is 1.086956×10^{-4} (m) and smoothing length is selected 1.25 times of the initial particle spacing. The relative error in calculated velocities at the centerline between the plates has an average value of 0.31% and a maximum value of 0.69% during computation.

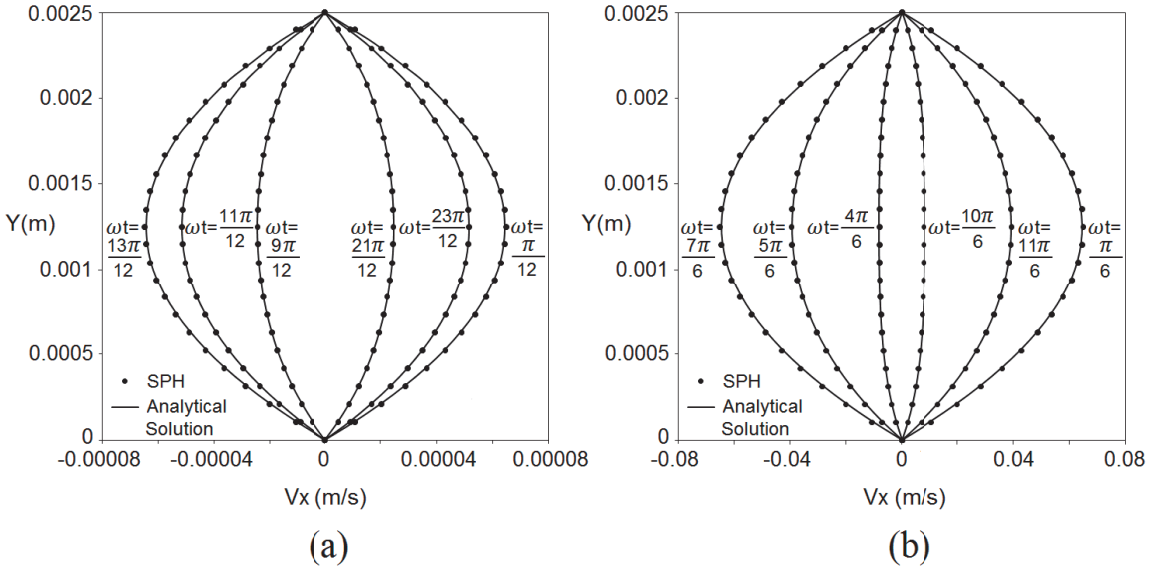

Fig. 3.8. Velocity profiles for oscillating flow between two parallel plates over a period; $W_o = 1$: (a) $A = 0.09\ (\mathrm{N/m^3})$; and (b) $A = 90\ (\mathrm{N/m^3})$.

For a Womersley number equal to 1, viscous forces dominate oscillating inertial forces and the velocity field shows Poiseuille type profiles. The highest velocity occurs at the centerline between the two plates.

The simulation results for a larger Womersley number of $W_o = 10$ and oscillating pressure difference amplitudes of 0.3 $(\mathrm{N/m^3})$ and 3000 $(\mathrm{N/m^3})$ are shown in Figs. 3.9(a, b). The particle initial spacing is 1.08695×10^{-4} (m) and the same physical properties as before are employed for the fluid. The relative error in calculated velocity at the centerline has an average value of 0.31% and a maximum value of about 0.7%. For Womersley number equal to 10, the inertial forces are stronger than viscous forces and the velocity profiles become flat in the central region and the highest velocity occurs in the regions within the vicinity of the plate.

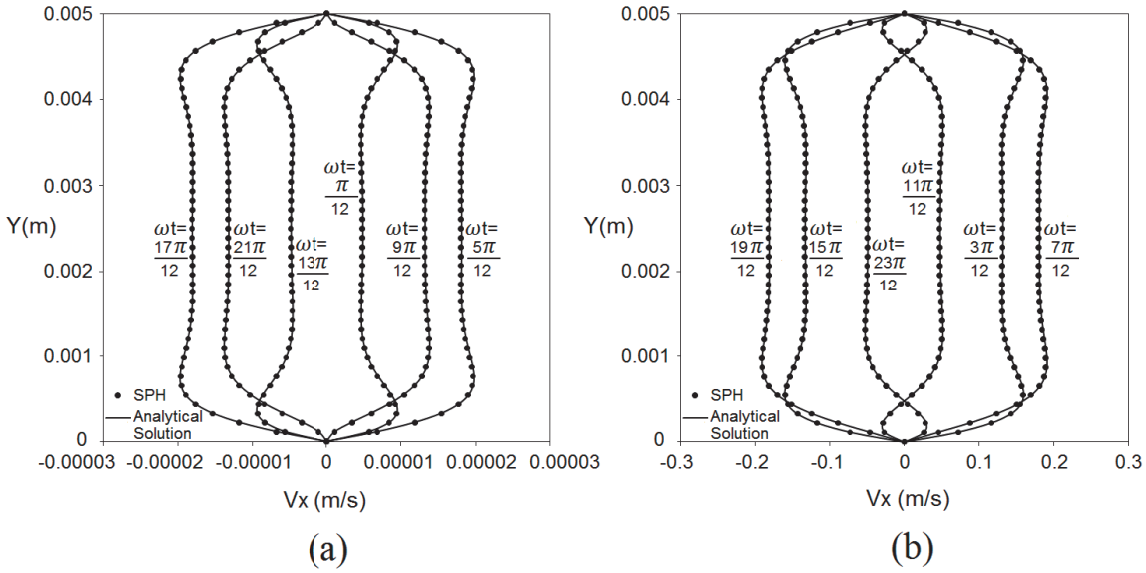

Fig. 3.9. Velocity profiles for oscillating flow between two plates over a period; $W_o = 10$: (a) $A = 0.3$ $(\mathrm{N/m^3})$; and (b) $A = 3000$ $(\mathrm{N/m^3})$.

The spatial convergence is analyzed using L_2 relative error norm criteria and depicted in Fig. 3.10. The results show a rate of convergence which is between first and second order.

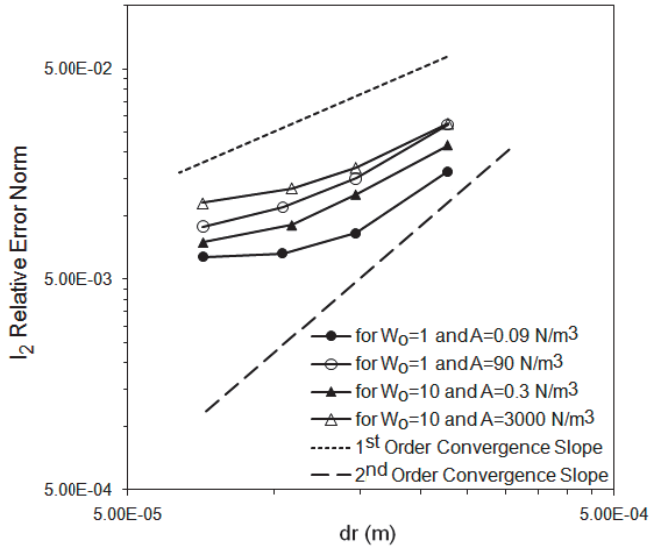

Fig. 3.10. Oscillating flow between parallel plates: Average L_2-norm of relative error for axial velocity over a period.

The maximum variation in particle density occurred during cases with a high Womersley number and a higher amplitude of imposed pressure difference. The maximum relative variation in density for the cases with $W_o = 1$ is 0.0029%, occurs when $A = 90\ (\mathrm{N/m^3})$, and for the cases with $W_o = 10$ is 0.034%, occurs when $A = 3000\ (\mathrm{N/m^3})$. These values are perfectly within the acceptable range.

In these simulations, at high Womersley numbers, the simulations using viscous formulation in "*Form I*", which was less accurate for Poiseuille flow, gives a good agreement with the analytical solution in the central region. This is, however, not surprising since, as shown in Fig. 3.9, the velocity gradient is almost zero in this region.

Another important characteristic to investigate for such oscillatory flows is the phase shift between the applied pressure difference and the resulting velocity. Figures 3.11 (a, b) show the applied oscillating pressure difference and the resulting oscillating velocity at the centerline between the plates.

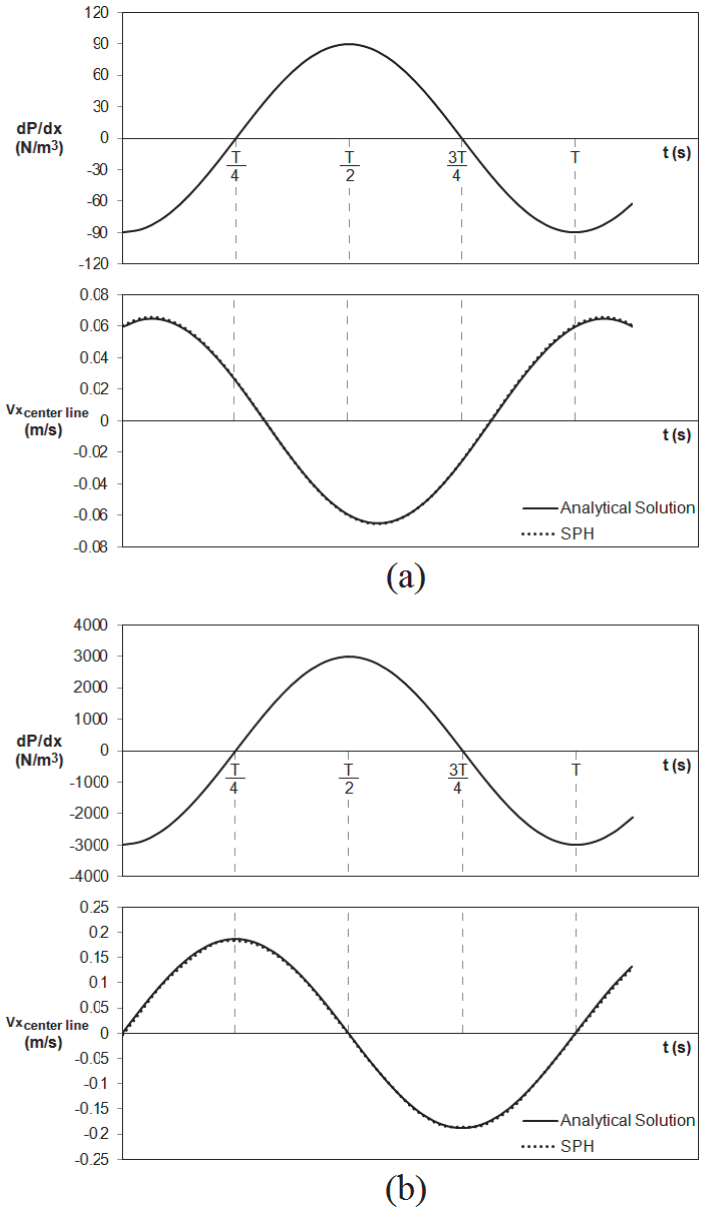

Fig. 3.11. Applied oscillating pressure difference and derived flow velocity at the center line between two plates: (a) $W_o = 1$ and $A = 90$ $(\mathrm{N/m^3})$; and (b) $W_o = 10$ and $A = 3000$ $(\mathrm{N/m^3})$.

SPH particles show the capability to accurately follow rapid changes in the acceleration and deceleration phases. The simulations then accurately reproduce the phase shift between the applied pressure difference and the velocity. At instants when the driving pressure difference becomes zero, SPH particles still move properly dependent upon their acquired energy from previous instants.

In practice, the total volume flow rate is a more important parameter than velocity, because it determines the time that fluid resides in the region of interest. It also can be a valuable indicator to examine the accuracy of the SPH incompressibility assumption and velocity calculations with respect to particle resolution. When using particle methods, the volume flow rate can be approximated by a summation over the particles located in a strip across the flow cross section with the width of particle spacing. In the present simulation, this gives

$$Q(t) = \sum_{j=0}^{j=m} V_{x,j}(y,t)dy \tag{3.10}$$

where m indicates the number of particle layers extended across two plates and dy is the width of the stream channel that a particle flows through (particle spacing).

The time variation of the calculated volume flow rate is compared with the exact solution in Fig. 3.12 for a case with $W_o = 10$ and $A = 3000\ (\mathrm{N/m^3})$. The results are in a very good agreement with an average relative error of 0.6% over one period.

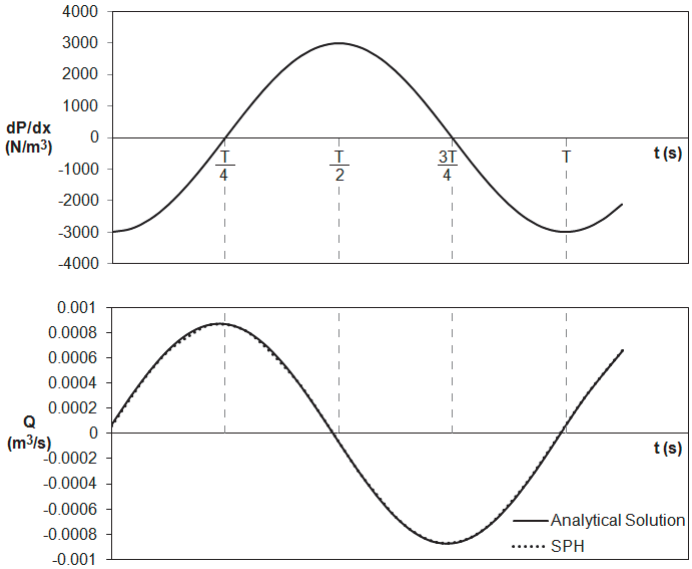

Fig. 3.12. Applied oscillating pressure difference and resulting oscillating volume flow rate through two plates; $W_o = 10$ and $A = 3000\ (\mathrm{N/m^3})$.

3.4.2. Flow above an Oscillating Plate

In literature, this problem is referred to as Stokes's second problem. A stationary fluid above a plate starts to move due to oscillation of a plate. The numerical simulation of this problem is of great interest and there is a wide practical application, such as the study of the mechanical behavior of blood cells under oscillating shear stress (microscale), controlling the coating thickness in oscillating film flows and the investigation of the hydrodynamic loads produced by structural vibration which is an important design factor in mechanical systems (macroscale).

This case is characterized by a varying phase lag between the velocities of different layers of particles above the plate. The plate moves in x direction with a velocity of $U_o(t) = U_{o,m}\cos\omega t$, where $U_{o,m}$ is the amplitude of the velocity oscillation and ω is the

oscillation or angular frequency ($\omega = 2\pi/T$, T is the period of oscillation). The analytical solution for this problem is obtained as (White, 1991)

$$V_x(y,t) = U_{o,m}\exp(-\eta)\cos(\omega t - \eta) \quad , \qquad \eta = y\sqrt{\frac{\omega}{2\nu}} \tag{3.11}$$

The flow oscillating velocity is damped as y increases ($\eta \to \infty$ leads to $V_x \to 0$).

The instantaneous velocity profiles over one period for the plate velocity amplitude of $2 \times 10^{-5}\,(\mathrm{m/s})$ and $0.3\,(\mathrm{m/s})$ with oscillation frequency of $\omega = \pi\,(\mathrm{rad/s})$ and $10\pi\,(\mathrm{rad/s})$ are shown in Figs. 3.13 and 3.14. The fluid physical properties are selected similar to previous cases. Particles are initially spaced $1 \times 10^{-4}\,(m)$ and $5 \times 10^{-5}\,(\mathrm{m})$ apart for $\omega = \pi\,(\mathrm{rad/s})$ and $10\pi\,(\mathrm{rad/s})$ cases, respectively.

The maximum relative variation in density is 0.078% occurring when $\omega = \pi\,(\mathrm{rad/s})$ for cases with a velocity amplitude of $2 \times 10^{-5}\,(\mathrm{m/s})$. For cases with velocity amplitude of $0.3\,(\mathrm{m/s})$ the maximum variation in density is 0.000047%, also occurring when $\omega = \pi\,(\mathrm{rad/s})$. These results are perfectly within the acceptable range. The maximum density variation occurred for cases with low oscillation frequency.

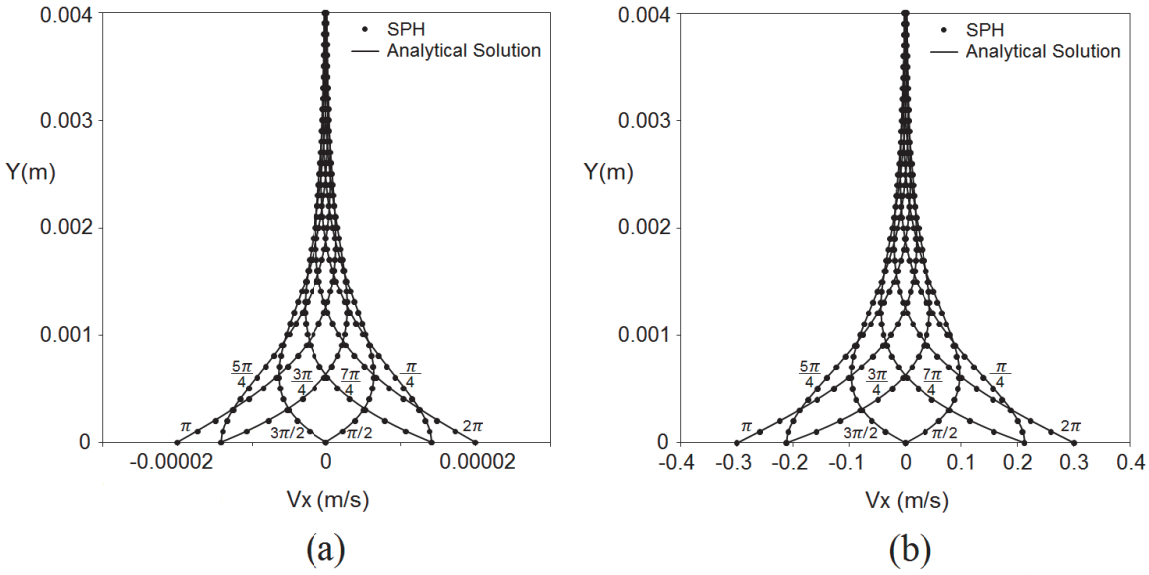

Fig. 3.13. Velocity profiles for flow over an oscillating plate with angular frequency of $\omega = \pi$ (rad/s)(T = 2 s) at increments of $\omega t = \pi/4$ over one period for plate velocity amplitude of: (a) $U_{o,m} = 2 \times 10^{-5}$ (m/s); and (b) $U_{o,m} = 0.3$ (m/s).

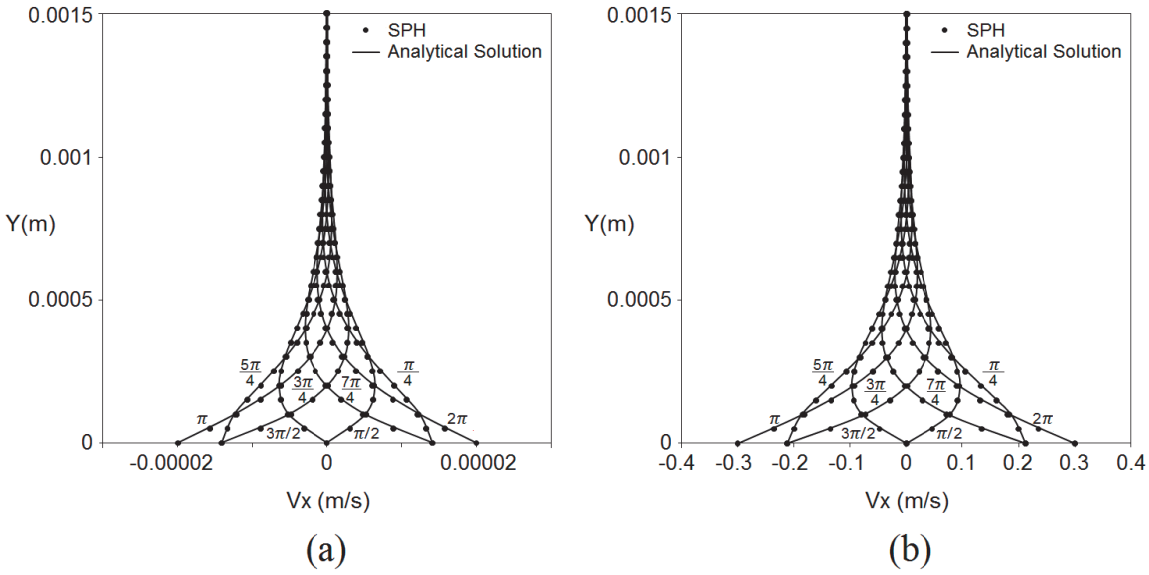

Fig. 3.14. Velocity profiles for flow over an oscillating plate with angular frequency of $\omega = 10\pi$ (rad/s)(T = 0.2 s) at increments of $\omega t = \pi/4$ over one period for plate velocity amplitude of: (a) $U_{o,m} = 2 \times 10^{-5}$ (m/s); and (b) $U_{o,m} = 0.3$ (m/s).

SPH shows the capability to capture the oscillating boundary layer region. This case has the most complex oscillating flow features since different layers of fluid experience different phase lags with regard to plate oscillations. SPH particles are able to follow these oscillations and there is a good agreement with the analytical solution. The particles far from the plate remained at rest as predicted by the analytical solution even for high magnitude and frequency of the oscillations.

The highest error in velocity calculations for the layer of particles near to the oscillating plate (subjected to the most elevated velocity gradient) occurs at $t = T/4$ and $t = 3T/4$. These instants correspond to a change in direction of the oscillating plate. For higher oscillation frequency cases (Fig. 3.14), the average relative error in velocity calculations for the layer of particles near to the plate is 1.54% (excluding $t = T/4$ and $3T/4$) and the largest error is 5.5% (at $t = T/4$ and $t = 3T/4$), however, for lower oscillation frequency cases (Fig. 3.13), the average error is 0.97% and the largest one is 4.9%. Although the cases with higher oscillation frequency (Fig. 3.14) has a particle spacing two times smaller than that of the case with lower frequency (Fig. 3.13), there is a higher average relative error in comparison with the theoretical solution.

The convergence rate in L_2 relative error norm is shown in Fig. 3.15, which is close to first order. Interestingly, the cases with the same oscillation frequency show quite similar spatial convergence behavior. The average relative error in velocity calculations is larger in higher oscillation frequencies compared with the lower frequencies.

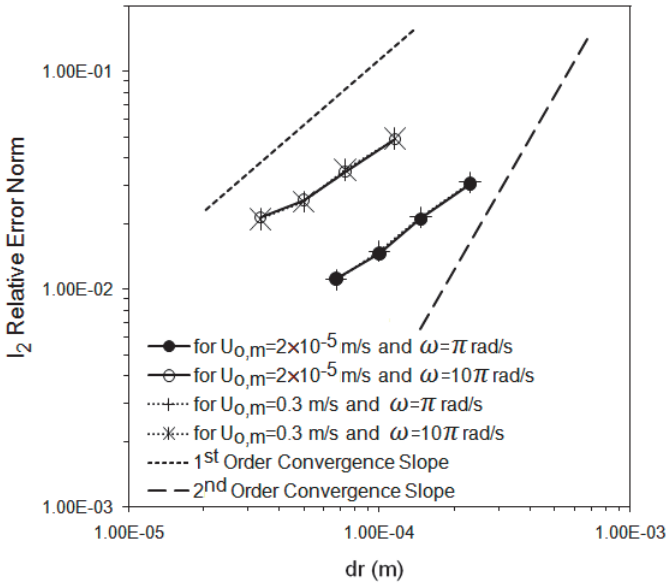

Fig. 3.15. Flow over an oscillating plate: Average L_2-norm of relative error for axial velocity over a period.

In fact, a higher oscillation frequency limits the wave propagation and results in a thinner oscillating boundary layer subject to a higher velocity gradient. The high oscillation frequency cases need high particle resolution which should be selected with respect to the thickness of the oscillating layer.

A good estimate for the particle resolution in the oscillating layer can be obtained knowing that the thickness of this layer is approximated where $V_x = 0.01 \times U_{o,m}$, (White, 1991) as

$$\delta \approx 6.5\sqrt{\frac{\nu}{\omega}} \tag{3.12}$$

To minimize the error in velocity calculations, it is of use to determine the optimal number of particle layers in the oscillating layer. Figure 3.16 shows the variation of the

relative error in the velocity calculations for the layer of particles near to the oscillating plate as a function of number of particle layers, N_δ, in the oscillating layer.

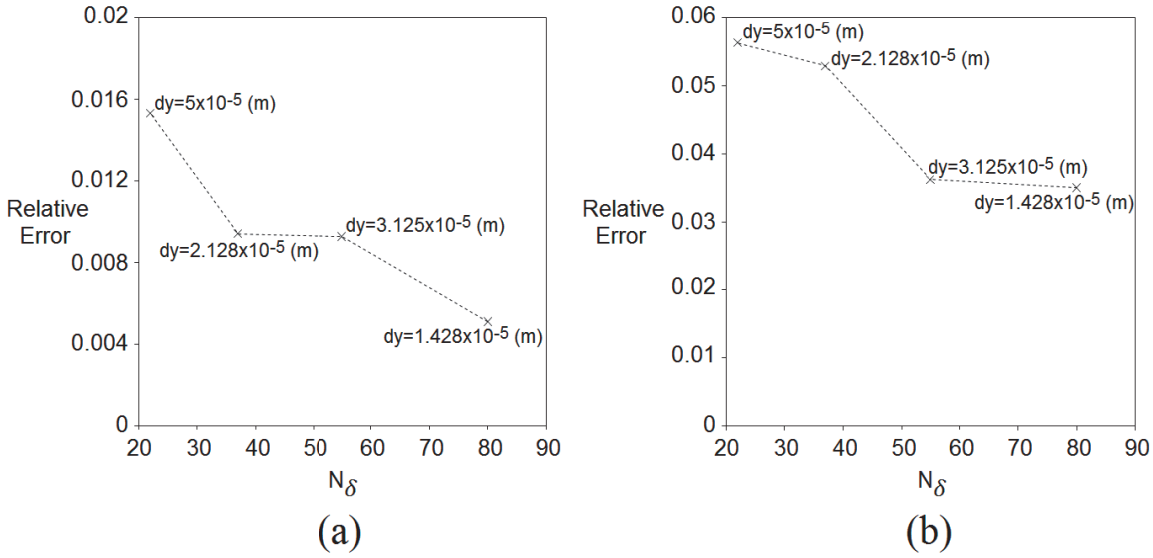

Fig. 3.16. Average relative error in the velocity calculations for the adjacent layer of particles to the oscillating plate; $U_{o,m} = 0.3$ (m/s) and $\omega = 10\pi$ $\left(\frac{\text{rad}}{\text{s}}\right)$ (T = 0.2 s): (a) at all instants excluding $t = T/4$ and $3T/4$; and (b) at $t = T/4$ and $3T/4$ instants.

To reduce the average relative error to about 1%, the optimal number of particles across the oscillating layer thickness should be 40 to 50. This approach will limit the relative error to about 4.5% in the layer adjacent to the oscillating plate at the most critical instants ($t = T/4$ and $3T/4$) while maintaining a reasonable computational time. Consequently, for simulation of such oscillating shear flows it is suggested to consider the thickness of the oscillating layer as the length scale of the flow. This means that using the same particle spacing for simulations with different frequencies is not recommended.

A good initial value for particle spacing can be obtained by dividing the estimated oscillating layer thickness (Eq. 3.12) by 40.

3.4.3. Oscillating Wall Shear Stress

An important parameter to take into account for oscillating flows is the wall shear stress. Wall shear stress plays a significant role in natural and industrial phenomena including cholesterol deposition in arteries (Irace et al., 2003), erosion in mechanical systems (Yamaguchi et al., 2005) and membrane based filtration processes (Gésan-Guiziou et al., 1999).

In laminar Newtonian flows, the wall shear stress, τ_w, is proportional to the local tangential velocity gradient with respect to normal distance from the wall boundaries, irrespective of wall shape. This is expressed in Eq. (3.13) as

$$\tau_w = -\mu \left(\frac{dV_t}{dx_n} \right)_w \tag{3.13}$$

where x_n is the local coordinate normal to the wall and V_t is the tangential local velocity with respect to the wall.

For flat wall boundaries, this expression can simply be determined using a finite difference scheme, which requires knowing the velocity of one or two layers of particles adjacent to the wall. However, in meshfree particle methods, this scheme is limited and inappropriate. In this section the possibility of developing a general formulation for the calculation of wall shear stress is examined.

There are several possible ways in SPH to approximate the gradient of a quantity. Using the summation approximation of Eq. (2.2), the gradient of the tangential velocity

with respect to the normal coordinate of the wall can be derived. Then, the wall shear stress becomes

$$\tau_w = -\mu \left(\frac{dV_t}{dx_n}\right)_{a \in wall} = -\mu \sum_b m_b \frac{V_{t,b}}{\rho_b} \frac{\partial W(\boldsymbol{r}_a - \boldsymbol{r}_b, h)}{\partial x_n} \tag{3.14}$$

here,

$$\frac{\partial W(\boldsymbol{r}_a - \boldsymbol{r}_b, h)}{\partial x_n} = \frac{(x_{n,a} - x_{n,b})}{|\boldsymbol{r}_a - \boldsymbol{r}_b|} \frac{dW}{dr} \tag{3.15}$$

Based on the general expression of (Monaghan, 1992)

$$\rho \nabla A = \nabla(\rho \mathrm{A}) - \mathrm{A} \nabla \rho \tag{3.16}$$

and using the SPH standard approximation of Eq. (2.2), the wall shear stress reads

$$\tau_w = -\mu \left(\frac{dV_t}{dx_n}\right)_{a \in wall} = -\frac{\mu}{\rho_a} \sum_b m_b \left(V_{t,b} - V_{t,a}\right) \frac{\partial W(\boldsymbol{r}_a - \boldsymbol{r}_b, h)}{\partial x_n} \tag{3.17}$$

For oscillatory flows, analyzing instantaneous variations, rather than average values, of wall shear stress is of primary importance. It is difficult to allocate the appropriate velocity to the imaginary particles, so as to resemble the exact velocity slope at the position of the wall particle. It should be mentioned that based on Eq. (2.36), the allocated artificial velocity of the imaginary particles, during computation, does not reflect the accurate velocity slope of the fluid particles near the plate. Therefore, this constraint should be taken into account when proposing a general formulation. Moreover, some SPH implementations do not use imaginary particles for simulation of wall boundaries. Consequently, only a limited number of particles will contribute to the summation in Eqs. (3.14) and (3.17) (kernel is truncated).

One can employ a methodology based on the kernel function modification (Bonet and Lok, 1999). However, this can be computationally expensive and it is preferable to implement an approach based on a general correction coefficient.

The proposed approach in this thesis displays its strength when computing the wall shear stress on the surface of thin structural bodies immersed in a fluid. The neighboring domain of a particle on the surface consists of particles on other sides of the body, however only the fluid particles on the same side of the surface should contribute to the summation of the particle's properties. In this study, imaginary and wall particles are not used to calculate the summation of wall shear stress, even though the wall particles are solved at each time step and their density is updated

Equations (3.14) and (3.17) can be modified by multiplying their right hand side by a correction coefficient, C_ξ, without any modification to the kernel function, resulting in

$$\tau_w = -\mu \left(\frac{dV_t}{dx_n}\right)_{a \in wall} = -\mu \sum_b m_b \, C_\xi \, \frac{V_{t,b}}{\rho_b} \frac{\partial W(\boldsymbol{r}_a - \boldsymbol{r}_b, h)}{\partial x_n} \tag{3.18}$$

and

$$\tau_w = -\mu \left(\frac{dV_t}{dx_n}\right)_{a \in wall} = -\frac{\mu}{\rho_a} \sum_b m_b \, C_\xi (V_{t,b} - V_{t,a}) \frac{\partial W(\boldsymbol{r}_a - \boldsymbol{r}_b, h)}{\partial x_n} \tag{3.19}$$

By employing a quartic spline kernel (influence domain of $2.5 \times h$) with h equal to 1.25 times the initial particle spacing, each fluid particle would have nearly 29 particles in its neighboring domain. However, to calculate wall shear stress, a particle on the wall will only have about 11 particles in its neighboring domain (see Fig. 3.17). Therefore, a correction coefficient of $C_\xi = \frac{29}{11} \approx 2.63$ is proposed to compensate for the kernel truncation on the wall boundary.

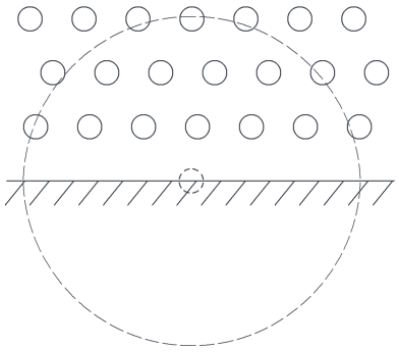

Fig. 3.17. A particle on the wall has 11 particles in its neighbouring domain (excluding other wall particles) instead of 29; for a kernel with the influence domain of $2.5 \times h$ and h equals to 1.25 times the particle spacing.

Employing different kernel functions and smoothing lengths will result in different numbers of particles in the neighboring domain of each particle. However, the correction coefficient will remain approximately the same. Using a kernel function with an influence domain of $2.5 \times h$ (quartic spline kernel) but having a smoothing length of $h = 1$ and 1.5 results in a correction coefficient of $C_\xi = \frac{21}{8} \approx 2.62$ and $C_\xi = \frac{44}{18} \approx 2.44$, respectively. Changing the kernel function to one with an influence domain of $3 \times h$ with $h = 1$ and 1.5 results in a correction coefficient of $C_\xi = \frac{26}{10} \approx 2.6$ and $C_\xi = \frac{65}{27} \approx 2.4$ respectively. Therefore, to generalize the correction coefficient, the approximated value of 2.5 can be used for all cases.

Figure 3.18 shows the wall shear stress variation on the lower plate for flow driven by an oscillating pressure difference (see Sec. 4.1) using general Eqs. (3.14) and (3.17) and modified Eqs. (3.18) and (3.19) with the same particle resolution ($dy = 3.20513 \times 10^{-5}$ m). The results are compared with the analytical solution and show the capability of each equation to reach the accurate analytical prediction.

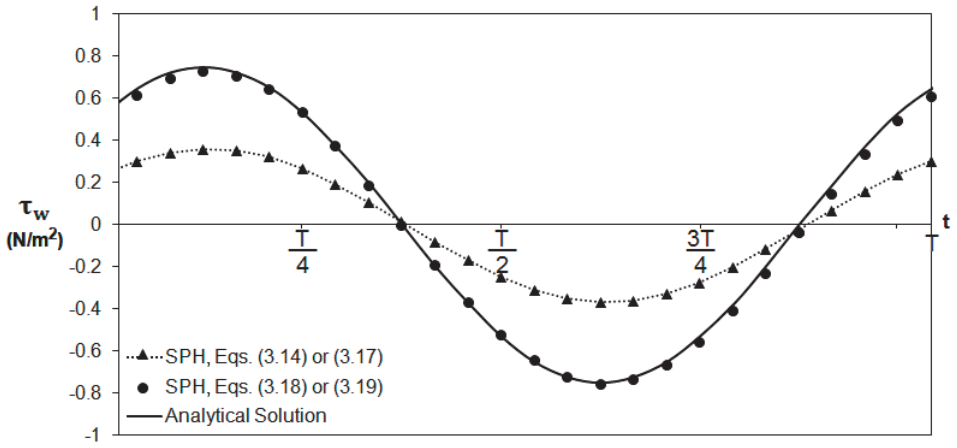

Fig. 3.18. Wall shear stress profiles for oscillating flow between two parallel plates using different formulations and comparison with analytical solution; $W_o = 10$ and $A = 3000$ $(\frac{\mathrm{N}}{\mathrm{m}^3})$.

In the above simulation, the wall boundary is stationary ($V_{t,a} = 0$) and both Eqs. (3.18) and (3.19) give the same value for wall shear stress. The performance of these formulations can therefore be examined more precisely in problems dealing with flow in interaction with moving wall boundaries.

The spatial convergence of different formulations for calculating wall shear stress is depicted in Fig. 3.19 using L_2-norm of relative error. The error norm converges to a high value when Eqs. (3.14) and (3.17) are used. The error norm of wall shear stress converges with a rate between first and second order for Eqs. (3.18) and (3.19).

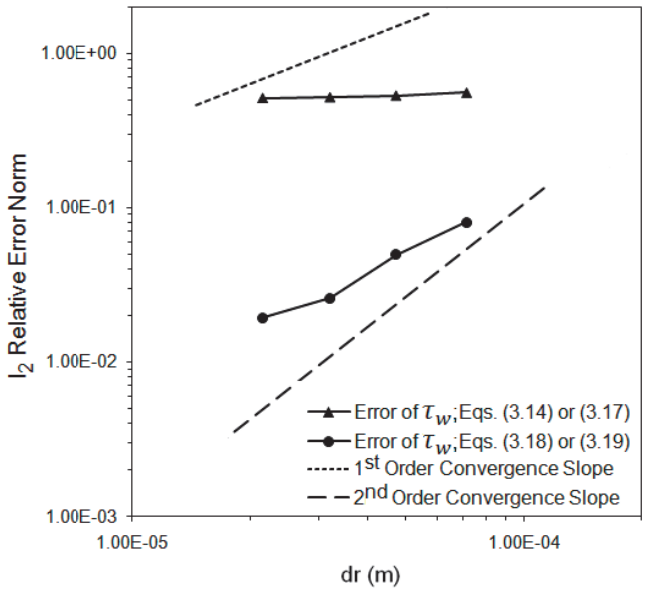

Fig. 3.19. L_2-norm of relative error for wall shear stress calculations over a period. Oscillating flow between two parallel plates; $W_o = 10$ and $A = 3000$ $(\frac{\mathrm{N}}{\mathrm{m}^3})$.

Using the same particle resolution to plot velocity profiles in Fig. 3.9(b), 1.08695×10^{-4} (m), does not give accurate results for the calculation of wall shear stress. Indeed, it is a common problem in mesh-based and meshfree computational methods to accurately compute the gradients of physical properties near the boundaries. In such cases, a high resolution mesh or particle distribution is needed.

The potential of the proposed formulations (Eqs. 3.18 and 3.19) to accurately predict the wall shear stress can be reinvestigated more precisely in the case of an oscillating wall boundary. Figure 3.20 shows the variation of wall shear stress over one period using different formulations compared to the analytical solution for the case of flow over an oscillating plate with a particle spacing of $dy = 2.2388 \times 10^{-5}$ (m).

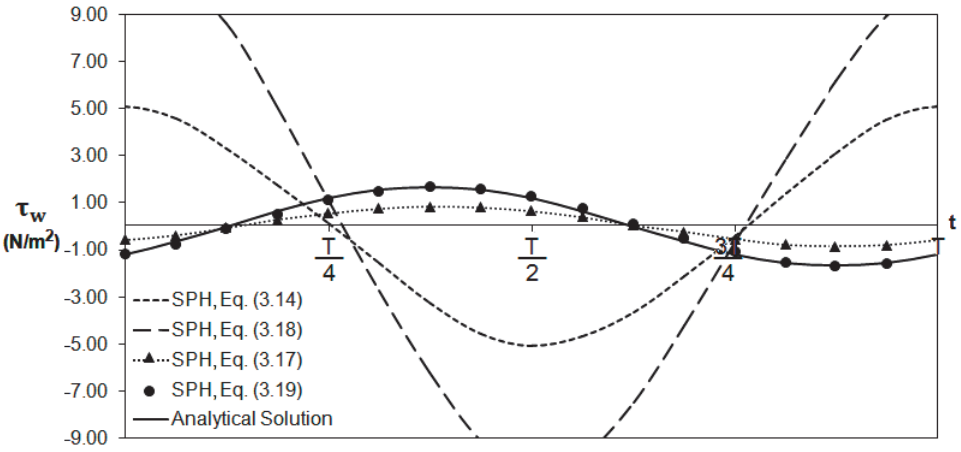

Fig. 3.20. Wall shear stress profiles for flow over an oscillating plate and comparison with analytical solution; $U_{o,m} = 0.3\ (\mathrm{m/s})$ and $\omega = 10\pi\ \left(\frac{\mathrm{rad}}{\mathrm{s}}\right)$ $(\mathrm{T} = 0.2\ \mathrm{s})$.

Equations (3.17) and (3.19) are much more compatible with the physics of no-slip boundary condition on the walls, a condition which results in a relative velocity of flow with respect to the wall equals zero. In addition, a constant tangential velocity should result in a zero gradient of this parameter; this condition is also satisfied by Eqs. (3.17) and (3.19), but not by Eqs. (3.14) and (3.18).

Equations (3.14) and (3.18) failed completely to provide correct results and Eq. (3.17) did not lead to accurate values for wall shear stress. In Fig. 3.21, the L_2 error norm of wall shear stress is plotted against particle spacing for Eqs. (3.17) and (3.19). Similar to previous simulations, the error norm converges to a higher value when Eq. (3.17) is used. The norm of wall shear stress error converges at a rate close to unity for Eq. (3.19).

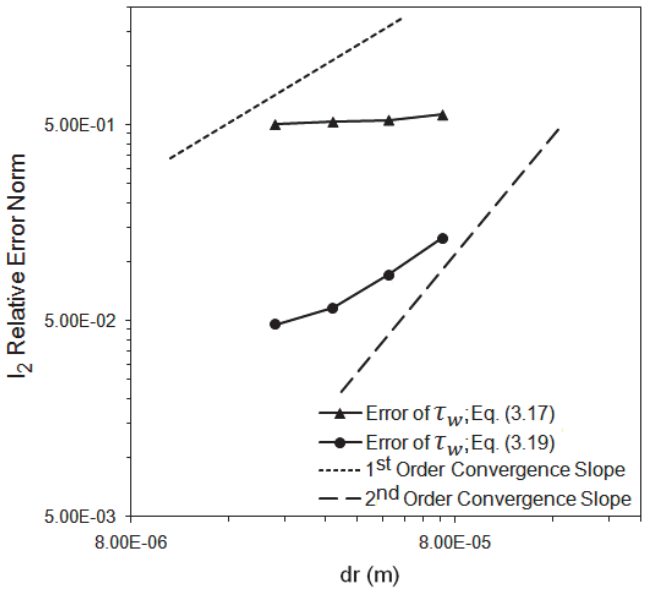

Fig. 3.21. L_2-norm of relative error for wall shear stress calculations over a period. Flow over an oscillating plate; $U_{o,m} = 0.3\ (\mathrm{m/s})$ and $\omega = 10\pi\ \left(\frac{\mathrm{rad}}{\mathrm{s}}\right)$.

The proposed formulation (Eq. 3.19) can be employed regardless of the curvature of the wall at the local region of interest. However, to achieve the desired accuracy for a larger curvature of the wall, a smaller smoothing length, h, or higher particle resolution is required in order to make the curved wall resemble a flat wall region. These constraints are similar for all computational methods.

3.5. Lid Driven Cavity Flow

The next test case deals with flow inside a square cavity. The fluid is driven due to the movement of the upper boundary. In this case, the boundary consists of four walls parallel to x- and y- axes located at $x = 0$, $x = L$, $y = 0$, and $y = L$. The Reynolds number is defined as $Re = U_o L/\nu$, where U_o is the upper boundary velocity parallel to

the x- axis. The physical properties are selected as $L = 1$ (m), $\rho_o = 1$ (kg/m^3), and $\nu = \frac{1}{3200}$ (m^2/s) and $\frac{1}{5000}$ (m^2/s) for $Re = 3200$ and 5000 cases, respectively.

Velocity profiles simulated at mid-vertical and mid-horizontal cross-sections of the cavity for $Re = 3200$ and 5000 and different initial particle spacing are shown in Figs. 3.22 and 3.23. The numerical results, for different particle spacing, are compared to the results of Ghia et al. (1982). Since the Lagrangian nature of SPH does not allow finding a large number of particles at a specific cross-section, all the particles within a thin strip with a width equal to the initial particle resolution are considered in order to plot the velocity profiles.

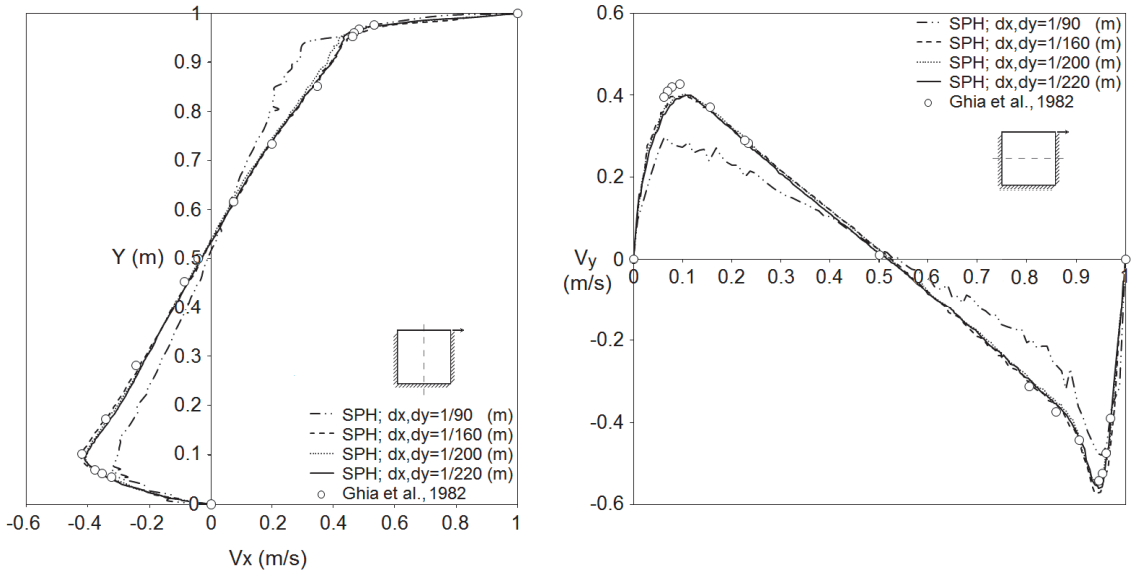

Fig. 3.22. Velocity profiles for $Re = 3200$ obtained using SPH for particle resolutions of $\frac{1}{90}; \frac{1}{160}; \frac{1}{200}; \frac{1}{220}$ (m) at: (a) mid-horizontal cross-section; and (b) mid-vertical cross-section of the cavity. The results are compared to the data of Ghia et al. (1982).

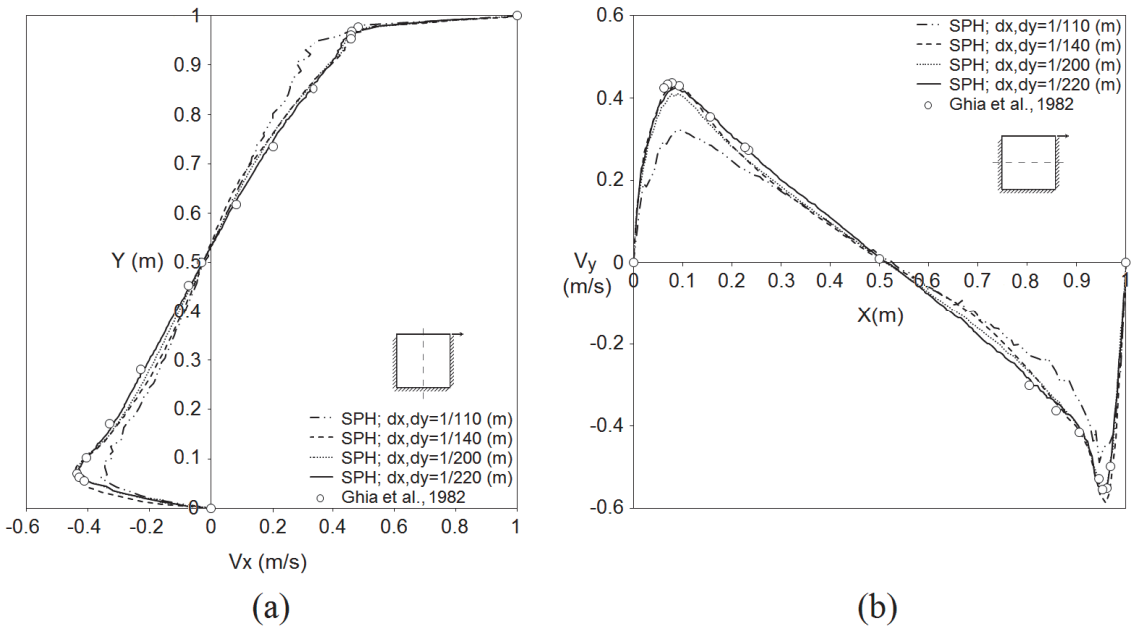

Fig. 3.23. Velocity profiles for $Re = 5000$ obtained using SPH for particle resolutions of $\frac{1}{110}; \frac{1}{140}; \frac{1}{200}; \frac{1}{220}$ (m) at: (a) mid-horizontal cross-section; and (b) mid-vertical cross-section of the cavity. The results are compared to the data of Ghia et al. (1982).

As expected, employing higher number of particles resulted in smoother velocity profiles. The effect of different particle resolutions is analysed through a convergence study using L_2-relative error norm criteria. Here the reference values are the results reported by Ghia et al. (1982). The L_2-relative error norms for both velocity components at two cross-sections of the cavity are shown in Fig. 3.24. The rate of spatial convergence for this case lies between first and second order as demonstrated for the previous oscillating flow case.

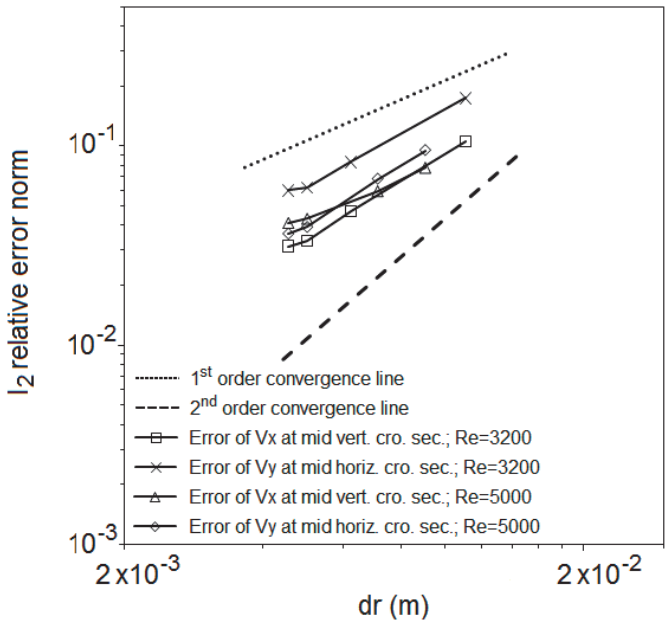

Fig. 3.24. L_2- norm of relative error versus spatial resolution for velocity components at two cross sections of the cavity.

A series of numerical tests shows that for cases at lower Reynolds numbers ($Re = 400 - 1000$) increasing the number of fluid particles more than 129×129 (reducing the particle spacing less than $dr = \frac{1}{130}(\mathrm{m}) = 0.00769\ (\mathrm{m})$) leads to converged velocity profiles. However, for higher Reynolds numbers ($Re = 3200 - 5000$), the same level of convergence occurs with 199×199 number of particles, corresponding to particle spacing less than $dr = \frac{1}{200}(\mathrm{m}) = 0.005\ (\mathrm{m})$. The velocity profiles for $Re = 400$ and 1000 are not shown here as they are frequently presented in SPH literature.

For $Re = 3200$ and the highest particle resolution (219×219), the maximum density change (0.85%) occurs for a few particles located at the right top corner of the cavity, however the average change in the density of all particles in the domain is

0.16%). For $Re = 5000$ at the same resolution, the maximum density change was 0.95% at the same location. The average change in the particle density is 0.17%.

The lid driven cavity flow consists of a main vortex and a couple of weak vortices at the bottom left, bottom right and top left corners of the cavity. In fact, the top left vortex appears for Reynolds numbers higher than 3200 (Ghia et al, 1982). Figure 3.25 shows the normalized velocity vector field at top left corner region of the cavity for Reynolds numbers equal to 1000 and 5000.

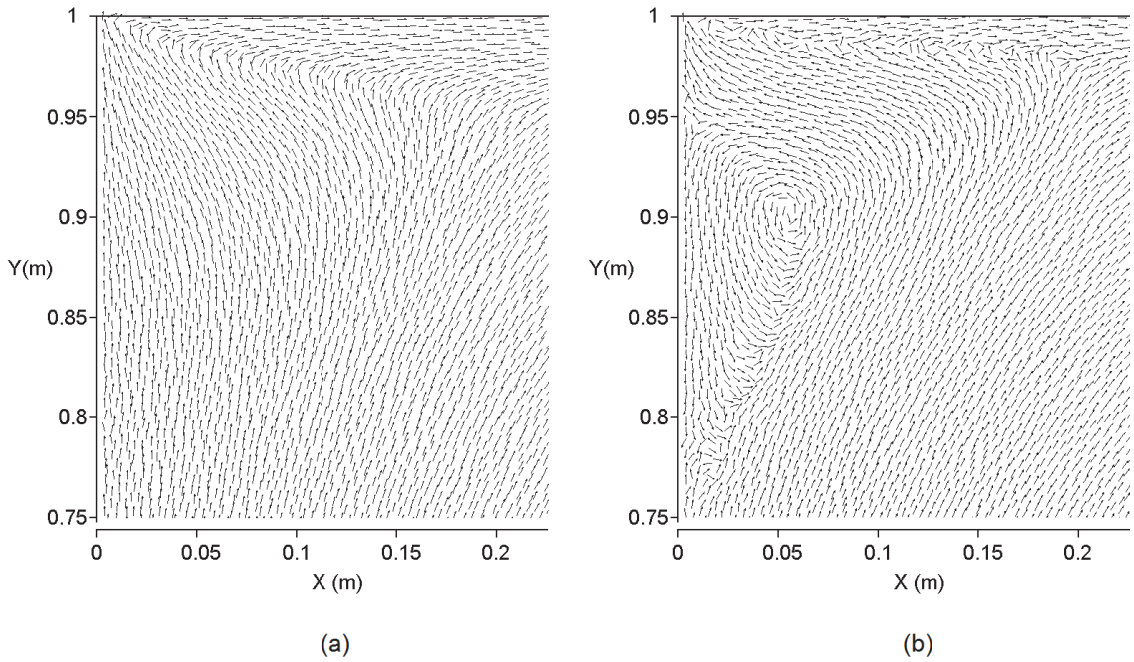

Fig. 3.25. Normalized velocity vector field at top left corner of the cavity; a) $Re = 1000$, and b) $Re = 5000$; particle resolution (219×219).

The center of the weak vortex at the top left corner of the cavity for Reynolds numbers of 3200 and 5000 is determined at (0.0405,0.8885) and (0.05775,0.9046) which is in

good agreement with the data obtained by Ghia et al. (1982): $(0.0539,0.8986)$ and $(0.0627,0.9105)$, respectively.

Interestingly, in the simulations dealing with Poiseuille and oscillating flow (Sec. 3.1), applying a speed of sound as low as five times the maximum velocity allowed the control of density fluctuations. However, it was not the case for lid-driven cavity flow and a void appeared at the centre of the recirculation zone for this order of sound speed (Fig. 3.26a).

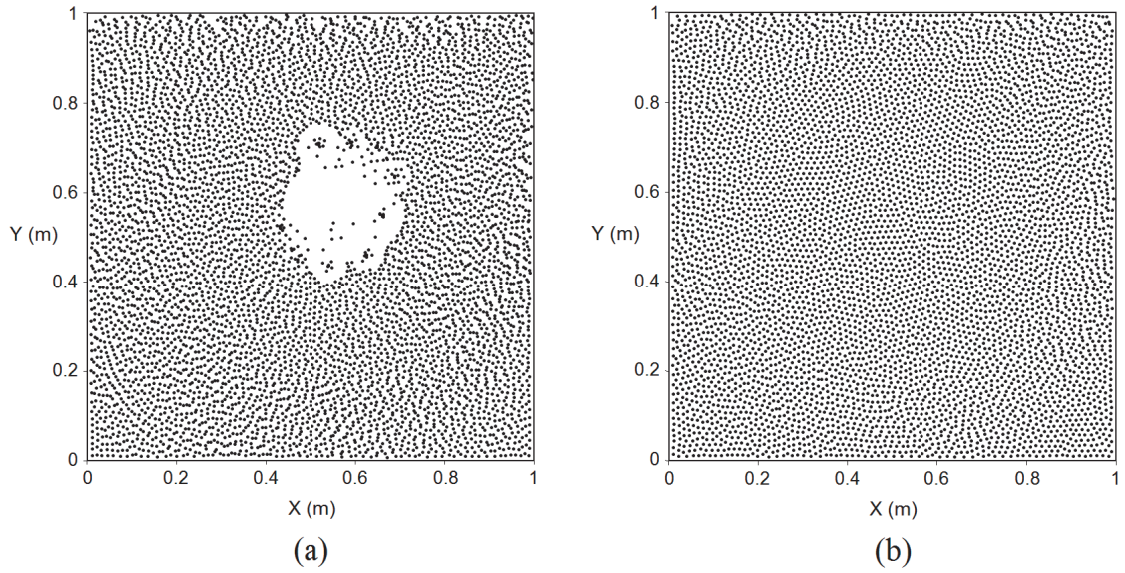

Fig. 3.26. The effect of sound speed to prevent the appearance of a numerical void at the center of cavity; a) $c = 10U_{Lid}$, and b) $c = 65U_{Lid}$; plots are at $t = 16.8$ (s).

This numerical artifact leads to incorrect computation of the density and therefore the pressure field. Typically, in order to avoid this void, a higher artificial speed of sound has to be applied. This problem has already been reported in the simulations of similar lid-driven cavity flow at $Re = 400$ and 1000 (Lee et al., 2008) and has been solved by using a speed of sound ten times higher than the usual recommended value (i.e, one hundred times larger than lid velocity). This artifact also appeared when the flow over a backward

facing step was modeled at $Re = 100$ (Issa et al., 2005) and it required a value for the speed of sound representing forty times the maximal flow velocity. In the simulations of lid-driven cavity flow, applying a speed of sound equal to $c = (45 - 65)U_{Lid}$ was required, for low particle resolution cases (less than 109×109), to prevent void appearance in the domain for all Reynolds numbers ($Re = 400 - 5000$). Interestingly, it is found in this thesis that for cases with a particle resolution higher than 139×139, a more realistic speed of sound in the range of $c = (12 - 15)U_{Lid}$ can prevent the occurrence of the void.

3.6. Summary

In this chapter, the ability of the SPH method to simulate internal transient and oscillating flows at different flow characteristics and lid-driven cavity flow at moderate Reynolds numbers were examined. The selected test cases were chosen because the exact solutions and reference data are available to ensure a precise validation of the numerical results. Also the selected benchmark cases have similarities to the geometry (arterial channels and heart cavities) and flow characteristics (oscillating pressure waveforms and arterial wall movement) found in the cardiovascular system. The main conclusions of this work are summarized as follows:

1) "*Form II*", Eq. (2.21), for modeling the viscous term showed more accuracy in the simulations, and unlike "*Form I*", Eq. (2.20), it is not dependent on the type of kernel function and flow characteristics.

2) Using the XSPH variant, especially when particle resolution is not high and flow is subjected to high velocity gradients, can generate undesirable particle disorders.

3) The SPH method was able to correctly simulate internal oscillating flows even when there was a large phase lag between the oscillation of the derived velocity and applied pressure difference and moving boundary.

4) Although the theoretical convergence rate of SPH discretization has been proven to be second order; several reasons affect the accuracy of SPH calculations and the rate of spatial convergence lies between first and second order,

5) A modified formulation for wall shear stress calculations was presented and verified against exact solutions.

6) Increasing particle resolution can avoid the occurrence of computational voids while maintaining the speed of sound at a reasonable value.

All simulated cases did not show unacceptable compressibility effects.

Chapter 4

Pulsatile Flow inside a Model of Left Heart Cavity

The previous chapter provided a comprehensive verification of SPH formulation and validation of the computational code. In this chapter, the results of the first attempt to simulate flow inside a model of the left ventricle (LV) of the heart, using the SPH method, are presented. Flow in the LV is comprised of a combination of oscillating flow in tubes and flow in a lid-driven cavity. First, the combination of these two benchmark cases is tested by simulating a pulsatile flow inside a rectangular cavity. An approach to deal with inflow and outflow boundary conditions is introduced and the important role of particle resolution in determining the order of accuracy of SPH simulations is also demonstrated. Finally, the flow in a model of LV cavity under pulsatile inflow condition is simulated and the ability of SPH to track fluid properties history is illustrated.

4.1. Introduction

The flow pattern in heart cavities is of great interest when studying cardiovascular diseases. Current numerical simulations dealing with flow inside the heart cavities are mainly based on conventional mesh-based methods: finite differences, finite volumes and finite elements (Taylor and Yamaguchi, 1995; Baccani et al., 2001; Nakamura et al., 2002; Long et al., 2003; Saber et al., 2003; Cheng et al., 2005; Pedrizzetti and Domenichini, 2005; Liang et al., 2007; Doenst et al., 2009), immersed boundary method

(Lemmon and Yoganathan, 2000; McQueen and Peskin, 2000; Peskin, 2002) and arbitrary Lagrangian-Eulerian approach (FV discretization: Vierendeels et al., 2000 and FE discretization: Watanabe et al., 2002). These methods have already demonstrated good capabilities in simulating cardiovascular flows and generated very interesting results with clinical and practical implications. However, some important aspects in cardiovascular flows, mainly those related to pathological conditions, can be difficult to capture using mesh-based methods. Examples include flow in complex geometries, tracking the history of blood flow properties, thrombus formation and the break off of red blood cells (microcirculation). The simulation of such characteristics requires CFD methods based on a Lagrangian particle approach instead of an Eulerian mesh-based approach.

In this chapter, the results of SPH simulation of a pulsatile flow inside a model of LV cavity (see Fig. 4.1) are presented. As this work represents the first attempt to simulate such flow using a particle method, the model does not include moving boundaries. Therefore, the main objective is to extend the application of SPH to simulate internal pulsatile flows at moderate Reynolds number in a complex geometry mimicking an LV cavity.

Simulating flow that is characterized by high pulsatility and moderate Reynolds number using SPH is challenging. Chapter 3 has already provided a comprehensive verification of SPH formulations and validation of the computational code developed. The combination of oscillating flow in tubes and flow in a lid-driven cavity is tested by simulating pulsatile flow in a rectangular cavity and the results are compared to those

obtained using the FV method, as no analytical solution exists for this problem. In addition, an approach to deal with inflow and outflow boundary conditions is introduced.

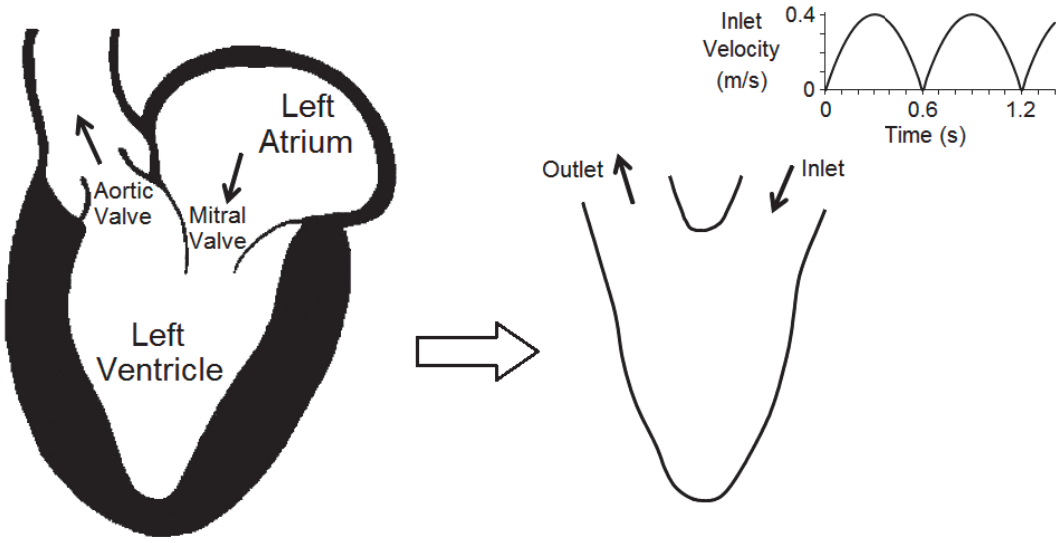

Fig. 4.1. Left ventricle (LV) geometry; inlet and outlet boundaries; and pulsatile inlet velocity.

The order of accuracy in the simulations, relative to particle resolution, is also investigated. Finally, the flow in a model of LV cavity under pulsatile inflow conditions is simulated and the ability of SPH to track fluid properties history is illustrated.

4.2. Methodology and Formulations

Unsteady Navier-Stokes equations for a Newtonian fluid flow are considered as Eqs. (2.5) and (2.6). The assumption of Newtonian behavior for blood flow in large arteries and heart cavities is considered as realistic (Waite and Fine, 2007). The effect of gravity is negligible in all cases investigated in this work.

In this work, Navier-Stokes equations are discretized based on Eqs. (2.8), (2.12), and (2.21) as

$$\frac{d\rho_a}{dt} = \sum_b m_b(\boldsymbol{V}_a - \boldsymbol{V}_b).\boldsymbol{\nabla}_a W_{ab} \tag{4.1}$$

$$\frac{d\boldsymbol{V}_a}{dt} = -\sum_b m_b(\frac{P_a+P_b}{\rho_a\rho_b})\boldsymbol{\nabla}_a W_{ab} + \sum_b m_b \frac{(\mu_a+\mu_b)\boldsymbol{r}_{ab}.\boldsymbol{\nabla}_a W_{ab}}{\rho_a\rho_b\,(r_{ab}^2+\eta^2)}\boldsymbol{V}_{ab} \tag{4.2}$$

where $\boldsymbol{V}_{ab} = \boldsymbol{V}_a - \boldsymbol{V}_b$ is the relative velocity vector between particles a and b, P is pressure, μ is dynamic viscosity and η^2 is a small term to avoid the singularity. Alternative forms are available in the literature (Monaghan, 1992; Cleary, 1998; Monaghan, 2006). The formulation for pressure gradient in Eq. (4.2) was shown to give slightly superior results compared to the conventional pressure gradient term (Colagrossi and Landrini, 2003) and is variationally consistent (Vila, 1999). The formulation for the viscous term used in Eq. (4.2) was previously shown to model the viscous behavior with good accuracy for the current application at moderate Reynolds numbers. The equation of state based on Eq. (2.14) is used to compute the pressure field.

A fourth order, quartic, spline kernel for 2D simulations, Eq. (2.4), is used due to its high stability. The smoothing length, h, is considered 1.25 times larger than the initial particle spacing.

The new position of the particles at each instant is derived by time integration of the velocity field based on Eq. (2.28). A second order predictor-corrector scheme is employed for time integration of the equations (see Sec. 2.3.2) and the time step is controlled by Eq. (2.34).

Wall boundary conditions are implemented by placing a set of particles exactly on the wall with the same distance as the initial fluid particles and some layers of fixed

imaginary particles parallel to the walls outside the domain (see Sec. 2.3.6). To easily apply a Neumann type boundary condition for pressure on the walls, imaginary particles are arranged so that each one is allocated to a normal line drawn from a wall particle. Implementation of this idea is presented in Fig. (4.2) for different configurations of wall boundaries.

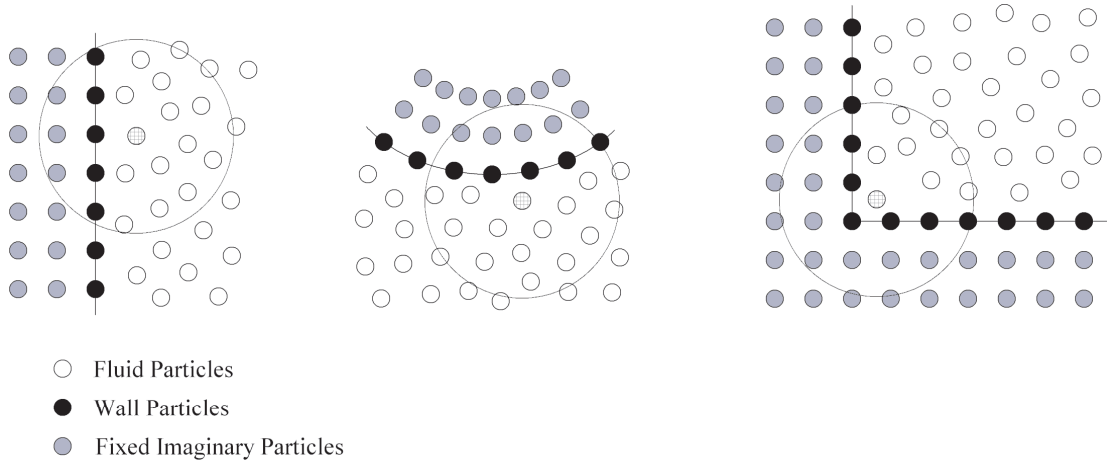

Fig. 4.2. Treatment of wall boundaries; one layer of wall particles and two layers of imaginary particles for different boundary configurations.

In this study, the velocity of wall particles is set to zero, but contrary to previous studies (Koshizuka et al., 1998; Shao and Lo, 2003; Violeau and Issa, 2007; Lee et al. 2008), the imaginary particles are given extrapolated velocities based on Eq. (2.36). Through a series of numerical tests, it is found in this thesis that giving extrapolated velocities instead of zero velocity to the imaginary particles better prevents the particles from penetrating the walls. It is caused by reducing the magnitude of the perpendicular velocity component of the fluid particles approaching a wall boundary. This approach is efficient when modeling highly inertial flows with a relatively low particle resolution.

A linked list method (See Sec. 2.3.4) is employed here to optimally search for neighboring particles.

4.3. Oscillating Flow with $W_o = 16$

The specific oscillating frequency of the flow in LV leads to perform a validation for a Womersly type flow with the oscillation period of $t = 0.61$ (s) which is in the same order of magnitude as that for simulating flow in the LV model. The results are compared to theoretical predictions (Eq. 3.6).

The distance between the two plates is $d = 0.01$ (m), an average diameter for arteries, and the fluid density and kinematic viscosity are $\rho = 1000$ (kg/m^3) and $\nu = 1 \times 10^{-6}$ (m^2/s), respectively. This corresponds to an oscillating Reynolds number ($Re_o = d^2\omega/\nu$) of 1024 and Womersly number ($W_o = \frac{d}{2}\sqrt{\omega/\nu}$) of 16. The simulation is performed for pressure gradient amplitude of 2500 (N/m^3). The particles are initially distributed with a uniform spacing of $dx = dy = 1.2821 \times 10^{-4}$ (m) (77 particles in span of the plates).

The oscillating velocity profiles are shown in Fig. (4.3) and the results are compared to the existing analytical solution (Eq. 3.6). There is a very good agreement between SPH results and the analytical solution. The variation in density remains well within the acceptable range of incompressibility assumption, with variations less than 0.0006%.

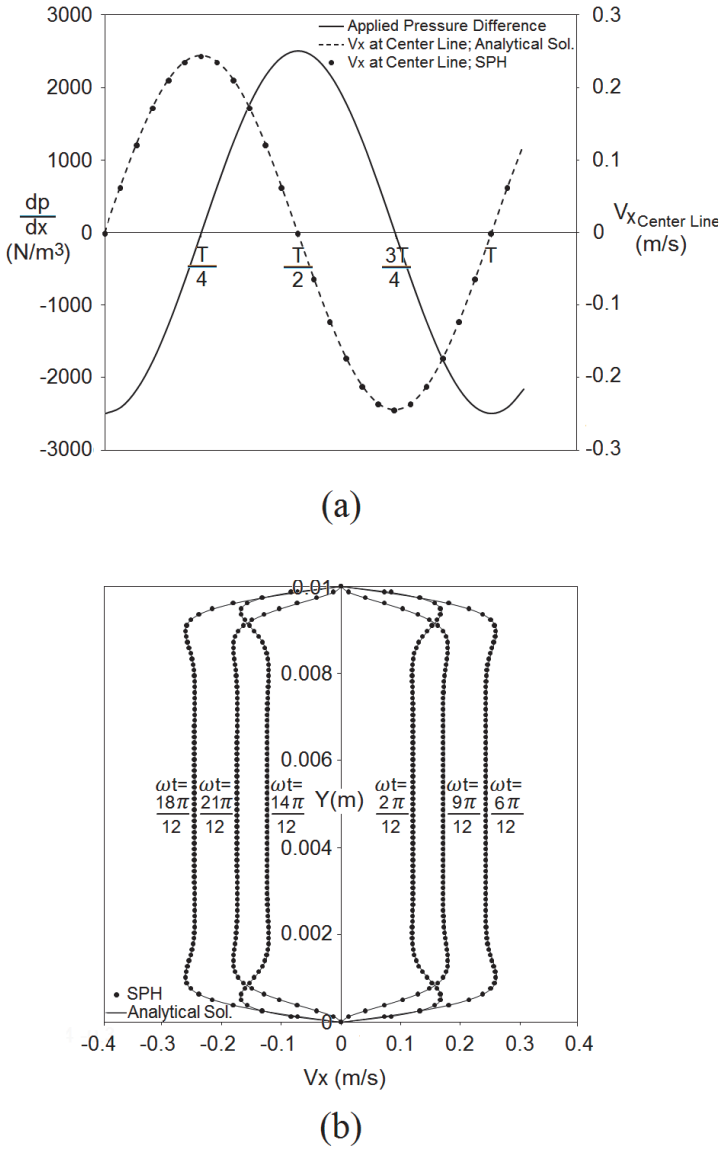

Fig. 4.3. Oscillating flow between two parallel plates over one period; 2500 $(\mathrm{N/m^3})$ and $W_o = 16$: (a) applied oscillating pressure wave form and computed centerline velocity; and (b) velocity profiles over one period.

In Fig. 4.4, the average L_2-relative error norm of velocity during the simulations is plotted against particle spacing. As it was reported in chapter 3, convergence rate is similar to unity. In the continuous domain of Eq. (2.1), the convergence rate of SPH can

be shown to be second order, $O(h^2)$. However, it is known that with a disordered set of points, the SPH order of convergence is nearer to one.

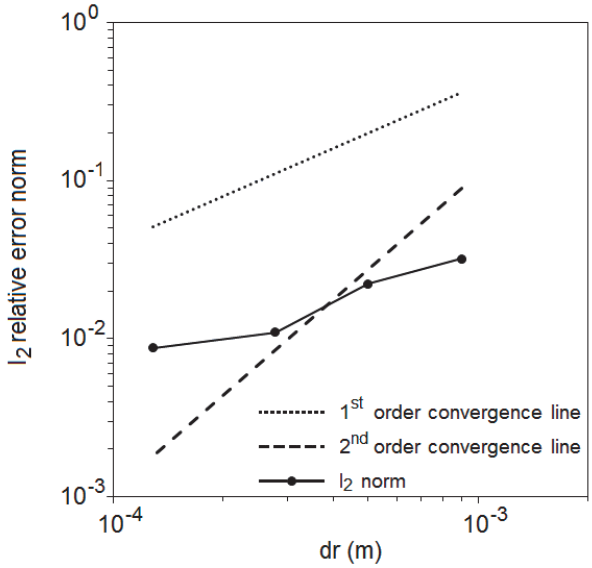

Fig. 4.4. Oscillating flow between two parallel plates over one period; L_2-norm of the relative error against particle spacing.

The no-slip boundary condition treatment employed did not fail although the flow boundary layers near the plates are highly oscillating.

4.4. Pulsatile Flow inside a Rectangular Cavity

The geometry consists of a rectangular cavity with dimension of $0.04\,(\mathrm{m})$ by $0.05\,(\mathrm{m})$ (Fig. 4.5). A pulsatile flow enters the cavity with a flat profile.

In this case, the dominant inertial force of the inlet jet induces enough momentum to maintain the flow in the domain without applying a body force or boundary movement even during the deceleration phase.

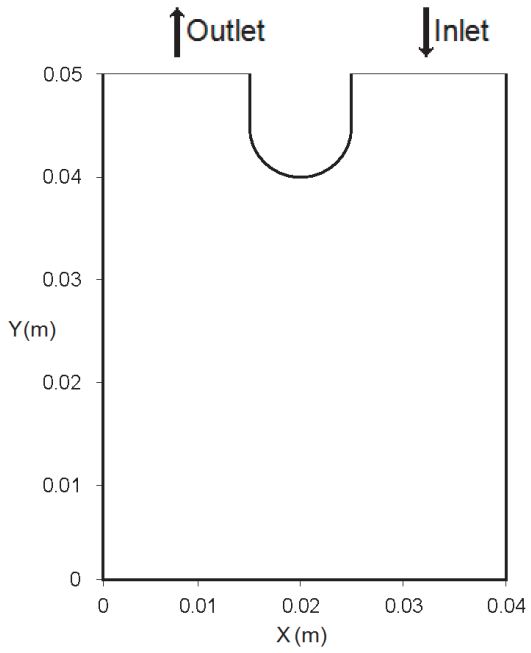

Fig. 4.5. The 2D geometry used for pulsatile flow in a rectangular cavity.

As there is no analytical solution or experimental study for this problem, the results are compared with those obtained by FV method using FLUENT (Ansys Inc., Lebanon, NH, USA), a widely used commercial software for simulation of fluid flows. A second-order scheme for time and spatial discretization was employed and time step and mesh independence study were carried out in order to make sure that the solution has converged. It should be mentioned that FV simulations are used for comparison purposes, not validation of SPH results. They are also used to evaluate the validity of the approach proposed for the implementation of inflow and outflow boundary conditions, as shown in the following section (Sec. 4.4.1), and to examine the order of convergence of the SPH scheme.

4.4.1. Inflow and Outflow Boundary Conditions

Rigid walls and periodic open boundaries are widely simulated in SPH (Monaghan 1994; Takeda et al., 1994; Morris et al., 1997; Koshizuka et al., 1998; Cummins and Rudman, 1999; Shao and Lo, 2003). On the other hand, implementation of inflow and outflow boundary conditions in SPH is not straightforward and is still under investigation (Lastiwka, 2009). The difficulties in simulating such boundary conditions in SPH originate from the meshfree nature of the particle methods. There are two primary challenges: (1) As fluid elements are represented by a set of particles moving in a Lagrangian frame of reference, there is no way to ensure the existence of particles exactly at these boundaries at all instants during the simulations; and (2) particles near such boundaries do not have enough particles in their neighboring domain.

One way of dealing with these issues is to apply a periodic boundary condition in which particles near the inlet interact with the particles near the outlet. However, for the test case under consideration here, this approach is problematic, as the arrangement of particles at the inlet is uniform (imposed boundary condition) and this is not the case at the outlet. Furthermore, applying the periodic boundary condition restricts the types of inflow and outflow boundary conditions to be used. So, in this study an alternative simple and effective approach to handle the difficulties in simulating this kind of inflow and outflow boundaries is applied. The physical inflow and outflow boundaries are displaced to new locations called numerical injection and ejection boundaries (Fig. 4.6). The numerical particle injection boundary is located upstream of the physical inflow boundary and the numerical ejection boundary is located downstream of the physical outflow boundary. The two boundaries (numerical and physical) are connected by an

artificial channel in order to maintain unidirectional flow in the inlet and outlet regions. The length of this channel has to be greater than the supporting size of the interpolating kernel function in order to ensure that any particle close to an inflow or outflow physical boundary has enough particles in its kernel support. Also, a uniform physical condition in the region enclosed between the numerical and physical boundaries must be created. Each particle exiting the numerical ejection boundary is stored and then injected through the inlet numerical boundary with the prescribed inflow properties. This technique avoids creating new injected particles that will occupy computer storage memory. To maintain the imposed flow rate at the inlet, a new particle is not injected until the previous particle has moved into the numerical domain by a distance equal to the initial particle spacing. This technique is not strictly non-reflecting but is sufficient for the present purpose.

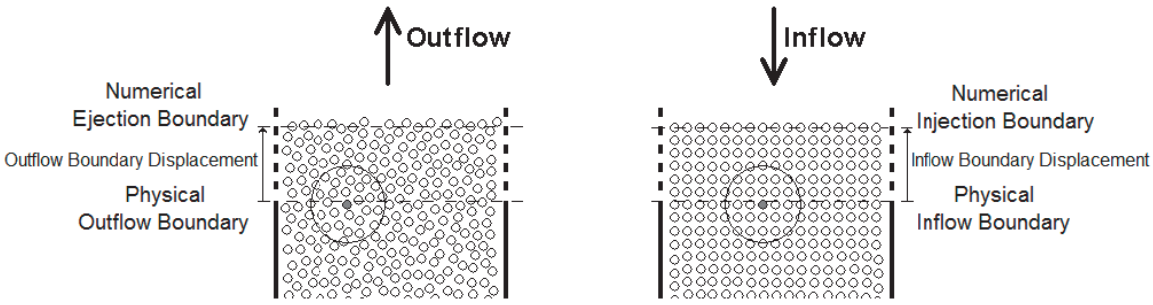

Fig. 4.6. Implementation of inflow and outflow boundaries.

In this study, boundary conditions at the inlet and outlet are defined so that continuity is always satisfied. For an incompressible flow with only one inlet and one outlet, this leads to

$$(AV)_{inlet} = (AV)_{outlet} \tag{4.3}$$

here, A is the cross section area of the channel and V is the mean velocity normal to the cross section at the inlet and outlet. Having the same size, in this case, for both the inlet and outlet naturally leads to

$$V_{inlet} = V_{outlet} \tag{4.4}$$

Therefore, conservation of mass results in an equality of mean velocity normal to the inlet and outlet. The inlet velocity profile is imposed and the outlet velocity is determined based on Eq. (4.4) at each instant.

Particles located in the inlet region, between the numerical and physical boundaries, are forced to maintain the imposed inlet velocity at each instant, while density and pressure of these particles are unknown and calculated based on SPH formulations and information about their neighboring particles, particularly those located in the interior domain. The same strategy is applied for the particles located in the outlet region.

4.4.2. Velocity Profiles

After satisfying the periodicity of the results, the velocity profiles at different instants of a cycle at mid-vertical and mid-horizontal cross-sections of the cavity were extracted and compared with the results of the FV method in Figs. 4.7(a-f). The effect of spatial resolution on the results is examined by considering different particle resolutions. Here, the data for four different particle resolutions (30610 fluid particles, $dr = 2.6726 \times 10^{-4}$ (m); 50506 fluid particles, $dr = 2.0833 \times 10^{-4}$ (m); 73848 fluid particles, $dr = 1.7241 \times 10^{-4}$ (m); 101616 fluid particles, $dr = 1.4706 \times 10^{-4}$ (m)) are plotted. Smoother velocity profiles result with increased particle resolution.

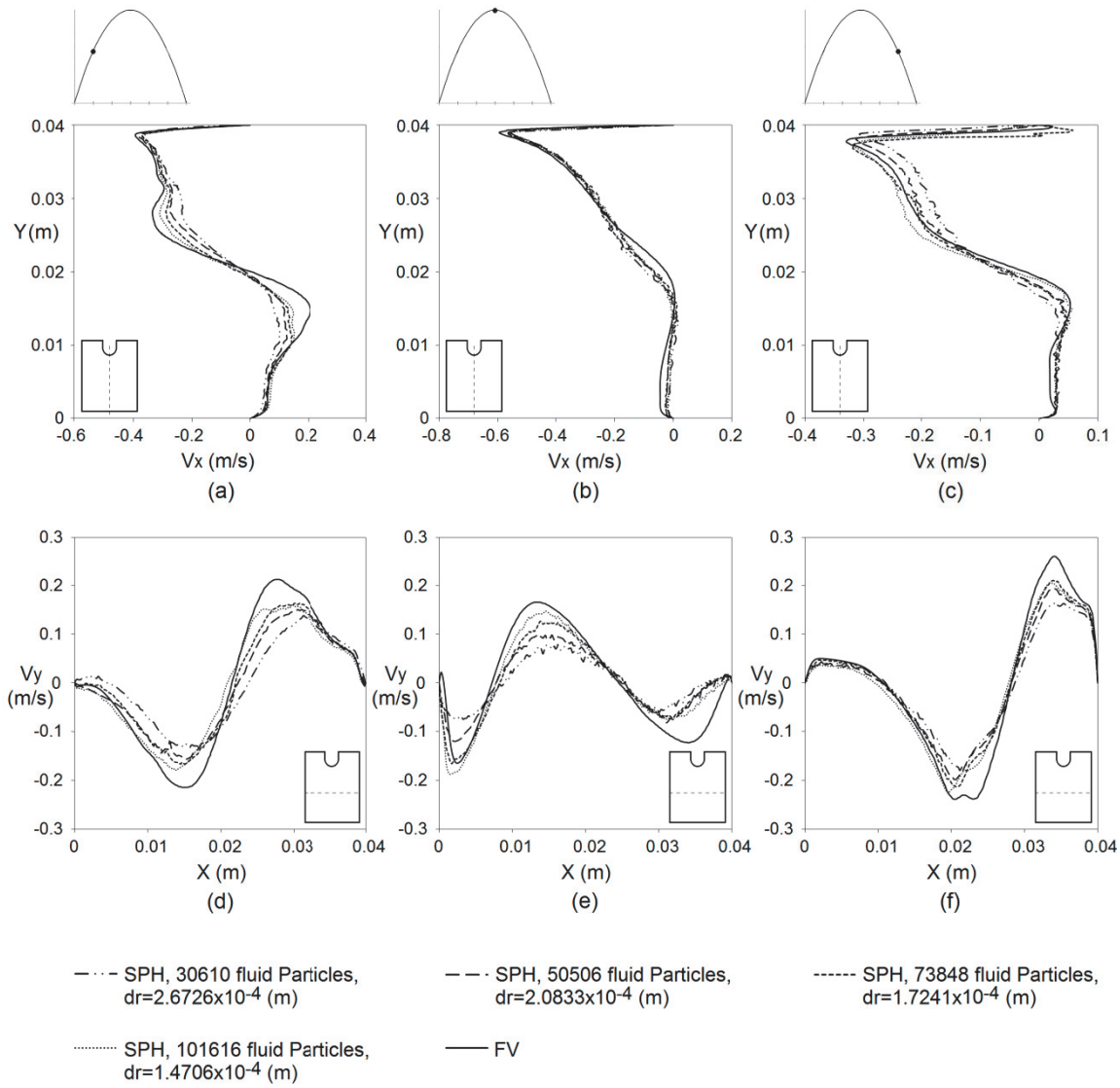

Fig. 4.7. SPH velocity profiles at mid- horizontal and vertical cross-sections of the LV cavity in comparison with FV and the effect of particle resolutions on the profiles; at mid horizontal cross section: a) $t = 0.1(\mathrm{s})$, b) $t = 0.3(\mathrm{s})$, and c) $t = 0.5(\mathrm{s})$ of a cycle; and at mid vertical cross section: d) $t = 0.1(\mathrm{s})$, e) $t = 0.3(\mathrm{s})$, and f) $t = 0.5(\mathrm{s})$ of a cycle.

Along the centerlines in Fig. 4.7, convergence of the velocity profiles is evident, but there is a discrepancy for the peak velocity magnitudes between the SPH and FV results. The reason for this is not known. The vertical component of the velocity at $0.3(\mathrm{s})$ (peak

ejection phase) at mid-sections along the inlet and outlet boundaries are presented and compared with the results of the FV method in Figs. 4.8(a-b).

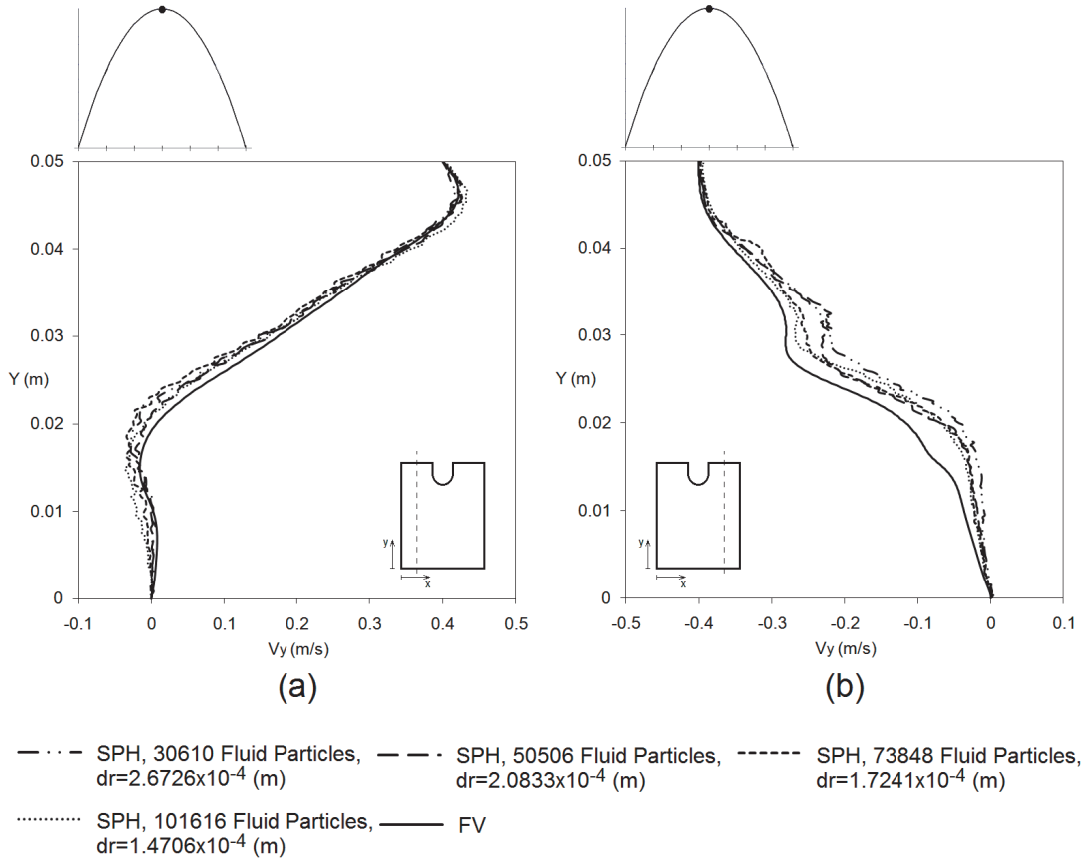

Fig. 4.8. SPH velocity profiles at left and right vertical cross sections of the LV cavity in comparison with FV and the effect of particle resolutions on the profiles at: a) left vertical cross-section; and b) right vertical cross-section.

In general, the SPH results are in satisfactory agreement with those extracted based on FV, particularly close to the inlet and outlet regions. To examine specifically the efficiency of the approach adopted for inflow and outflow boundary conditions, the profile of the vertical component of the velocity vector across the outlet channel of the cavity for different instants of a cycle at $Y = 0.045$ (m) are shown in Figs. 4.9(a-c). The

SPH results are in reasonable agreement with the results of the FV method.

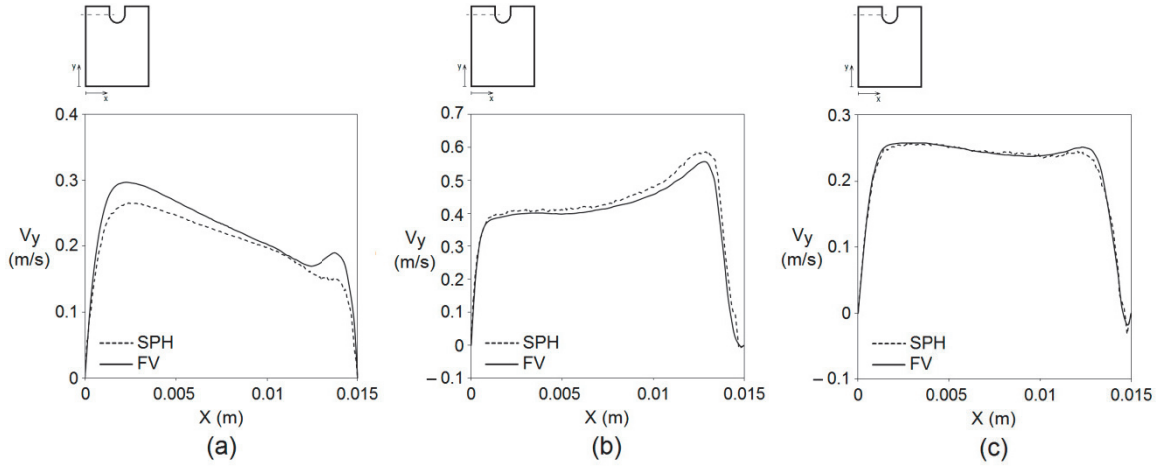

Fig. 4.9. SPH velocity profile across the outlet channel of the cavity in comparison with FV result: a) $t = 0.1(\mathrm{s})$, b) $t = 0.3(\mathrm{s})$, and c) $t = 0.5(\mathrm{s})$ of a cycle. (101616 fluid particles, $dr = 1.4706 \times 10^{-4}$ m)

This case also allows the discussion of the truncation errors in SPH simulations. Indeed, from SPH formulation, one expects second order accuracy. However, the accuracy in SPH calculations is highly affected by the smoothing length, particle spacing and non-uniformity distribution of the particles due to their movement during the simulation (Quinlan et al., 2006; Vaughan et al., 2008). It has previously been shown that SPH simulations exhibit accuracy greater than first order but less than second order (Vacondio et al., 2011). The equivalence with first and second-order accurate FV schemes by employing low and high particle resolutions on the accuracy of SPH results is shown in Figs. 4.10 (a-d) where SPH velocity profiles at two mid cross-sections of the cavity at 0.3 (s) are plotted. The SPH results of employing a low particle resolution (9094 fluid particles, $dr = 4.5454 \times 10^{-4}$ (m)) are compared with those obtained using the first order accurate FV spatial discretization, while the SPH results for high particle

resolution (101616 fluid particles, $dr = 1.4706 \times 10^{-4}$ (m)) are compared to those obtained using the second order accurate FV spatial discretization.

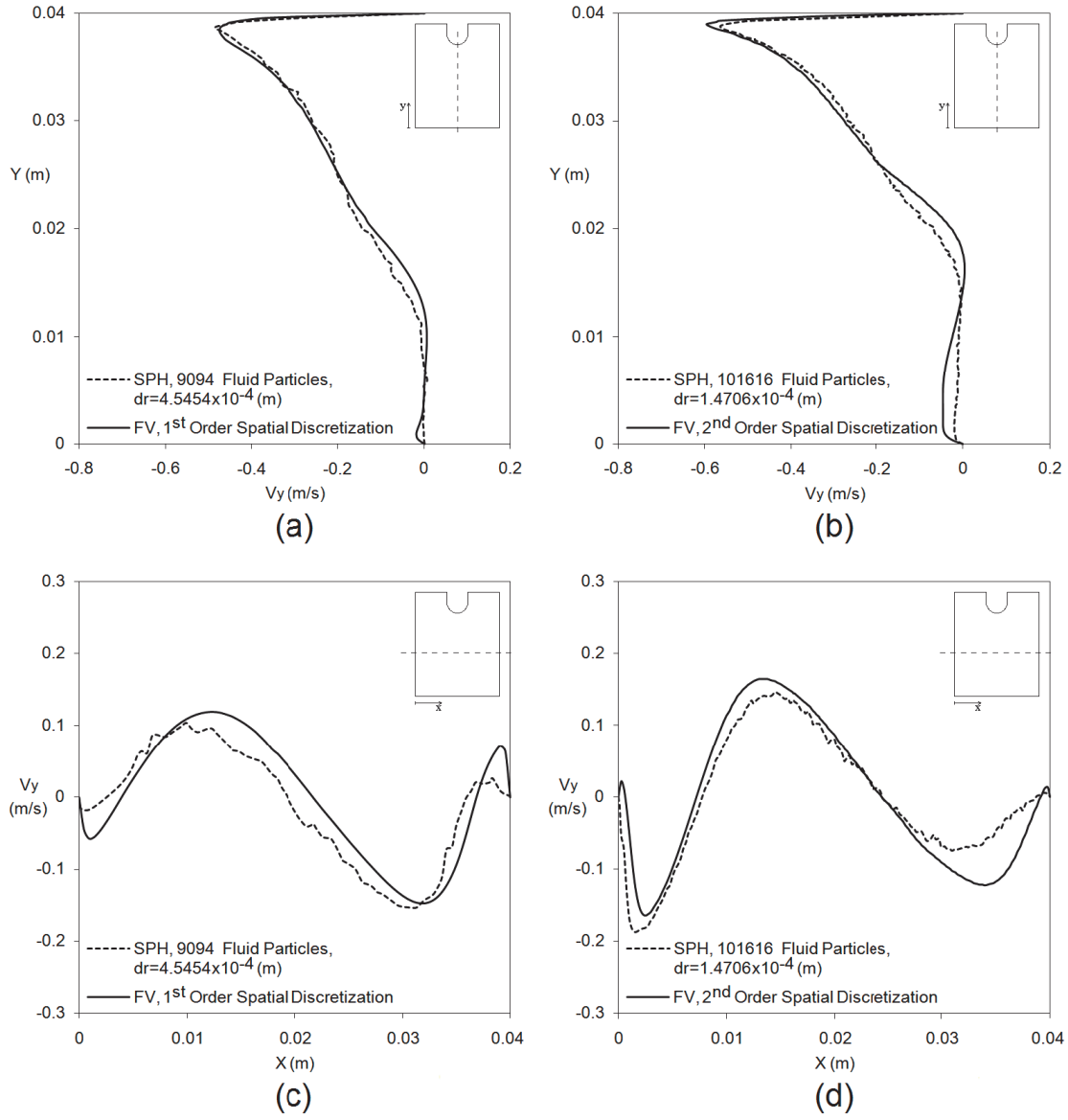

Fig. 4.10. SPH velocity profiles in mid- horizontal and vertical cross sections of the LV cavity compared to FV at $t = 0.3$ (s). In mid vertical cross section: a) SPH with low particle resolution compared to FV with 1st order accurate spatial discretization, b) SPH high particle resolution compared to FV with 2nd order accurate spatial discretization; and in mid horizontal cross section: c) SPH low particle resolution against FV with 1st order accurate spatial discretization, d) SPH high particle resolution against FV with 2nd order accurate spatial discretization.

These results illustrate how the SPH simulations with particle resolution exhibit behavior equivalent to a FV scheme of different accuracy order. The lower particle resolution gives results similar to the first-order FV scheme, while the second-order accuracy can be reached by increasing the particle resolution.

As it has been previously mentioned in Sec. 3.4, for simulations with low particle resolution in lid-driven cavity case, employing a high speed of sound was needed to prevent the appearance of the void at the center of the main vortex. Interestingly, this void did not appear when simulating pulsatile flow inside the cavity even when a standard value for the speed of sound was used ($c = 10\ U_{max}$). This can be explained by the unsteady nature of the flow. The coherent structures in the domain dynamically change in response to the pulsatile inlet flow. This probably does not allow enough time for the creation of a void in the domain. The particles located at the center of the domain, potentially subjected to numerical void appearance, do not stagnate in this region and are convected away by the unsteady entering flow. This is analogous to the delayed transition to turbulence in pulsatile flows.

4.4.3. Comparison between Linked List and Simple Particle Search Methods

The linked list method has been used in all simulation cases as an effective method to search for the neighboring particles at each time step. As shown in Table 4.1, the efficiency of the method increases with increasing the number of particles. For instance, the computation with a number of 101616 fluid particles runs 428 times faster than when the linked list method is not applied, while for a case with 3071 fluid particles the computation runs 26 times faster. This comparison is based on simulation runs on a 1.86 GHz, 2 GB Intel Personal Computer.

Table 4.1. The effect of applying linked list method on decreasing computation time.

Initial Particle Spacing (mm)	Number of Particles	Computation Time per Time Step (s)		Decrease in Computation Time
		Simple Particle Search Method	Linked List Method	
0.83333	Fluid Particles: 3071 Wall Particles: 258 Imaginary Particles: 528	13.2	0.5	$\frac{1}{26}=0.038$
0.38155	Fluid Particles: 14705 Wall Particles: 546 Imaginary Particles: 1104	257.5	2.4	$\frac{1}{107}=0.009$
0.29450	Fluid Particles: 25250 Wall Particles: 708 Imaginary Particles: 1428	746.6	4.5	$\frac{1}{166}=0.006$
0.20833	Fluid Particles: 50506 Wall Particles: 998 Imaginary Particles: 2008	2457	9.7	$\frac{1}{253}=0.004$
0.17241	Fluid Particles: 73848 Wall Particles: 1202 Imaginary Particles: 2416	4880	14.2	$\frac{1}{343}=0.003$
0.14706	Fluid Particles: 101616 Wall Particles: 1410 Imaginary Particles: 2832	8989	21	$\frac{1}{428}=0.002$

4.5. Pulsatile Flow inside a Model of Left Ventricle

A 2D realistic asymmetric model of LV (dimensions of 0.04 (m) by 0.05 (m)) with a pulsatile inlet velocity similar to the rectangular cavity case is shown in Fig. 4.11. The inlet velocity condition is the most applicable type of boundary condition in biofluid

mechanic studies. As the flow experiences high inertial effects only during a short portion of the period and the LV geometry represents a healthy LV, the flow is not turbulent. The assumption of laminar flow is realistic when the LV is under normal conditions.

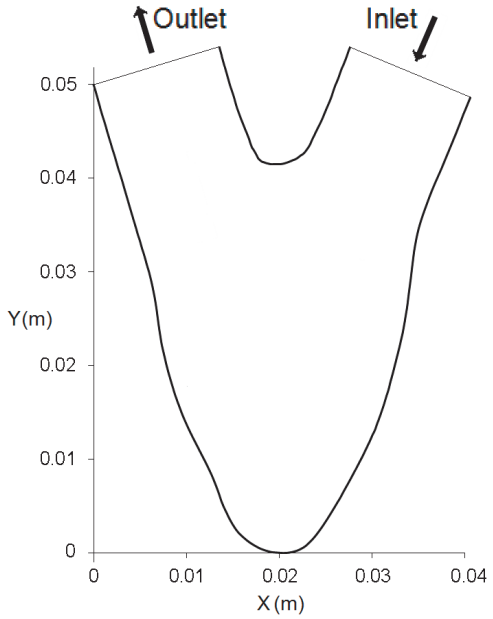

Fig. 4.11. A realistic asymmetric geometry of the LV cavity.

The velocity profiles at different instants at mid-vertical and horizontal cross-sections (lines: $X = 0.0194\ (\mathrm{m})$ and $Y = 0.025\ (\mathrm{m})$) of the LV cavity for different particle resolutions ($dr = 5.555 \times 10^{-4}\ (\mathrm{m}), 3.846 \times 10^{-4}\ (\mathrm{m}), 2.083 \times 10^{-4}\ (\mathrm{m})$) are shown in Fig. 4.12(a-d). These particle resolutions were selected considering both the level of accuracy and the computational costs based on the simulation results for the pulsatile flow inside a rectangular cavity (Sec. 4.4).

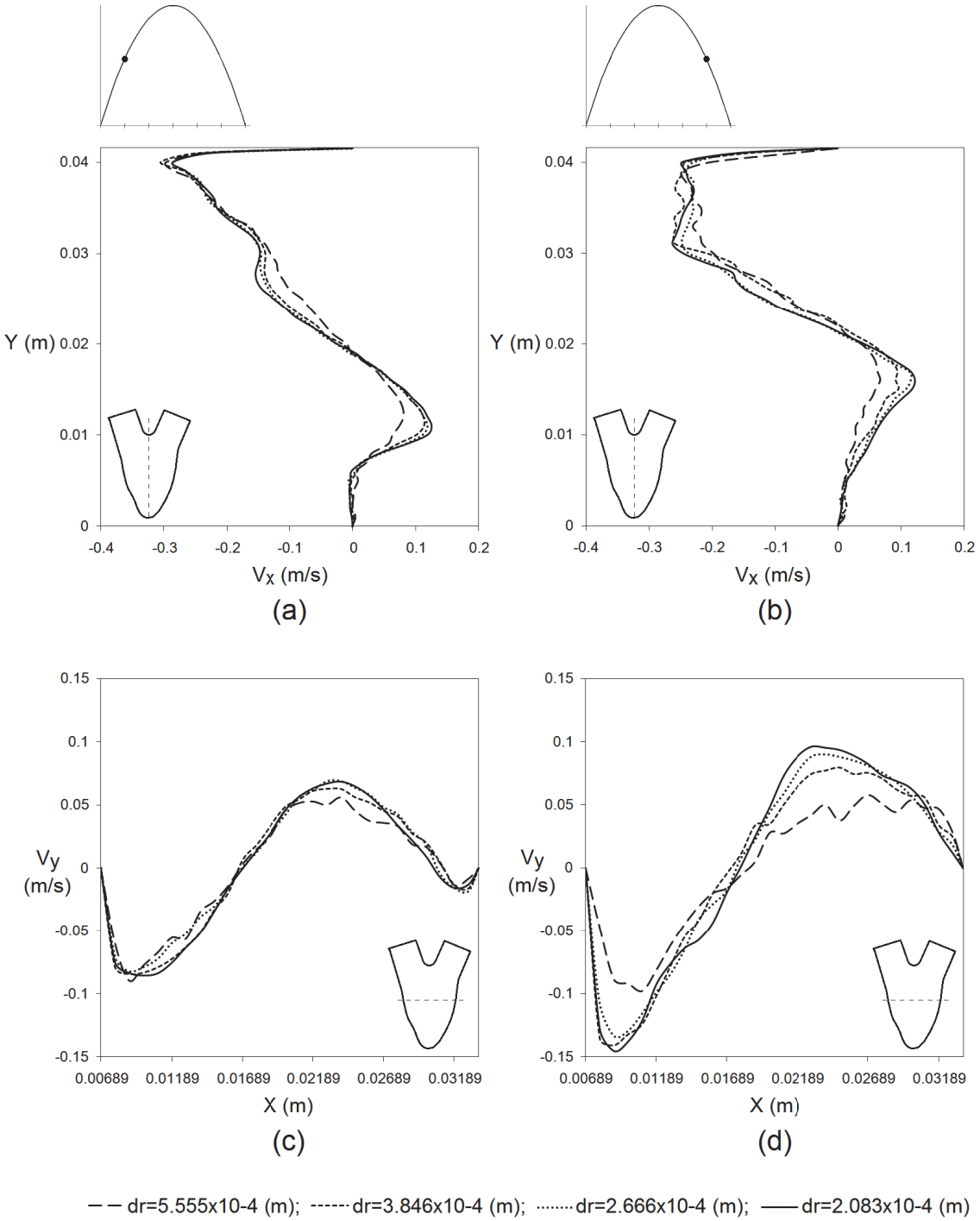

Fig. 4.12. SPH velocity profiles at main cross sections of the LV cavity and the effect of particle resolutions on the profiles; at mid vertical cross section: a) $t = 0.1$ (s), b) $t = 0.5$ (s) of a cycle; and at mid horizontal cross section: c) $t = 0.1$ (s), d) $t = 0.5$ (s) of a cycle.

The velocity profiles demonstrated a convergence of the results. Assuming that the finest resolution represents a converged solution, the convergence evaluated using L_2-relative error norm is shown in Fig. (4.13). For each cross section, the error is defined based on the actual computed velocity profile and the one using a lower particle resolution. It appears that the velocity profiles converge with a rate of convergence which is between first and second order and is consistent with previous results.

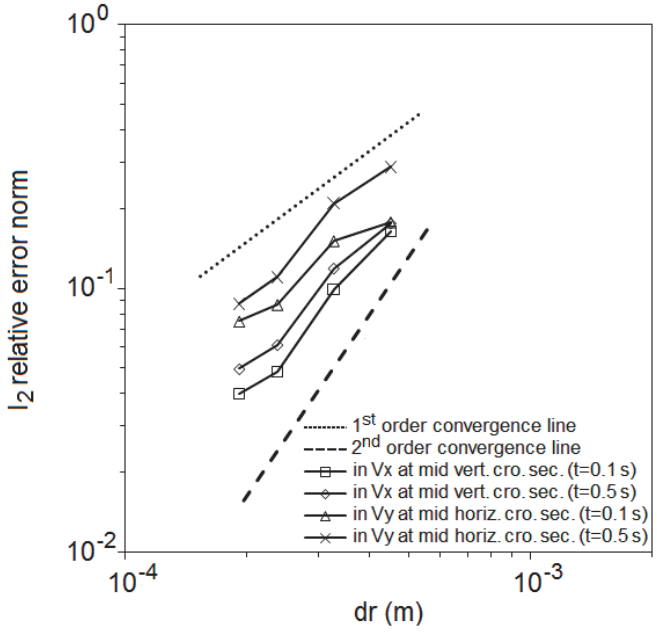

Fig. 4.13. L_2-relative error norm versus spatial resolution for velocity calculations at mid-vertical and mid-horizontal cross sections.

The velocity vector maps for a case with 16429 fluid particles ($dr = 2.666 \times 10^{-4}$ m) at different instants during a cycle ($t = 0.1$ s, 0.2 s, 0.5 s and 0.6 s are shown in Fig. 4.14 (a-d).

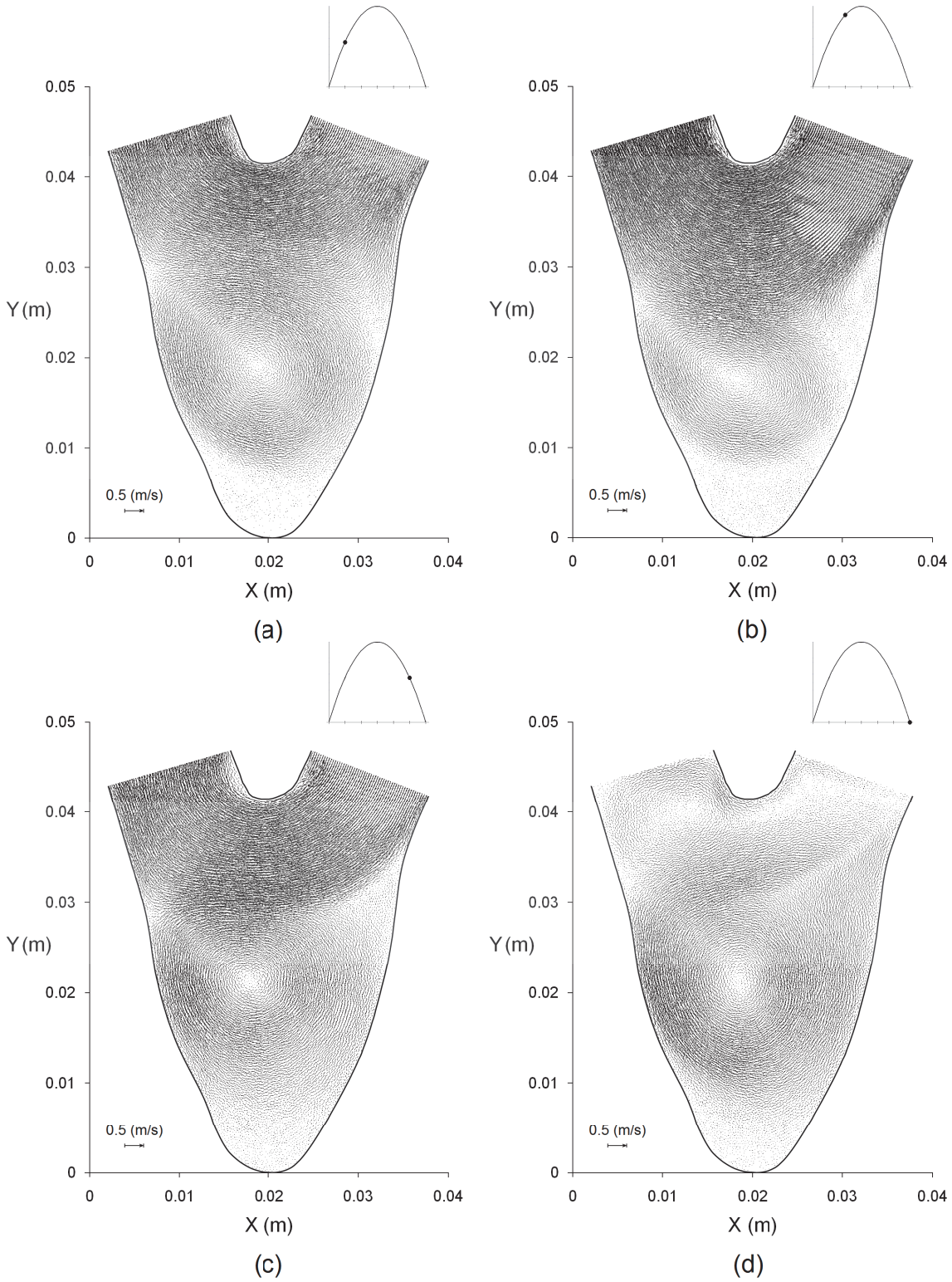

Fig. 4.14. SPH velocity vector maps in the LV cavity; 16429 fluid particles ($dr = 2.666 \times 10^{-4}$ m) at: a) $t = 0.1$ (s); b) $t = 0.2$ (s); c) $t = 0.5$ (s); and d) $t = 0.6$ (s) of a cycle.

The flow displayed a number of complicated characteristics. The acceleration period of the filling phase (Fig. 4.14a,b) is mainly characterized by a pulsatile jet emerging into the cavity. The inlet jet dominates the main vortex remaining from the previous cycle. As a result of jet breakdown during the deceleration period (Fig. 4.14c), the coherent structure grows in the space between the inlet and the outlet. At the end of the cycle (Fig. 4.14d), this coherent structure grows rapidly and occupies the central region in the cavity. These flow characteristics are close to physiological flow characteristics in the human LV where the filling phase is mainly characterized by a pulsatile jet emerging from the left atrium, through the mitral valve, into the LV cavity. During a normal filling phase, this jet flow strikes the apex of LV and then turns back up towards the septal wall resulting in a large asymmetric vortex that effectively fills the entire LV, with velocities directed towards the LV outflow tract (Rodevand et al, 1999). The role of this vortex is to store some kinetic energy during the filling (diastolic) phase and release it during the ejection (systolic) phase (Pedrizzetti and Domenichini, 2005).

The results obtained here are promising, since this work represents a first attempt to simulate the flow inside a model of LV using a meshfree particle method. The anatomy of the LV is simplified (no boundary movement), and as a consequence, to satisfy the conservation of mass in the domain, the outlet remains in the open position. Therefore, in present simulations during the acceleration phase, the flow at the inlet is immediately directed towards the aortic side (outlet). The main features of the flow, however, are similar to what is reported in clinical papers in terms of emerging inlet jet and main vortex in the LV (Kilner et al., 2000). Conducting simulations with a moving boundary represents the next logical development.

An important characteristic of SPH that makes it suitable for the simulation of cardiovascular flows is its ability to directly determine the time history of the fluid elements in the domain. In Fig. (4.15), the time history of four particles entering the domain has been studied. This allows the determination of the residual time under pathological conditions allowing for a link with the risk of LV thrombosis to be developed.

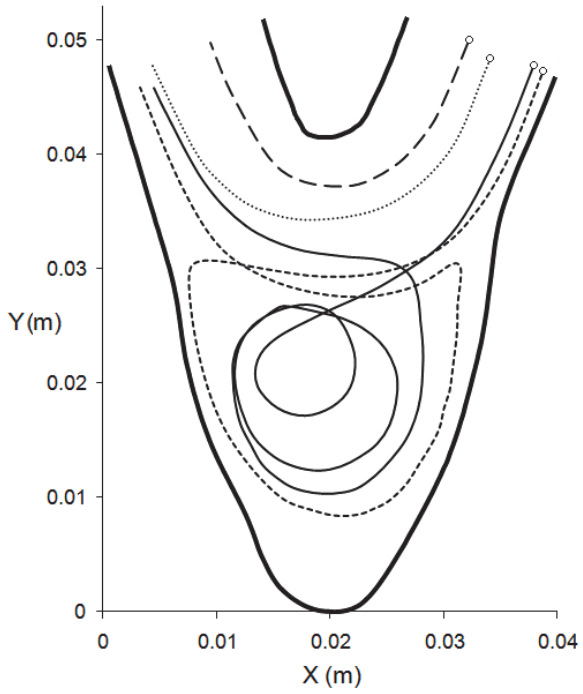

Fig. 4.15. Time history of entering particles.

4.6. Summary

The study aimed to further develop SPH to simulate flow inside a model of the LV. The relevant validations were provided in Chapter 3 and this chapter using a series of benchmark cases including, unsteady oscillating and lid-driven cavity flows. Subsequently, both benchmark cases were combined and a pulsatile jet in a cavity was

simulated. The results of the simulation were compared with the finite volume method. In addition, an approach to incorporate inflow and outflow boundary conditions was introduced. Finally, pulsatile inlet flow in a rigid LV model was simulated. The results demonstrated the ability of SPH to model complex flows and to track the time history of fluid properties. This chapter also highlighted some interesting characteristics of the SPH method. The order of accuracy in SPH simulations is still a controversial issue and its determination is not as straightforward as for mesh-based methods. The SPH formulation should lead to a second order accuracy, but it was shown that particle resolution plays an important role in the order of the accuracy. Low particle resolution can be sufficient to analyze the general behavior of the flow and to be applied to engineering problems. Also, the Lagrangian nature of SPH permits tracking the history of fluid shear stress with application to blood hemolysis analysis of cardiovascular devices.

Chapter 5

Blood Components Damage in Bileaflet Mechanical Heart Valves

Shear induced damage to blood components occurs due to unphysiological flow patterns and is of primary importance in the design of prosthetic cardiac devices. This chapter presents the first SPH simulation of the complex hemodynamics of bileaflet mechanical heart valves (BMHVs) with emphasis on the determination of shear stress loading history on blood components. One of the main characteristics of SPH, discussed in the previous chapter, is its ability to determine the realistic time history of the fluid elements in the domain. This study illustrates the effects of unphysiological shear stress patterns and vortical structures on the potential number of blood components damaged.

5.1. Introduction

Valve replacement by a prosthetic heart valve is the only viable solution in symptomatic patients with severe valve stenosis. The prosthetic heart valve can be either biological or mechanical. Due to the elevated structural durability of mechanical heart valves (MHVs) compared to biological heart valves, 2/3 of all valve replacements are performed using MHVs. Several *in vivo, in vitro* and *in silico* studies have been dedicated to the investigation of flow characteristics downstream of MHVs. A review on these

studies, the current challenges and future directions can be found in (Yoganathan et al., 2005; Sotiropoulos and Borazjani, 2009).

Despite decades of improvements in the design of MHVs, thrombus formation and hemolysis are still the major drawbacks associated with MHVs. *In vivo* evaluation of such shear induced hemodynamic events is still a difficult task. As a consequence, most studies rely on *in vitro* tests and numerical simulations, with a preference towards numerical simulations as they provide a large spectrum of flow characteristics with a significantly high spatial resolution.

Commercial and in house computational codes have studied MHVs in a wide range of applications ranging from simplified geometry, symmetrical assumptions, steady flow and laminar regimes to detailed geometrical models, applied pulsatile velocity waveforms, turbulence modeling and fluid structure interaction (King et al., 1996; Ge et al., 2003; Cheng et al., 2004; Redaelli et al., 2004; Dumont et al., 2007; Nobili et al., 2008; de Tullio et al., 2009). These methods demonstrated good capability in simulating the hemodynamics of MHVs.

Almost all studies investigating thrombus and hemolysis events in MHVs rely on simulations based on an Eulerian approach. However, an accurate evaluation of such events has to take into account the loading history and the cumulative effect on blood components (Grigioni et al., 2005). This requires using a Lagrangian integral of the fluid over time (Moiseyev and Bar-Yoseph, 2010) and therefore, to analyze the Lagrangian dynamics of blood components trajectories in the unsteady flow field (Yoganathan et al., 2005). This can more accurately be performed using meshfree particle Lagrangian methods.

One of the first contributions dedicated to the application of particle methods to simulate blood flow through MHVs was performed using the Lattice Boltzmann method (LBM) (Krafczyk et al., 1998; Krafczyk et al., 2001; Pelliccioni et al., 2007). The LBM method is based on statistical and probabilistic physics and requires collision sub-processes to simulate the physical interaction between the particles. The simulations were capable of capturing the main flow characteristics downstream of bileaflet MHVs (BMHVs) and the results were very promising. The algorithm and the methodology are still under improvement, much like all other particle methods. The LBM method is not a fully meshfree Lagrangian method since it still requires a background mesh for particle distribution. This, similar to Eulerian based methods, may limit its accuracy for the evaluation of shear induced hemodynamic events.

The study presented in this chapter is dedicated to study blood flow through a BMHV using SPH. This study first demonstrates the potential of the SPH method to simulate the complex flow through a BMHV. Then, the risk of shear stress hemodynamic events (thrombus formation and hemolysis) induced by a BMHV is evaluated without employing a fictitious particle injection and tracking techniques. The simulations are performed for both normally functioning and dysfunctional BMHVs.

5.2. Methodology and Formulations

The Navier-Stokes equations can be discretized, using SPH, in different forms (Chapter 2). The continuity and Reynolds averaged Navier-Stokes (RANS) momentum equations for turbulent flows are adopted based on Eqs. (2.8), (2.12), and (2.21) as

$$\frac{d\rho_a}{dt} = \sum_b m_b \boldsymbol{V}_{ab} . \boldsymbol{\nabla}_a W_{ab} \tag{5.1}$$

$$\frac{d\boldsymbol{V}_a}{dt} = -\sum_b m_b\left(\frac{P_b+P_a}{\rho_a\rho_b}\right)\boldsymbol{\nabla}_a W_{ab} + \sum_b m_b \frac{(\mu_{e,a}+\mu_{e,b})\boldsymbol{r}_{ab}.\boldsymbol{\nabla}_a W_{ab}}{\rho_a\rho_b(\boldsymbol{r}_{ab}^2+\eta^2)}\boldsymbol{V}_{ab} \quad (5.2)$$

where $\boldsymbol{V}_{ab} = \boldsymbol{V}_a - \boldsymbol{V}_b$ is the relative velocity vector between particles a and b, P is pressure, μ_e is effective viscosity defined as $\mu_e = \mu + \rho\nu_T$, where μ is dynamic viscosity and ν_T is turbulent eddy viscosity and η^2 is a small term to avoid the singularity. The equations presented here are based on the turbulent mean flow and the traditional symbol representing time-averaged variables is omitted for simplicity. Turbulence modeling in SPH has been more applied to free surface flow simulations (Shao and Gotoh, 2004, Ting et al., 2005; Dalrymple and Rogers, 2006; Violeau and Issa, 2007). The effect of turbulent fluctuations on the mean flow through BMHV is modeled using $k - l_m$ turbulence model (Wilcox, 2006; Violeau and Issa, 2007). A detailed description of the adopted turbulent model is presented in section 2.2.6. This model is less computationally demanding, while it is able to answer the demands of this study.

The pressure is related to the density by the equation of state shown in Eq. (2.14). The standard formulation of Eq. (2.28) is used to track the movement of the particles in the domain and a variable computational time step is employed based on Eq. (2.34). The time integration of the governing equations is based on a predictor-corrector scheme.

The effect of wall boundaries is modeled by placing a layer of particles on the walls and three layers of imaginary particles outside of the fluid domain parallel to the walls (see Sec. 3.3.6). A zero velocity is given to wall particles but an extrapolated velocity is given to the imaginary particles to force no slip boundary condition on the walls and avoid fluid particles penetrating the walls.

5.3. Numerical Model

A pulsatile flow through a two dimensional model of St. Jude Medical bileaflet aortic heart valve prostheses is simulated using SPH. The model is identical to the one used by Bluestein et al., 2000. The inlet velocity waveform, corresponding to cardiac output of $5.5\ (\mathrm{L/min})$ and heart rate of $72\ (\mathrm{bpm})$, used in this study are shown in Fig. 5.1. The density and dynamic viscosity of blood is set to $1056\ (\mathrm{kg/m^3})$ and $3.5 \times 10^{-3}\ (\mathrm{Pa.s})$, respectively. A fully developed turbulent velocity profile is applied at the inlet (Munson et al., 2005).

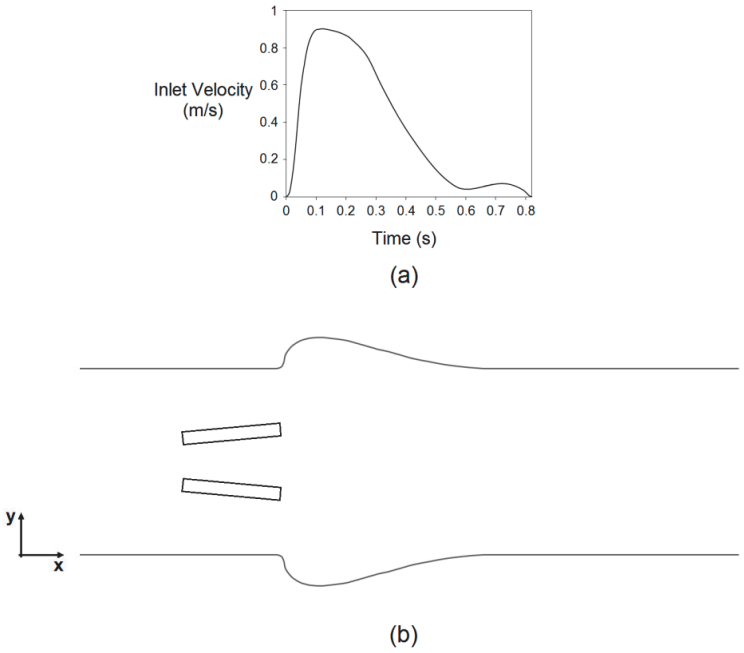

Fig. 5.1. Features of the model used in this study: a) Inlet velocity wave form, and (b) normal bileaflet mechanical heart valve geometry.

Pannus or thrombus formation around the BMHV structure can lead to valve dysfunction in one or both leaflets (Baumgartner et al., 1993). The prevalence of such a life-threatening complication is around 0.2 to 6% patients/year (Montorsi et al. 2003). In

this study, a normal functioning and a dysfunctional BMHV with different dysfunction severities in one leaflet (from 25% to 100% in area) are simulated using approximately 19700 particles to depict the continuum fluid domain, 524 particles to model the walls and 328 particles to model the valve leaflets.

5.4. Flow Patterns

Figure 5.2 shows the comparison between the results for axial velocity at the leading edge and the trailing edge of the BMHV leaflets during the systolic deceleration phase (105 (ms) after peak of systolic phase), obtained using SPH and FV method (Bluestein et al., 2000). There is very good agreement between the results.

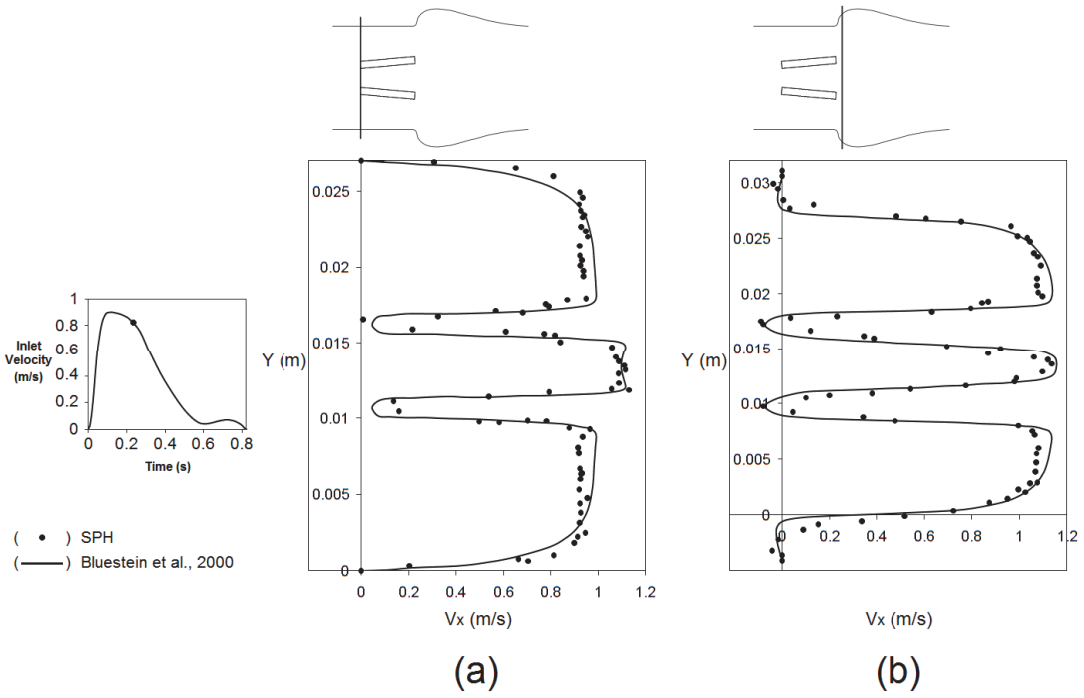

Fig. 5.2. Comparison between SPH results and finite volume method results (Bluestein et al., 2000) for axial velocity profiles at two cross-sections at 105 (ms) after peak systole: (a) at the leading edge of valve leaflets; (b) at the trailing edge of valve leaflets.

The SPH simulations were capable of capturing the main features of the flow through the BMHV including, central and lateral jets and vortex shedding in the wake of the leaflets as shown in Fig. 5.3(a). The maximal velocity is 1.89 (m/s). In the figure, two instants are considered: peak systolic phase and deceleration phase.

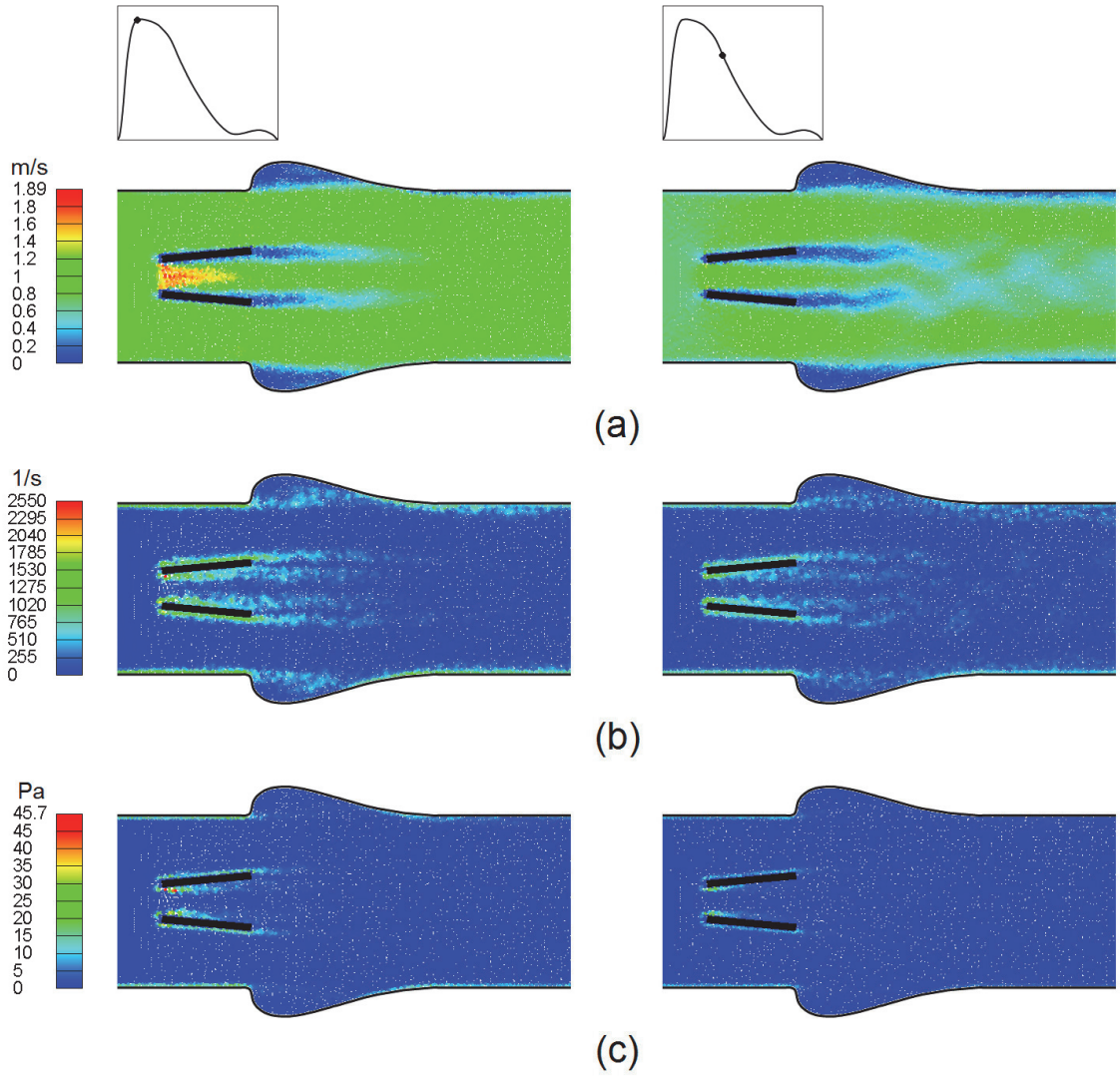

Fig. 5.3. Flow patterns through a normal BMHV at peak systole (0.1 s) and early deceleration phase (0.3 s): (a) velocity magnitude; (b) vorticity; and (c) turbulent shear stress.

Figure 5.3(b) depicts the vorticity field at the same instants. The shear layer around the leaflets rapidly separates into unsteady vortices downstream of the valve. As a consequence of such flow configuration, SPH particles experience a turbulent shear stress that can reach up to 45.7 (Pa) (Fig. 5.3c). This value is close to the value (53 Pa) obtained experimentally by (Liu et al., 2000).

The consequence of one valve leaflet dysfunction on velocity, vorticity and turbulent shear stress is shown in Fig. 5.4. An opening of one leaflet of the BMHV up to 50° instead of 85° (for St-Jude HP BMHV), corresponding to 76% severity in leaflet dysfunction, leads to a significant increase in the maximal velocity reaching up to 3.52 (m/s). Furthermore, the maximal velocity is not located through the central orifice anymore, as expected in the healthy case, but through the lateral normally functioning orifice. This has a significant *in vivo* practical consequence, since in the evaluation of the performance of BMHVs by Doppler echocardiography, the ultrasound beam is aligned with the central orifice. Under such conditions, the velocity recorded will be 2.2 (m/s) instead of 3.52 (m/s), representing an underestimation of the maximal velocity by 60%. These values are in agreement with the experimental study of (Baumgartner et al., 1993) and the numerical simulations of (Smadi et al., 2010).

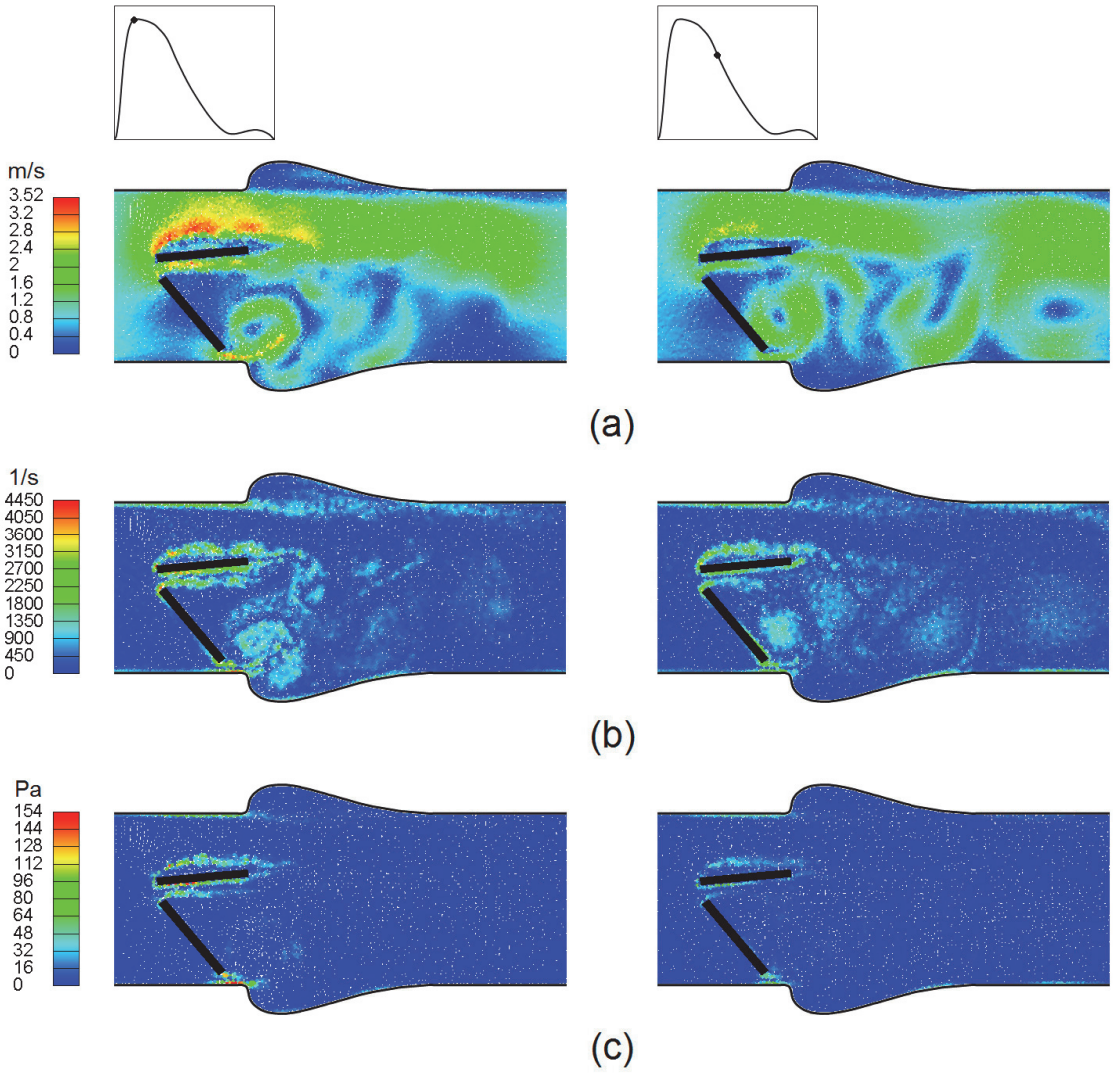

Fig. 5.4. Flow patterns through a dysfunctional BMHV at peak systole (0.1 s) and early deceleration phase (0.3 s): (a) velocity magnitude; (b) vorticity; and (c) turbulent shear stress.

The vorticity field downstream of the dysfunctional mechanical heart valve shows the development of large coherent structures mainly downstream of the dysfunctional leaflet (Fig.5.4b). This new flow configuration has a direct impact on the magnitude of turbulent shear stress within the flow field (Fig. 5.4c). Indeed, the value of maximum turbulent shear stress in the presence of a dysfunctional BMHV is more than three times higher than when the BMHV functions normally (154 (Pa) *vs.* 45.7 (Pa)).

5.5. Shear Stress Accumulation on Particles

The Lagrangian nature of the SPH method gives direct access to the shear stress history imposed on blood components. As the flow in SPH is modeled by real fluid particles, there is no need to consider a complex particulate two phase flow approach or injection of particles and stochastic models to investigate the effect of turbulence on particle trajectories (Bluestein et al., 2000; Dumont et al., 2007; Govindarajan et al., 2009). Also, there is no need to adopt virtual particle integration (VPI) method proposed recently by (Moiseyev et al., 2010) to overcome disadvantages inherent to particle injection and tracking techniques.

The concept initially developed by (Hellums et al., 1987), to quantify the shear stress history of platelets flowing through a stenosis (Bluestein et al., 1997) is used to compute the shear stress loading of blood elements. It was then used by (Bluestein et al., 2000) to study the thromboembolic complications in MHVs. The cumulative effect of instantaneous turbulent shear stress, τ, and exposure time, dt, on each blood component, a, in the domain is computed as $\sum|\tau_a|.dt$.

The accumulative shear stress pattern supported by SPH particles is shown in Fig. (5.5). A dysfunctional BMHV has significantly more potential to damage blood components than a normally functioning valve. This is mainly due to the combination of elevated turbulent shear stresses and larger coherent structures, mainly downstream of the dysfunctional leaflet, trapping the particles in the large flow recirculation regions.

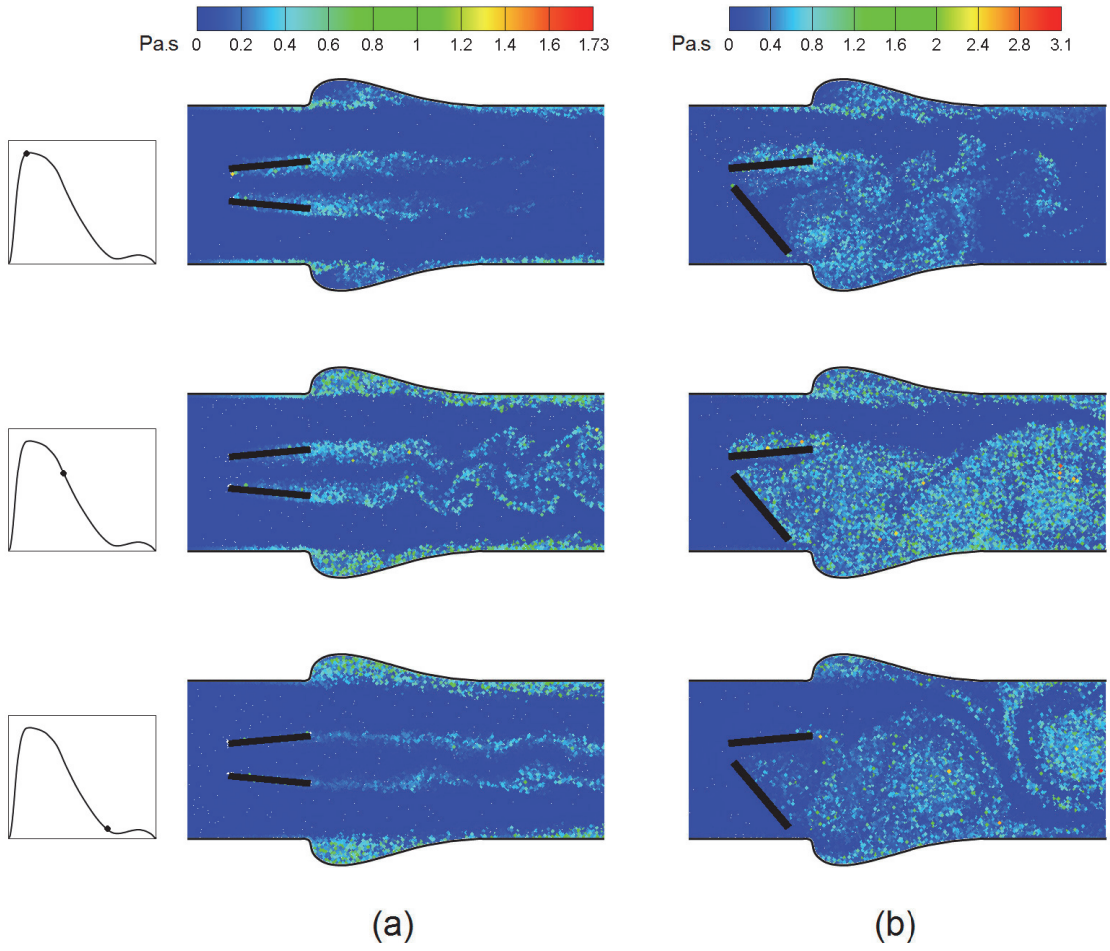

Fig. 5.5. Instantaneous patterns associated with accumulative shear stress applied on particles passing through: (a) normal bileaflet mechanical heart valve; and (b) dysfunctional bileaflet mechanical heart valve.

Blood particles passing through the leading edge of the leaflets are exposed to high turbulence shear stress (Figs. 5.3c and 5.4c) which may trigger damage to the blood components. Particle shear stresses are lower in the deceleration phase, but more complex patterns trap fluid particles in the domain for a longer period and increase accumulation of shear stresses. The accumulative shear stress field is analogous to the vorticity field in terms of flow patterns (Figs. 5.3b and 5.4b). This shows the potential role played by unphysiological vortices in damaging blood components.

Figure 5.6 shows a histogram of the accumulative shear stress loading on particles at 0.3 s of the cardiac cycle in the entire domain. The results for the normally functioning valve are compared to those obtained for the dysfunctional valve (for 25%, 42%, 60%, 76% and 100% reduction in area).

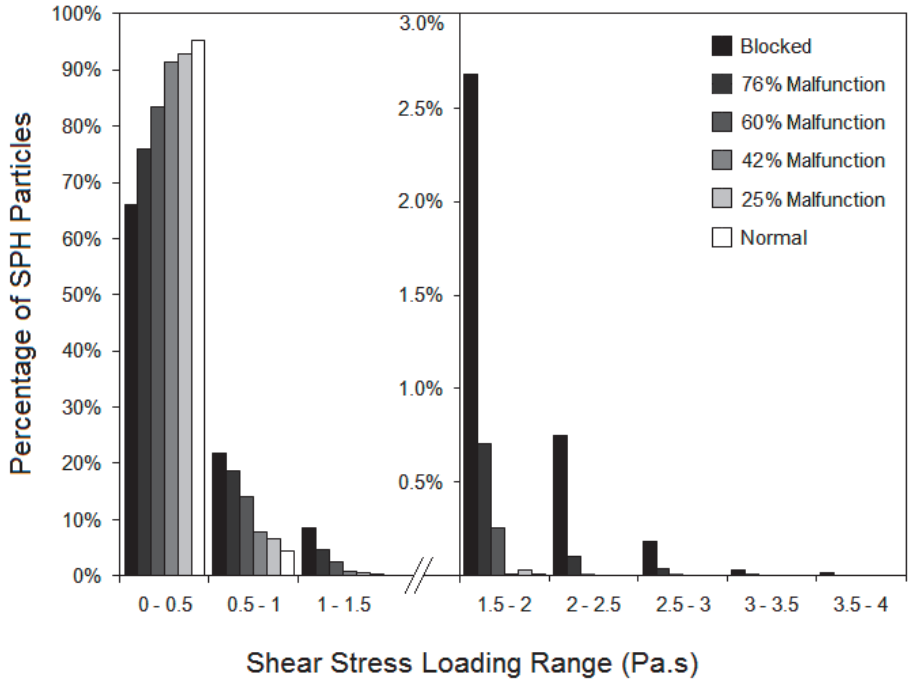

Fig. 5.6. Statistical distribution of particle accumulative shear stress loading at 0.3 (s) of the cardiac cycle.

The SPH particles moving through a dysfunctional BMHV carry higher stress accumulation, which illustrates the high potential of even a mild dysfunction to damage blood components. The resulting thrombus can contribute rapidly to increase the severity of valve dysfunction. Different threshold levels are reported for shear stress damage to platelets (Hellums et al., 1987) and red blood cells (Lu et al., 2001). Red blood cells tolerate much higher shear stress than platelets. In a normal BMHV 95 % of particles

have an accumulative shear stress less than $0.5\ (\mathrm{Pa.s})$ $(5\ \mathrm{dyne.s/cm^2})$, however in a case with one completely blocked leaflet, $66\ \%$ of particles tolerate the same range of shear stress accumulation. In a healthy case, no particle tolerates an accumulative shear stress higher than $2\ (\mathrm{Pa.s})$. Higher degrees of valve dysfunction result in a larger number of particles with elevated shear stress loading.

5.6. Summary

The SPH methodology was further developed to simulate flow through normal and dysfunctional BMHVs with a realistic aortic flow waveform. The results showed the capability of SPH to simulate the complex flow through prosthetic mechanical heart valves. As this work represents the first attempt to apply SPH to simulate the complex pulsatile flow through a normal and dysfunctional bileaflet mechanical heart valve, some simplifications had to be adopted. Mainly, two dimensional simulations and fixed valve leaflets.

Evaluating shear-induced hemodynamic events is of primary importance for the design of mechanical heart valves. Currently, this relies on numerical simulations based on an Eulerian approach. However, a more accurate evaluation should be based on the analysis of the Lagrangian dynamics of blood components. The results obtained regarding the accumulation of shear stress patterns on blood components illustrates the important role played by unphysiological flow patterns and mainly vortical structures. The statistical distribution of particles with respect to shear stress loading history provides important information regarding the relative number of blood components that

can be damaged. This can be used as a measure of the response of blood components to the presence of the valve implant or any implantable medical device.

Finally, it should be mentioned that implementation of FSI can result in higher levels of blood components damage due to the interaction between valve leaflets and blood elements mainly during closing and regurgitation phases.

Conclusions and Future Works

This thesis aimed to develop smoothed particle hydrodynamics (SPH), a fully Lagrangian meshfree method, to study blood flow in the cardiovascular system. The SPH method demonstrated good reliability to simulate hemodynamics in the heart and arteries. It also demonstrated the capability of modeling a number of flow characteristics that are difficult to capture using mesh-based methods. Moreover, some interesting features of SPH methodology were discovered and highlighted through a series of numerical tests.

The performance of the two most commonly standard formulations for modeling the viscous term, the XSPH variant and symmetric formulation for pressure gradient modeling was investigated. The standard *"Form II"* for modeling the viscous term showed more accuracy, and unlike *"Form I"*, it was not dependent on the type of interpolating kernel function and flow characteristics. Using XSPH variant to modify the movement of the particles created undesirable particle disorders. Based on this study, it is recommended that XSPH be used with caution in the presence of the real viscosity. The symmetric form for pressure gradient provided accurate results and did not show sensitivity to the selected value for sound speed. It was shown that the particle resolution plays an important role in the order of the accuracy in SPH simulations and the velocity profiles converge with a rate of convergence that is between first and second orders. To search the neighboring particles, the linked list method was used in all simulations. The method resulted in a decrease in the computational cost on the order of several hundred times for simulations with high particle resolution compared to the simple search method.

A modified formulation for wall shear stress calculations was introduced and verified against exact solutions. Simulation of a lid-driven cavity flow at laminar high Reynolds numbers showed that increasing particle resolution can prevent compressibility effects in SPH while maintaining the speed of sound at a reasonable range. An effective approach to handle the challenges of simulating inflow and outflow boundary conditions was provided and tested. The SPH method was able to correctly simulate internal oscillating flows even in the presence of a large phase lag between the oscillation of the applied pressure difference and the moving boundary with the derived velocity.

Smoothed particle hydrodynamics method was applied successfully to simulate pulsatile flow inside a model of the left ventricle (LV). The method showed good capability as an effective substitute for conventional mesh-based methods to simulate complex hemodynamics of the LV while easily tracking the history of fluid elements in the domain. Understanding the performance of LV filling is not only important from a clinical point of view, but also for the development of the cardiovascular assist devices. The results obtained here are promising as this work represents the first attempt to simulate the flow inside a model of the LV using a meshfree particle method. The main features of the simulated flow are similar to what is reported in clinical papers in terms of emerging inlet jet and main vortex in the LV.

Smoothed particle hydrodynamics was also successfully applied to simulate flow through normal and dysfunctional BMHVs with a realistic aortic flow waveform. The results showed the capability of SPH to simulate the complex flow through BMHVs including lateral and central jets, vortex shedding downstream of the valve leaflets and large recirculation regions downstream of the dysfunctional leaflet. In this study, the

effect of turbulent fluctuations on the mean flow through BMHVs was also considered. The results obtained regarding the accumulation of shear stress patterns on blood components illustrates the important role played by non-physiological flow patterns and mainly vortical structures. The cumulative shear stress patterns provided in this study are clearly similar to the vorticity patterns, which clearly demonstrates the role of vortices in the accumulation of shear stress on blood particles. The elevated potential to damage blood components starts when particles bear high shear stress, especially near the leaflets. For a healthy valve, particles passing near the leaflets spin downstream of the leaflets. In a dysfunctional MHV, particle motion presents a complex vortical nature with a large recirculation downstream of the dysfunctional leaflet, which affects a larger number of blood components and traps them.

All simulated cases in this thesis did not show unacceptable compressibility effects. This is despite the fact that in some cases, fluid particles experienced rapid changes in acceleration magnitude and direction, and were subjected to higher inertial effects when compared to previous studies. As this thesis represents the first essential attempt to apply SPH in the simulation of complex pulsatile flow inside a LV cavity and through BMHVs, some simplifications had to be adopted which are described below.

The anatomy of the LV was simplified (no boundary movement), and as a consequence, to satisfy the conservation of mass in the domain, the outlet remained in the open position. In the future, conducting simulations with a moving boundary represents the next logical development. The meshfree nature of SPH allows implementation of the moving boundaries with less difficulty than in mesh-based methods. The complexity of

the geometries and movement of the boundaries leads to elevated computational costs in mesh-based methods because of the process of mesh generation and re-meshing.

Using *in vivo* phase-contrast magnetic resonance imaging (MRI), it is possible to acquire patient specific myocardium movements. In the future, a combined MRI and SPH study can provide reproduction of flow patterns in the patient's LV. The meshfree particle nature of SPH will allow easy testing, *in silico*, of alternative surgical procedures and to estimate their clinical impact on the hemodynamic condition of the patient. The two-dimensional simulation is not an important limitation since most of the imaging instruments used by clinicians derive two velocity components.

The main assumption adopted in modeling the hemodynamics of BMHVs was fixed valve leaflets. It should be mentioned that considering the movement of the leaflets in the future can result in higher levels of blood components damage due to the interaction between valve leaflets and blood elements, mainly during closing and regurgitation phases. The proposed technique, based on SPH for evaluating the shear stress loading of particles, can also be used to measure the response of blood components in the presence of valve implants or any implantable medical device. The turbulent model used in this study can predict the flow behavior at an acceptable level of accuracy for the purpose of this study, while having low computational cost. The complexity and unsteadiness of the flow through a BMHV may require employing a more advanced turbulence model demanding high performance computing facilities. Running the code in parallel CPUs or executing on graphics processing units (GPUs) can overcome this limitation and speed up the calculations enormously.

Another perspective for future work is to integrate simulations based on SPH and ultrasound to evaluate the potential of the emerging techniques for imaging arterial hemodynamics and wall movement. Newly developed ultrasonic measurement techniques such as Echo particle image velocimetry (EchoPIV), have shown experimentally to be a promising tool capable of well estimating blood velocity as well as wall artery motion in complex geometries. However, prior to a wider clinical application, Echo PIV has to be thoroughly validated. Currently, the validation strategy is mainly based on coupling mesh-based computational methods with ultrasound simulations using random point scatters. Random virtual point scatters are used and their dynamic displacement resembles movement of the blood components and wall arteries. At each time step, the velocity vector of the scatters can be derived using a complex mapping approach between Lagrangian and Euleran frames. Using SPH, both fluid and structure domains are solved through the same algorithm. Furthermore, SPH particles can act as point scatters and there is no need to consider random virtual point scatters and use complex and low-accuracy techniques to track their movement in the domain. Therefore, the coupling fluid-solid-ultrasonic simulations will be more realistic. Smoothed particle hydrodynamics can provide an accurate reference for verification of ultrasound derived velocity fields.

Appendix A

Computational Algorithm

The algorithm for second order accurate predictor-corrector time integration scheme in SPH is described below. The differential equations have a general form as $\frac{dy}{dt} = f$. The algorithm was implemented using the programming language FORTRAN.

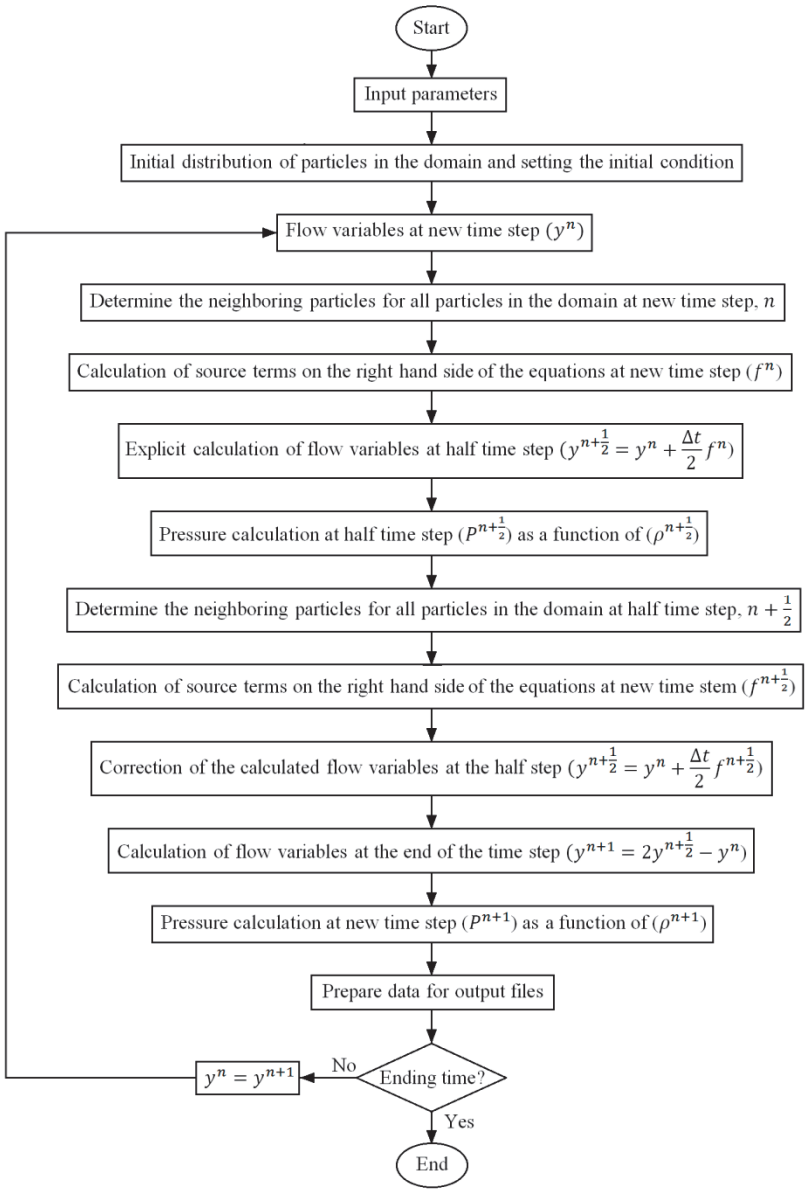

Fig. A.1. General algorithm for SPH calculations based on predictor-corrector time integration scheme.

Appendix B

SPH Code for Linked List Method

A fast method to search for neighboring particles is to employ a linked list method. The following code describes how to determine how many and which particles are positioned in a specific cell in the domain.

```
!       At each time step (n), this part of the code determines the cell number that each particle (i) is
!       allocated to and returns cell number (ICellNx, ICellNy) for each particle and the number of
!       particles in each cell (NPC).

        DO 5 ic=1,NCellx        !       NCellx: Number of cells in x-direction.
        DO 5 jc=1,NCelly        !       NCelly: Number of cells in y-direction.

        NPC(ic,jc)=0            !       NPC(ic,jc): Number of particles in cell number (ic,jc).

5       CONTINUE

        DO 10 i=1,Ntot                  !       Ntot: Total number of particles.

!       Kernel with supporting size of 2.5*h.
        ICellNx(i)=INT(X(i,n)/(2.5*h))  !       ICellNx(i): x indicator of cell number that
                                                particle (i) is allocated to.
        ICellNy(i)=INT(Y(i,n)/(2.5*h))  !       ICellNy(i): y indicator of cell number that
                                                particle (i) is allocated to.
        INx=ICellNx(i)
        INy=ICellNy(i)

        NPC(INx,INy)=NPC(INx,INy)+1

        Cell(INx,INy,NPC(INx,INy))=i
!       The NPC^th component of the cell number (ICellNx, ICellNy) is particle (i)

10      CONTINUE
```

After all particles were assigned to the cells, the summation process is started to compute the right hand side of the equations in SPH approximation. For particle of interest, *a*, located at the cell number (ICellNx(na), ICellNy(na)), only the particles in the same cell and in the neighboring cells are considered. The computational loop over the particles in the domain is shown in the following.

```
      DO 100 na=1,Ntot

      DO 200 nc=-1,1,1
      DO 200 mc=-1,1,1

      CellX=ICellNx(na)+nc

      CellY=ICellNy(na)+mc

      DO 300 ij=1,NPC(CellX,CellY)        !  NPC: Number of particles in cell number
                                             (CellX,CellY)
      nb=Cell(CellX,CellY,ij)             !  nb: Particle number that is the ij th component
                                             of the cell (CellX,CellY)
      Xnanb=X(na,n)-X(nb,n)
      Ynanb=Y(na,n)-Y(nb,n)

      Rab=DSQRT(Xnanb**2+Ynanb**2)        !  Rab: Distance between particle a and
                                             particle b
      q=Rab/h

!     Kernel with supporting size of 2.5*h.
      IF(q.GT.2.5) GOTO 300
      .
      .
      .
      .
      .
```

References

Anderson, J., 1995. Computational fluid dynamics: the basics with applications. 1st edition, McGraw-Hill Science Engineering, Blacklick, Ohio, USA.

Antoci, C., Gallati, M., Sibilla, S., 2007. Numerical simulation of fluid-structure interaction by SPH. Computers and Structures 85, 879-890.

Baccani, B., Domenichini, F., Pedrizzetti, G., Tonti, G., 2001. Fluid dynamics of the left ventricular filling in dilated cardiomyopathy. Journal of Biomechanics 35, 665-671.

Balsara, D.S., 1995. Von Neumann stability analysis of smoothed particle hydrodynamics-suggestions for optimal algorithms. Journal of Computational Physics 121, 357-372.

Basa, M., Quinlan, N.J., Lastiwka, M., 2009. Robustness and accuracy of SPH formulations for viscous flow. International Journal for Numerical Methods in Fluids 60, 1127-1148.

Bate, M.R., 1995. Modelling accretion in protobinary systems. Monthly Notices of the Royal Astronomical Society 277, 362-376.

Baumgartner, H., Schima, H., Kuhn, P., 1993. Effect of prosthetic valve malfunction on the Doppler-catheter gradient relation for bileaflet aortic valve prostheses. Circulation 87, 1320-1327.

Belytschko, T., Lu, Y.Y., Gu, L., 1994. Element-free Galerkin methods. International Journal for Numerical Methods in Engineering 37, 229-256.

Benz, W., Asphaug, E., 1995. Simulations of brittle solids using smoothed particle hydrodynamics. Computer Physics Communications 87, 253-265.

Bernal, J.D., 1964. The Bakerian lecture, 1962: the structure of liquids. Proceedings of the Royal Society London 280, 299-322.

Binder, K, 1992. The Monte Carlo method in condensed matter physics. Springer, Berlin, Germany.

Bluestein, D., Niu, L., Schoephoerster, R.T., Dewanjee, M.K., 1997. Fluid mechanics of arterial stenosis: relationship to the development of mural thrombus. Annals of Biomedical Engineering 25, 344-356.

Bluestein, D., Rambod, E., Gharib, M., 2000. Vortex shedding as a mechanism for free emboli formation in mechanical heart valves. Journal of Biomechanical Engineering 122, 125-134.

Bonet, J., Kulasegaram, S., 2000. Correction and stabilization of smooth particle hydrodynamics methods with applications in metal forming simulations. International Journal for Numerical Methods in Engineering 47, 1189-1214.

Bonet, J., Lok, T.-S.L., 1999. Variational and momentum preservation aspects of smooth particle hydrodynamic formulations. Computer Methods in Applied Mechanics and Engineering 180, 97-115.

Brackbill, J.U., Ruppel, H.M., 1986. FLIP: A method for adaptively zoned, particle-in-cell calculations of fluid flows in two dimensions. Journal of Computational Physics 65, 314.

Chen, S., Doolen, G.D., 1998. Lattice Boltzmann method for fluid flows. Annual Review of Fluid Mechanics 30, 329-364.

Cheng, R., Lai, Y., Chandran, K., 2004. Three-dimensional fluid-structure interaction simulation of bileaflet mechanical heart valve flow dynamics. Annals of Biomedical Engineering 32, 1471-1483.

Cheng, Y., Oertel, H., Schenkel, T., 2005. Fluid structure coupled CFD simulation of the left ventricular flow during filling phase. Annals of Biomedical Engineering 33 (5), 567-576.

Chorin, A. J., 1968. Numerical solution of the Navier-Stokes equations. Mathematics of Computation 22, 745-762.

Cleary, P.W., 1998. Modelling confined multi-material heat and mass flows using SPH. Applied Mathematical Modelling 22, 981-993.

Cleary, P.W., Ha, J., Alguine, V., Nguyen, T., 2002. Flow modeling in casting processes. Applied Mathematical Modelling 26, 171-190.

Colagrossi, A., Landrini, M., 2003. Numerical simulation of interfacial flume by smoothed particle hydrodynamics. Journal of Computational Physics 191, 448-475.

Cummins, S.J., Rudman, M., 1999. An SPH projection method. Journal of Computational Physics 152, 584-607.

Dalrymple, R.A., Rogers, B.D., 2006. Numerical modeling of water waves with the SPH method. Coastal Engineering 53, 141-147.

De Tullio, M.D., Cristallo, A., Balaras, E., Verzicco., 2009. Direct numerical simulation of the pulsatile flow through an aortic bileaflet mechanical heart valve. The Journal of Fluid Mechanics 622, 259-290.

Doenst, T., Spiegel, K., Reik, M., Markl, M., Hennig, J., Nitzsche, S., Beyersdorf, F., Oertel, H., 2009. Fluid-dynamic modeling of the human left ventricle: methodology and application to surgical ventricular reconstruction. Annals of Thoracic Surgery 87, 1187-1195.

Dominguez, J.M., Crespo, A.J.C., Gómez-Gesteira, M., Marongiu, J.C., 2010. Neighbour lists in smoothed particle hydrodynamics. International Journal for Numerical Methods in Fluids; DOI:10.1002/fld.2481.

Dumont, K., Vierendeels, J., van Nooten, G., Verdonck, P., Bluestein, D., 2007. Comparison of the hemodynamic and thrombogenic performance of two bileaflet mechanical heart valves using a CFD/FSI model. Journal of Biomechanical Engineering 129 (4), 558-565.

Ellero, M., Kroger, M., Hess S., 2002. Viscoelastic flows studied by smoothed particle hydrodynamics. Journal of Non-Newtonian Fluid Mechanics 105, 35-51.

Fox, R.W., McDonald, A.T., Pritchard, P.J., 2004. Introduction to fluid mechanics. 6th Ed., John Wiley & Sons. Inc., New York, USA.

Frisch, U., Hasslacher, B. and Pomeau, Y., 1986. Lattice gas automaton for the Navier-Stokes Equation, Physical Review Letters 56, 1505-1508.

Ge, L., Jones, S.C., Sotiropoulos, F., Healy, T.M., Yoganathan, A.P., 2003. Numerical simulation of flow in mechanical heart valves: grid resolution and the assumption of flow symmetry. Journal of Biomechanical Engineering 125 (5), 709-718.

Gésan-Guiziou, G., Daufin, G., Boyaval, E., Berre, O., 1999. Wall shear stress: effective parameter for the characterisation of the cross-flow transport in turbulent regime during skimmed milk microfiltration. Lait 79 (3), 347-354.

Ghia, U., Ghia, K.N., Shin, C.T., 1982. High-Re solutions for incompressible flow using the Navier–Stokes equations and a multigrid method. Journal of Computational Physics 48, 387-411.

Gingold, R.A., Monaghan, J.J., 1977. Smoothed particle hydrodynamics: theory and application to non-spherical stars. Monthly Notices of the Royal Astronomical Society 181, 375-389.

Gomez-Gesteira, M., Dalrymple, R.A., 2004. Using a three-dimensional smoothed particle hydrodynamics method for wave impact on a tall structure. Journal of Waterway, Port, Coastal, and Ocean Engineering 130 (2), 63-69.

Gomez-Gesteira, M., Rogers, B.D., Violeau, D., Grassa, J.M., Crespo, A.J.C., 2010. Foreword: SPH for free-surface flows. Journal of Hydraulic Research 48 (Extra Issue), 3-5.

Govindarajan, V., Udaykumar, H.S., Chandran, K.B., 2009. Two-dimensional simulation of flow and platelet dynamics in the hinge region of a mechanical heart valve. Journal of Biomechanical Engineering 131 (3), 031002.

Gray, J.P., Monaghan, J.J., Swift, R.P., 2001. SPH elastic dynamics. Computer Methods in Applied Mechanics and Engineering 190, 6641-6662.

Grigioni, M., Morbiducci, U., D'Avenio, G., Di Benedetto, G., Del Gaudio, C., 2005. A novel formulation for blood trauma prediction by a modified power-law mathematical model. Biomechanics and Modeling in Mechanobiology 4 (4), 249-260.

Haji-Sheikh, A., Sparrow, E.M., 1967. The solution of heat conduction problems by probability methods. Journal of Heat Transfer 89 (2), 121-130.

Hammersley, J.M., Handscomb, D.C., 1964. Monte Carlo methods. Chapman and Hall, London & New York.

Hardy, J., de Pazzis, O., Pomeau, Y., 1976. Molecular dynamics of a classical lattice gas: transport properties and time correlation functions, Physical Review A 13, 1949-1961.

Harlow, F.H., 1956. A machine calculation method for hydrodynamic problems. Los Alamos Scientific Laboratory report LAMS-1956.

Harlow, F.H., 1964. The particle-in-cell computing method for fluid dynamics. Methods in Computational Physics 3, 319-343.

Heart and Stroke Foundation of Canada, 2003. The Growing Burden of Heart Disease and Stroke in Canada. Ottawa, Canada.

Hellums, J.D., Peterson, D.M., Stathopoulos, N.A., Moake, J.L., Giorgio, T.D., 1987. Studies on the mechanisms of shear-induced platelet activation. in: Hartman, A., Kuschinsky W., (Editors). Cerebral Ischemia and Hemorheology, Springer-Verlag, New York, 80-89.

Hu, X.Y., Adams, N.A., 2006. A multi-phase SPH method for macroscopic and mesoscopic flows. Journal of Computational Physics 213, 844-861.

Imaeda, Y., Inutsuka, S.-I., 2002. Shear flows in smoothed particle hydrodynamics. The Astrophysical Journal 569, 501-518.

Irace, C., Cortese, C., Fiaschi, E., Carallo, C., Farinaro, E., Gnasso, A., 2004. Wall shear stress is associated with intima-media thickness and carotid atherosclerosis in subjects at low coronary heart disease risk. Stroke 35, 464-468.

Issa, R., Lee, E.S., Violeau, D., Laurence, D.R., 2005. Incompressible separated flows simulation with the smoothed particle hydrodynamics gridless method. International Journal for Numerical Methods in Fluid 47, 1101-1106.

Jiang, F., Oliveira, M.S.A., Sousa, A.C.M., 2006. SPH simulation of transition to turbulence for planar shear flow subjected to a streamwise magnetic field. Journal of Computational Physics 217, 485-501.

Kilner, P.J., Yang,. G.Z., Wilkes, A.J., Mohiaddin, R.H., Firmin, D.N., Yacoub, M.H., 2000. Asymmetric redirection of flow through the heart. Nature 404, 759-761.

King, M. J., Corden, J., David, T., Fisher, J., 1996. A three-dimensional, time-dependent analysis of flow through a bileaflet mechanical heart valve: comparison of experimental and numerical results. Journal of Biomechanics 29 (5), 609-618.

Koseff, J.R., Street, R.L., 1984. The lid-driven cavity flow: a synthesis of qualitative and quantitative observations. Journal of Fluids Engineering 106, 390-398.

Koshizuka, S., Nobe, A., Oka Y., 1998. Numerical analysis of breaking waves using the moving particle semi-implicit method. International Journal for Numerical Methods in Fluids 26, 751-769.

Krafczyk, M., Cerrolaza, M., Schulz, M., Rank, E., 1998. Analysis of 3D transient blood flow passing through an artificial aortic valve by lattice-Boltzmann methods. Journal of Biomechanics 31 (5), 453-462.

Krafczyk, M., Tölke, J., Rank, E., Schulz, M., 2001. Two-dimensional simulation of fluid-structure interaction using lattice-Boltzmann methods. Computers and Structures 79, 2031-2037.

Lastiwka, M., Basa, M., Quinlan, N.J., 2009. Permeable and non-reflecting boundary conditions in SPH. International Journal for Numerical Methods in Fluids 61, 709-724.

Lee, E.S., Moulinec, C., Xu, R., Violeau, D., Laurence, D., Stansby, P., 2008. Comparisons of weakly compressible and truly incompressible algorithms for the SPH mesh free particle method. Journal of Computational Physics 227, 8417-8436.

Lemmon, J.D., Yoganathan, A.P., 2000. Three-dimensional computational model of left heart diastolic function with fluid-structure interaction. Journal of Biomechanical Engineering 122 (2), 109-117.

Leonard, A., 1980. Vortex methods for flow simulation. Journal of Computational Physics 37, 289-335.

Liang, F., Taniguchi, H., Liu, H., 2007. A multi-scale computational method applied to the quantitative evaluation of the left ventricular function. Computers in Biology and Medicine 37, 700-715.

Libersky, L., Petschek, A.G., 1991. Smooth particle hydrodynamics with strength of materials. Advances in the Free Lagrange Method. Lecture Notes in Physics 395, 248-257.

Liu, G.R., 2010. Meshfree methods: moving beyond the finite element method. 2nd Edition, CRC Press, Taylor and Francis Group, New York, USA.

Liu, G.R., Liu, M.B., 2003. Smoothed particle hydrodynamics: a meshfree particle method. World Scientific Publishing Co. Pte. Ltd, New Jersey, USA.

Liu, M.B., Liu, G.R., Lam, K.Y., 2003. Constructing smoothing functions in smoothed particle hydrodynamics with applications. Journal of Computational and Applied Mathematics 155 (2), 263-284.

Liu, J.S., Lu, P.C., Chu, S.H., 2000. Turbulence characteristics downstream of bileaflet aortic valve prostheses. Journal of Biomechanical Engineering 122 (2), 118-124.

Long, Q., Merrifield, R., Yang, G.Z., Kilner, P.J., Firman, D.N., Xu, X.Y., 2003. The influence of inflow boundary conditions on intra left ventricle flow predictions. Journal of Biomechanical Engineering 125, 922-927.

Loudon, C., Tordesillas, A., 1998. The use of dimensionless Womersley number to characterize the unsteady nature of internal flow. Journal of Theoretical Biology 191, 63-78.

Lu, P.C., Lai, H.C., Liu, J.S., 2001. A revaluation and discussion on the threshold limit for hemolysis in a turbulent shear flow. Journal of Biomechanics 34, 1361-1364.

Lucy, L.B., 1977. A numerical approach to the testing of the fission hypothesis. Astronomical Journal 82, 1013-1020.

Ma, J., Ge, W., 2008. Is standard symmetric formulation always better for smoothed particle hydrodynamics?. Computers and Mathematics with Applications 55, 1503-1513.

McQueen, D.M., Peskin, C.S., 2000. A three-dimensional computer model of the human heart for studying cardiac fluid dynamics. Computer Graphics 34, 56-60.

Metropolis, N., 1987. The beginning of the beginning of the Monte Carlo method. Los Alamos Science, Number 15, 125-130 (special issue in honor of S. Ulam).

Moiseyev, G., Bar-Yoseph, P.Z., 2010. No need for particle tracing: from accumulating fluid properties to novel blood coagulation model in the lattice Boltzmann method. Journal of Biomechanics 43 (5), 864-870.

Monaghan, J.J., 1989. On the problem of penetration in particle methods. Journal of Computational Physics 82 (1), 1-15.

Monaghan, J.J., 1992. Smoothed particle hydrodynamics. Annual Review of Astronomy and Astrophysics 30, 543-574.

Monaghan, J.J., 1994. Simulating free surface flows with SPH. Journal of Computational Physics 110, 399-406.

Monaghan, J.J., 2002. SPH compressible turbulence. Monthly Notices of the Royal Astronomical Society 335, 843-852.

Monaghan, J.J., 2006. Smoothed particle hydrodynamic simulations of shear flow. Monthly Notices of the Royal Astronomical Society 365, 199-213.

Monaghan, J.J., Cas, R.F., Kos, A., Hallworth, M., 1999. Gravity currents descending a ramp in a stratified tank. Journal of Fluid Mechanics 379, 39-69.

Monaghan, J.J., Gingold, R.A., 1983. Shock simulation by the particle method SPH. J. Computational Physics 52, 374-389.

Monaghan, J.J., Kocharyan, A., 1995. SPH simulation of multi-phase flow. Computer Physics Communications 87, 225-235.

Monaghan, J.J., Kos, A., 1999. Solitary waves on a Cretan beach. Journal of Waterway, Port, Coastal, and Ocean Engineering 1111, 145-154.

Morris, J.P., Fox, P.J., Zhu, Y., 1997. Modeling low Reynolds number incompressible flows using SPH. Journal of Computational Physics 136, 214-226.

Morris, J.P., Monaghan, J.J., 1997. A switch to reduce SPH viscosity. Journal of Computational Physics 136, 41-50.

Munson, B.R., Young, D.F., Okiishi, T.H., 2005. Fundamentals of fluid mechanics. 5th Ed., John Wiley & Sons Inc., USA.

Nakamura, M., Wada, S., Mikami, T., Kitabatake, A., Karino, T., 2002. A computational fluid mechanical study on the effects of opening and closing of the mitral orifice on a

transmitral flow velocity profile and an early diastolic intraventricular flow. JSME International Journal Series C 45 (4), 913-922.

Nobili, M., Morbiducci, U., Ponzini, R., Del Gaudio, C., Balducci, A., Grigioni, M., Maria Montevecchi, F., Redaelli, A., 2008. Numerical simulation of the dynamics of a bileaflet prosthetic heart valve using a fluid-structure interaction approach. Journal of Biomechanics 41 (11), 2539-2550.

Pedrizzetti, G., Domenichini, F., 2005. Nature optimizes the swirling flow in the human left ventricle. Physical Review Letters 95 (10), 108101.1-108101.4.

Pelliccioni, O., Cerrolaza, M., Herrera, M., 2007. Lattice Boltzmann dynamic simulation of a mechanical heart valve device. Mathematics and Computers in Simulation 75, 1-14.

Perez, S., Zachrich, G., 2000. Monte Carlo simulation for determination of the stream function. Computer Applications in Engineering Education 8 (1), 38–42, 2000.

Peskin, C.S., 2002. The immersed boundary method. Acta Numerica 11, 1-39.

Price, D.J., Monaghan, J.J., 2004. Smoothed particle hydrodynamics: I- Algorithms and tests in one dimension. Monthly Notices of the Royal Astronomical Society 348, 123-138.

Quinlan, N.J., Basa, M., Lastiwka, M., 2006. Truncation error in mesh-free particle methods. International Journal for Numerical Methods in Engineering 66, 2064-2085.

Randles, P.W., Libersky L., 1996. Smoothed particle hydrodynamics some recent improvements and applications. Computer Methods in Applied Mechanics and Engineering 139, 375-408.

Redaelli, A., Bothorel, H., Votta, E., Soncini, M., Morbiducci, U., Del Gaudio, C., Balducci, A., Grigioni, M., 2004. 3-D simulation of the St. Jude Medical bileaflet valve opening process: fluid-structure interaction study and experimental validation. Journal of Heart Valve Disease 13, 804-813.

Richie, B.W., Thomas, P.A., 2001. Multiphase smoothed-particle hydrodynamics. Monthly Notices of the Royal Astronomical Society 323, 743-756.

Rodevand, O., Bjornerheim, R., Edvardsen, T., Smiseth, O.A., Ihlen, H., 1999. Diastolic flow pattern in the normal left ventricle. Journal of the American Society of Echocardiography 12 (6), 500-507.

Rubinstein, R.Y., Kroese, D.P., 2008. Simulation and the Mont Carlo method. 2nd Ed., John Wiley & Sons Inc., New Jersey, USA.

Saber, N.R., Wood, N.B., Gosman, A.D., Merrifield, R.D., Yang, G.Z., Charrier, C.L., Gatehouse, P.D., Firmin, D.N., 2003. Progress towards patient-specific computational flow modeling of the left heart via combination of magnetic resonance imaging with computational fluid dynamics. Annals of Biomedical Engineering 31 (1), 42-52.

Shankar, P.N., Deshpande, M.D., 2000. Fluid mechanics in the driven cavity. Annual Review of Fluid Mechanics 32, 93-136.

Shao, S., Gotoh, H., 2004. Simulating coupled motion of progressive wave and floating curtain wall by SPH- LES model. Coastal Engineering Journal 46, 171-202.

Shao, S., Ji, C., Graham, D.I., Reeve, D.E., James, P.W., Chadwick, A.J., 2006. Simulation of wave overtopping by an incompressible SPH model. Coastal Engineering 53, 723-735.

Shao, S., Lo, E.Y.M., 2003. Incompressible SPH method for simulating Newtonian and non-Newtonian flows with a free surface. Advances in Water Resources 26, 787-800.

Sigalotti, L.D.G., Klapp, J., Sira, E., Melean, Y., Hasmy, A., 2003. SPH simulations of time-dependent Poiseuille flow at low Reynolds numbers. Journal of computational physics 191, 622-638.

Smadi, O., Hassan, I., Pibarot, P., Kadem, L., 2010. Numerical and experimental investigations of pulsatile blood flow pattern through a dysfunctional mechanical heart valve. Journal of Biomechanics 43 (8), 1565-1572.

Sotiropoulos, F., Borazjani, I., 2009. A review of state-of-the-art numerical methods for simulating flow through mechanical heart valves. Medical and Biological Engineering and Computing 47 (3), 245-256.

Souli, M., Benson, D.J., (Editors), 2010. Arbitrary Lagrangian Eulerian and fluid-structure interaction: numerical simulation. Wiley-ISTE, London, UK.

Stillinger, F.H., Rahman, A., 1974 . Improved simulation of liquid water by molecular dynamics. Journal of Chemical Physics 60, 1545-1557.

Takeda, H., Miyama, S.M., Sekiya, M., 1994. Numerical simulation of viscous flow by smoothed particle hydrodynamics. Progress of Theoretical Physics 92, 939-960.

Taylor, T.W., Yamaguchi, T., 1995. Realistic three dimensional left ventricular ejection determined from computational fluid dynamics. Medical Engineering & Physics 17 (8), 602-608.

Ting, T.S., Prakash, M., Cleary, P.W., Thompson, M.C., 2005. Simulation of high Reynolds number flow over a backward facing step using SPH. ANZIAM Journal 47, C292-C309.

Traub, O., Berk, B.C., 1998. Laminar shear stress: mechanisms by which endothelial cells transduce an atheroprotective force. Arteriosclerosis, Thrombosis, and Vascular Biology 18, 677-685.

Vacondio, R., Rogers, B.D., Stansby, P.K., 2011. Smoothed particle hydrodynamics: approximate zero-consistent 2-D boundary conditions and still shallow water tests. International Journal for Numerical Methods in Fluids, DOI: 10.1002/fld.2559.

Vaughan, G.L., Healy, T.R., Bryan, K.R., Sneyd, A.D., Gorman, R.M., 2008. Completeness, conservation and error in SPH for fluids. International Journal for Numerical Methods in Fluids 56, 37-62.

Versteeg, H., Malalasekra, W., 2007. An introduction to computational fluid dynamics: the finite volume method. 2nd Edition, Prentice Hall, USA.

Vierendeels, J.A., Riemslagh, K., Dick, E., 2000. Computer simulation of intraventricular flow and pressure gradients during diastole. Journal of Biomechanical Engineering 122 (6), 667-674.

Vila, J.P., 1999. On particle weighted methods and smooth particle hydrodynamics. Mathematical Models and Methods in Applied Sciences 9 (2), 161-209.

Violeau, D., Issa, R., 2007. Numerical modeling of complex turbulent free-surface flows with the SPH method: an overview. International Journal for Numerical Methods in Fluids 53, 277-304.

Waite, L., Fine, J., 2007. Applied biofluid mechanics. 1st Ed., McGraw-Hill, New York, USA, 113-116.

Watanabe, H., Hisada, T., Sugiura, S., Okada, J., Fukunari, H., 2002. Computer simulation of blood flow, left ventricular wall motion and their interrelationship by fluid-structure interaction finite element method. JSME International Journal Series C 45 (4), 1003-1012.

White, F.M., 1991. Viscous fluid flow. 2nd Ed., McGraw-Hill book Co., New York, USA.

Wilcox, D.C., 2006. Turbulence modeling for CFD. 3rd ed., DCW Industries Inc., La Canada CA, USA.

Wingate, C.A., Stellingwerf, R., 1994. SPHINX users manual, LAUR 932476, Los Alamos National Lab., Los Alamos, NM 87545.

Yamaguchi, R., Mashima, T., Amagai, H., Fujii, H., Hayase, T., Tanishita, K., 2005. Variation of wall shear stress and periodic oscillations induced in the right-angle branch during laminar steady flow. Journal of Fluids Engineering 127 (5), 1013-1020.

Yoganathan, A.P., Chandran, K.B., Sotiropoulos, F., 2005. Flow in prosthetic heart valves: state-of-the-art and future directions. Annals of Biomedical Engineering 33 (12), 1689-1694.

Zhu, Y., Fox, P.J., Morris, J.P., 1999 . A pore-scale numerical model for flow through porous media. International Journal for Numerical and Analytical Methods in Geomechanics 23, 881-904.

Zienkiewicz, O.C., Taylor, R.L., Nithiarasu, P., 2005. The finite element method for fluid dynamics. 6th Ed., Elsevier Butterworth-Heinemann, Oxford, UK.